_____MASTER'S THESIS _____

Model Generation for Current Induced Stress of Electrical Components in Automotive Battery Systems

conducted at the
Institute of Electronics
Graz University of Technology, Austria

in co-operation with
Samsung SDI Co., Ltd.
Premstätten, Austria

by:
Brankovic, Emir BSc.
Matriculation Nr. 01431789

Supervisors:
Univ.-Prof. Dipl.-Ing. Dr.techn. Deutschmann, Bernd
(Institute of Electronics)
Dipl.-Ing. Dr.techn. Parz, Peter
(Samsung SDI Co., Ltd.)

Graz, in June 2020

Affidavit

I declare that I have authored this thesis independently, that I have not used other than the declared sources/resources, and that I have explicitly indicated all material which has been quoted either literally or by content from the sources used. The text document uploaded to TUGRAZonline is identical to the present master's thesis.

15. June 2020	*Brankovic Emir*
Date	Signature

Eidesstattliche Erklärung

Ich erkläre an Eides statt, dass ich die vorliegende Arbeit selbstständig verfasst, andere als die angegebenen Quellen/Hilfsmittel nicht benutzt, und die den benutzten Quellen wörtlich und inhaltlich entnommene Stellen als solche kenntlich gemacht habe. Das in TUGRAZonline hochgeladene Textdokument ist mit der vorliegenden Masterarbeit identisch.

15. June 2020	*Brankovic Emir*
Datum	Unterschrift

ife

Abstract

Electric Vehicles (EV) are getting more and more popular and with EU regulations to cut the CO_2 emissions to 0% by 2050, there is huge ongoing research to optimize and develop the EV suitable for mass use. The electrical components are getting smaller and lighter to reduce the total weight, save space, and ultimately reduce the costs. Thus, the components are pushed to their limits and there are some rising safety concerns. EV being reliable is one of the things taken for granted, but more than half of the components are implemented simply because of safety reasons. The highest priority in the automotive industry is the people's safety using or operating the vehicle.

Even though a great effort is put into making the EV safe as possible, accidents do happen and in case of emergency the battery, where all the EV energy is stored, must be disconnected as fast as possible from the rest of the car. Components that play a crucial role in separating the battery from the rest of the EV, are housed in the Battery Disconnect Unit (BDU). If one of the components of the BDU fails, the whole BDU fails, and the components can be guaranteed to perform as they should only if their temperature does not exceed certain limits. Thus, thermal management is getting significant importance for the component temperature monitoring and one way to that is by thermal simulations.

In this thesis, a method for generating a 1D Thermal Model using the Finite Difference Method (FDM) considering only electric current as model input, is presented. The thermal model is developed for the safety components placed inside the BDU (e.g. shunts and relay) and for the BDU. Using the developed thermal model, it is possible to predict the transient and maximal temperature of different parts of BDU components, which are crucial for the safe operation of EV. Furthermore, the developed model is suitable for efficient computation and gives satisfactory accuracy when compared to the measurements and complex 3D simulations using commercial software.

On this basis, a recommendation is given for further model optimization and steps to be considered. Thus, this thesis hopes to offer useful guidelines and sources of information for future thermal or related model development.

Kurzfassung (German)

Elektrofahrzeuge gewinnen immer mehr an Beliebtheit und mit den EU-Vorschriften zur Reduzierung der CO_2-Emissionen auf 0 % bis 2050 wird viel in die Forschung investiert, um die für die Massenproduktion geeigneten Elektrofahrzeuge zu optimieren. Um Platz, Gewicht und Kosten zu verringern, werden die verbauten elektrischen Komponenten ständig kleiner und leichter. Demzufolge werden die Komponenten an ihre Grenzen gebracht und es stellt sich die Frage, ob die Gesamtsicherheit dadurch gefährdet ist. Es wird als selbstverständlich angenommen, dass die Elektrofahrzeuge zuverlässig und sicher sind. Dennoch, mehr als die Hälfte der Komponenten wird nur aus Sicherheitsgründen eingebaut. Die höchste Priorität in der Automobilindustrie hat die Sicherheit der Menschen bei der Verwendung oder Bedienung des Fahrzeugs.

Obwohl große Anstrengungen unternommen werden, um die Elektrofahrzeuge so sicher wie möglich zu machen, können Unfälle passieren, und im Notfall muss die Batterie, in der die gesamte Energie gespeichert ist, so schnell wie möglich vom Rest des Autos getrennt werden. Komponenten, die eine entscheidende Rolle bei der Trennung der Batterie spielen, sind in der Batterietrenneinheit untergebracht. Wenn eine der Komponenten ausfällt, so fällt die gesamte Batterietrenneinheit aus. Die Komponenten behalten ihre vorgegebenen Eigenschaften nur, falls ihre Temperatur sich in einem bestimmten Temperaturintervall befindet. Überschreitet die Komponententemperatur die obere Temperaturgrenze so kann nicht mehr gewährleistet werden, dass diese über die gesamte Nutzungsdauer eines Fahrzeugs noch korrekt funktioniert. Daher gewinnt das Wärmemanagement für die Überwachung der Komponententemperatur zunehmend an Bedeutung und Durchführung von Wärmesimulationen ist eine der beliebten Lösungen.

In dieser Arbeit wird eine Methode zur Generierung eines 1D-Wärmemodells unter Verwendung der Finite-Differenzen-Methode (FDM) vorgestellt, bei der nur elektrischer Strom als Modellinput dient. Das Wärmemodell wurde für die Sicherheitskomponenten in der Batterietrenneinheit (z. B. Shunts und Relais) und für die gesamte Batterietrenneinheit entwickelt. Mit dem entwickelten Wärmemodell ist es möglich, die transiente und maximale Temperatur verschiedener Teile von Batterietrenneinheit-Komponenten vorherzusagen, die für den sicheren Betrieb von Elektroautos entscheidend sind. Darüber hinaus eignet sich das entwickelte Modell für eine effiziente Berechnung und bietet eine zufriedenstellende Genauigkeit im Vergleich zu Messungen und komplexen 3D-Simulationen mit kommerzieller Software.

Auf Basis dieser Arbeit wird eine Empfehlung für weitere Modelloptimierungen gegeben. Daher kann diese Arbeit als nützliche Informationsquelle für die zukünftige thermische oder ähnliche Modellentwicklung fungieren.

Acknowledgments

I certainly would not have finished this work without the help of those who were with me every step of the way. They were by my side from the very beginning, when I needed the most motivation, and with me when I had a question.

Therefore, I would like to express my sincere gratitude to my supervisor Univ.-Prof. Dipl.-Ing. Dr.techn. Bernd Deutschmann, who pointed me in the right direction right at the start and who was there with valuable information. Furthermore, my utmost gratitude goes to my co-supervisor and my chef, Dipl.-Ing. Dr.techn. Peter Parz, with whose help I got the opportunity to do my master's thesis in cooperation with Samsung SDI. I would like to thank him for his tremendous patience he has given to me and the possibility to contact him at any time with any question. I would also like to thank Dipl.-Ing. Matic Blaznik, who provided me with 3D models and instructed me on how to improve my models. I am especially grateful to my father, Dipl.-Ing. Zlatan Brankovic, who tirelessly supported my work even when I did not have an answer and gave me the motivation to carry on with my work.

Finally, I want to thank my family, who has been by my side and allowing me carefree studies, and to my friends who were with me and when I wanted to take a break from everything. Without all of them, I certainly would not have finished this work in such a good way.

Thank you.

Contents

ife

ife

Abbreviations

EV	Electrical Vehicle
IC	Integrated Circuits
BDU	Battery Disconnect Unit
BMS	Battery Management System
ADC	Analog-to-Digital Converter
HVDC	High-voltage Direct Current
PSU	Power Supply
ODE	Ordinary Differential Equation
FDM	Finite Difference Method
FEM	Finite Element Method

Symbols

U	electrical voltage, V	$\dot{q}$	rate of energy generation per unit volume, W/m³
U_{th}	thermal voltage, V		
I	electrical current, A	q''	heat flux, W/m²
P	electrical power, W	k	thermal conductivity, W/m·K
R	ohmic resistance, Ω	h	convection heat transfer coefficient, W/m²·K
R_{Ref}	reference resistance at 293K, Ω		
R_{th}	thermal resistance, K/W	ε	emissivity
T	temperature, K	E^{tot}	total energy, J
T_{∞}	fluid temperature, K	$\dot{E_{in}}$	rate of energy transfer into a control volume, W
T_S	surface temperature, K		
T_{Ref}	reference temperature at 293.15K	$\dot{E_{out}}$	rate of energy transfer out of control volume, W
α	thermal resistivity coefficient, 1/K		
Q	energy (heat) transfer, J	$\dot{E_g}$	rate of energy generation, W
m	mass, kg	$\dot{E_{st}}$	rate of increase of energy stored within a control volume, W
c	specific heat, J/kg·K		
c_p	specific heat at constant pressure, J/kg·K	ρ	density, kg/m³
C_{th}	thermal mass, J/K		
S	Seebeck coefficient, V/K		
J	current density, Am⁻²		
σ_{el}	electrical conductivity, S/m		
σ	Stefan-Boltzmann constant, W/m⁻²·K⁻⁴		
q	heat transfer rate, W		

ife

1 Introduction

1.1 Motivation

E arth's climate change is a major problem of modern society and one of the biggest pollutants is the mobility sector. Regulations under the Paris agreement[1] from 2016 demand that carbon neutrality[2] must be reached by the second half of the 21st century and the need to create more energy-efficient vehicles is one of the promising solutions. The major European car manufacturers are investing a lot in the electromobility research and development and we are witnesses of a rising trend of EVs on our streets. Thus, the customers' needs for vehicle range, power, and expenses are not always easy to satisfy and the car manufacturers are trying to find new ways to store more energy in battery cells while minimizing the time needed for charging and costs. Higher voltage levels are a good way to reduce the copper costs and the ongoing developments are now targeting 800 V-platforms. [1]

With higher voltage levels and higher energy density in battery packs, some rising safety concerns must be dealt with before mass production. Cars being reliable is one of the things we just take for granted. This feat of extreme reliability was certainly not easy to achieve. On the integrated electrical circuits (IC) of vehicles, more than half of the components are implemented simply because of safety reasons. Safety is the top priority in the automotive industry. If an accident does happen (e.g. a car crash or short circuit) the battery pack, where all the EV energy is stored, needs to be disconnected fast from the rest of the car. The safety devices in EV should fulfil the following requirements in case of emergency: separate the battery from the rest of the car and keep the spare energy away from the passenger.

One of the most important safety devices in EV is the Battery Disconnect Unit (BDU) and its main function is to disconnect the battery from the rest of the car. Additionally, the BDU should disconnect in case of battery charging failure, case of deactivation, or if some other EV component fails so that higher current as permitted occurs. [2, p. 13]

---

[1] For additional reading please refer to [33].

[2] Refers to achieving zero carbon dioxide (CO_2) emission; the total balance between absorption of carbon from the atmosphere in carbon sinks and its emissions.

■ife

During the EV operation, the current through the BDU rises significantly and heat is being generated. Heat generation represents a major threat to the safe operation of components inside the BDU. This is because every electrical device has a desired operating temperature range, ranging from -40°C to 120°C. If the component temperature of the BDU exceeds the upper limit, it cannot be guaranteed that the safety components will operate as they are supposed to. [3, p. 6]

Following the simple rule: *If one of the components fails the whole of BDU fails*, shows the importance of thermal management inside the BDU. Thus, power dissipation within the components can cause high-temperature gradients and rise of inner resistance, which strongly affects the performance, especially in cases where high accuracy and reliability is required. [4, p. 846] Components contributing most to the thermal load are relays, fuses, and busbars, which cannot release the heat easily into the ambient air. Consideration of heat transfer must be taken seriously, and it should be considered in the process of designing and operational monitoring of the BDU. One of the best, low-cost methods is to embody the thermal transfer of the different components through computer simulations. Nevertheless, computer simulation must fulfil requirements in the sense of compatibility of simplicity and satisfactory accuracy.

Nowadays, there is no novelty that the current trend in the automotive industry is toward higher packing density with the system gaining new dimensions. With the large power densities and rising concerns of system failure, especially because of thermal dissipation I was more than intrigued to tackle some of the current *heat transfer problems* inside the BDU!

ife

1.2 State of Art

Thermal modeling and management are getting significant importance in the automotive industry with its ICs and components inside BDUs pushed to their limits. Thus, the electrical equipment is densely assembled, and designers continually make them even more compact to save weight, space, and finally reduce production costs. Busbars, relays, and fuses control the electrical current I through the BDU, and because of ohmic resistance R, *Joule* heating[3] is generated. Excessive heat can damage each component and/or endanger the behaviour of modern vehicle BDU and other ICs.

Nevertheless, to implement a fully coupled electrothermal simulation is far from being trivial. Through recent history, different methodologies were presented. Most of them involve 3D numerical software tools coupled with electrical simulator software, where the 3D software is used to solve the transient heat diffusion equation with the power dissipation given from the electrical simulator. Though this method of electrothermal simulation requires large memory requirements and long CPU simulation time, it led to satisfactory accuracy, meaning the convergence between simulation and experimental values were present. Another method, introduced by *W. Luft* and *E. J. Diebold* [5] in 1961, proposed the construction of thermal resistance, which quickly calculates the temperature response to the corresponding power dissipation calculated by the electrothermal simulator. The implementation of thermal resistance is done in the form of an equivalent electrical RC network. In this way, one can get a dynamic thermal response with much less CPU simulation time and memory resources. Various other approaches can be found in literature, which is dealing with this problem. Thus, they all have as basis one of the basic methods described above. [6, p. 1031]

To be concise and to give the reader of this paper a better overview of the literature, found dealing with this problem, some of the more relevant[4] papers ([4], [7], [8], [9], [10], [11], [12] chronological) dating back from the 1970s will be reflected (see *Figure 1*). Furthermore, the solution they proposed together with its advantages and disadvantages will be presented.

---

[3] *Joule* heating (*Ohmic* heating or *resistive* heating) is process of heat generation in electrical conductor with resistance R by the passage of an electrical current I.

[4] During the literature research, I have ascertained more than 40 scientific papers dating back to the 1960s, when the first computer software's started to emerge. Most papers were referencing the same papers and were not independent of each other. Thus, only 7 papers stated different methodologies to simulate the electrothermal effects within integrated ICs and only 2 ([8], [11]) papers were discussing methods to assert the heat transfers inside BDUs.

■ife

Problem
Existing simulation softwares model electrical components at constant temperature.

1976

Solution
Developed electro-thermal simulator which includes chip temperature gradients.
Used Software
Saber Circuit Simulator (for electro-thermal simulations)

Problem
Electrical devices are often heated significantly by power dissipated within device (self-heating) and by other devices (thermal coupling).

1993

Solution
Developed electro-thermal simulator for dynamic temperature distribution.
Used Software
Saber Circuit Simulator (for electro-thermal simulations)

Problem
Vehicle IC systems are getting larger in scale every year. The importance of thermal management is increasing. The main heat generators in BDUs are fuses, relays and busbars. Thus, designers pack them in thight, compact boxes to save space.

2002

Solution
Heat transfer resistance is calculated by assuming temperature of each part, and then the temperature of each part is calculated. Commercial software is used for automatic generation of the mesh.
Used Software
Not specified

Problem
By neglecting the thermal response of electrical componens the operational behaviour may differ from predicted by numerical simulations. Electrical and thermal problem must be solved simultaneously in order to indentify and prevent problems during the desing.

2006

Solution
Proposed co-simulation methodology. Saber Simulation Software was used to perform the electrical portion of the simulation. Temperature calculations were performed with external Software.
Used Software
Saber Circuit Simulator (for electrical modelling)
External Software (for thermal simulations)

Problem
FEA for electro-thermal simulations are very time consuming. Circuit simulations have been limited to electronic models at selected temperature. Thermal Circuits (Foster RC) have insufficient accuracy.

2016

Solution
Mixed-Mode Setup of a 3D FEA thermal model and electrical circuit model.
Used Software
Synopsis TCAD Sentaurus Environment

Problem
The number of electricals components and systems in modern vehicles is increasing. Electrical power is rising, so is Joule heating and so temperature and malfunctions.

2013

Solution
Detailed models of IC components and their behavior based on 3D model rather on simplified circuit.
Used Software
ANSYS Software (for thermal FEA simulations)

Problem
Pressure upon power device manufactures to make electronic devices pushed to their limits e.g. high temperatures, high power density, strong integration and compact shapes. Increasing need for electrothermal simulation.

2010

Solution
Compact Thermal Models (Zth ... RC ... Network ... VHDL-AMS).
Used Software
COMSOL Multiphysics (for FAE), VHDL-AMS (for modeling of CTM), MATLAB (for extracting RC parameters)
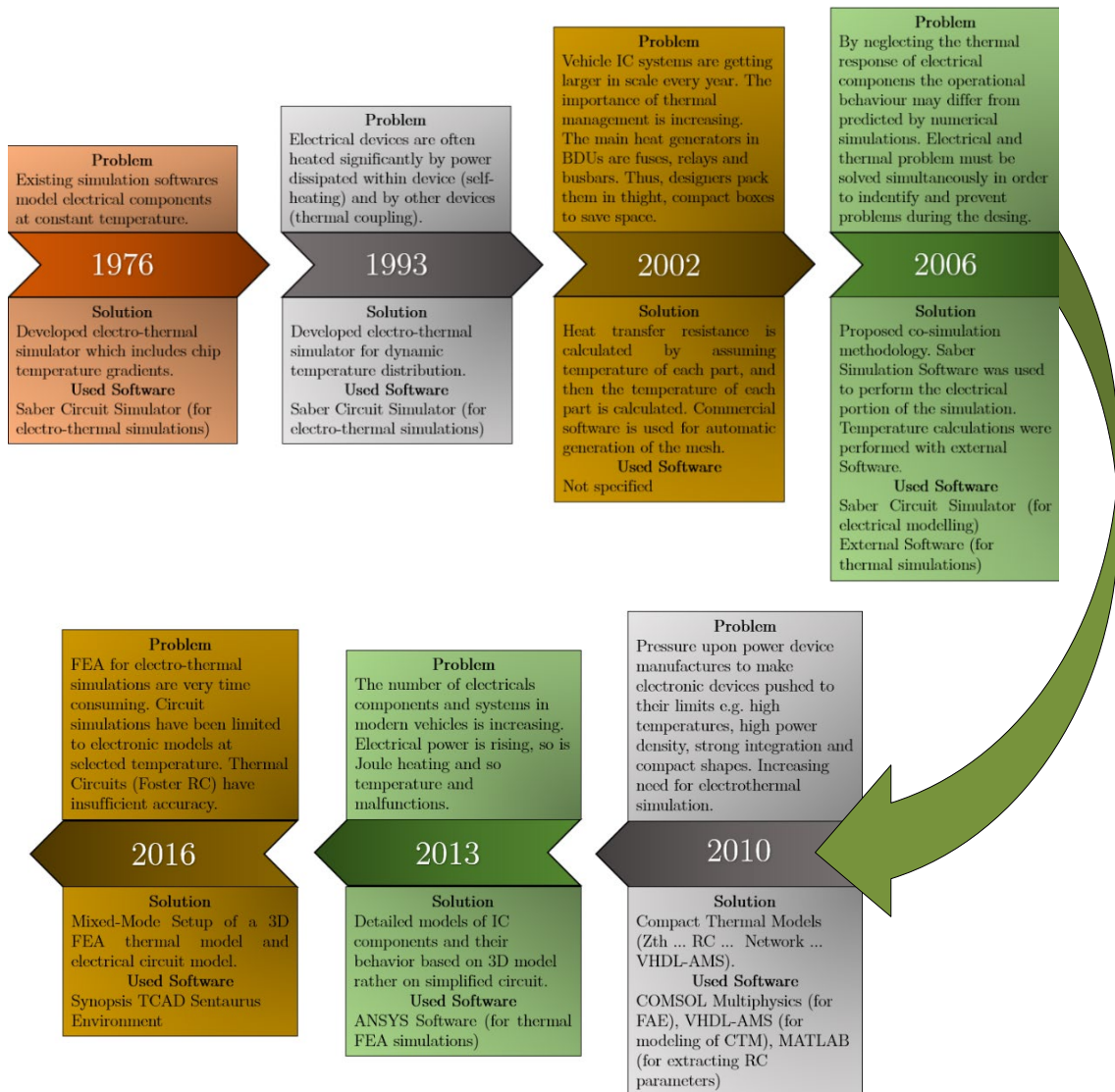
Figure 1: Electro-thermal problem through recent history

In addition to the two basic techniques mentioned above for electro-thermal modelling, the research was using three approaches to represent the thermal phenomena. The various approaches are summarized in the following table (see **Table 1**). Thus, exhaustive literature can be found, it will not be explained because it would certainly go beyond the scope of this master's thesis.

Finite Element Method (FEM)	Finite Difference Method (FDM)	Equivalent RC Network
Is a numeric method simulating the relationship between thermal responses and heat resource by large number of finite elements.	Is a numeric method by replacing the continuous part of heat equation with discrete approximation.	Simulates relationship between thermal resistance and capacitance by equivalent RC Newtork (Foster or Cauer)
Papers		
[10], [11], [12]	[4], [10]	[5], [9], [10], [12]
Advantages		
More accurate than FDM and RC Good for complicated BC and geometries	Generates easy to solve equations In multi-domain is much easier to couple thermal equations	Simple to build and easy to extend to electrothermal simulations Very fast in comparison to FEM
Disadvantages		
Consumes CPU time Complexity of Equations	Not as accurate as FEM Limitations of structure that can be analyzed	Extracted from thermal response and cannot be achieved independenlty Not accurate as FEM or FDM

Table 1: Advantages and disadvantages of different modelling methods used

Analysing the table above, it is easy to notice, that by applying one or more methods, a trade-off between the accuracy (i.e. the convergence of simulation and experiment values) and the speed of computation, must be accepted. While designing the BDU, the accuracy of the simulation and the clear thermal distribution and influence of the temperature of the individual components on each other is essential. On the other hand, the efficiency of calculation and minimal use of the Battery Management System (BMS) and CPU power is essential for monitoring critical component temperatures in real-time.

In this contribution, the work presented in this master's thesis extends strategies described in [5], [9], [10], [12] by electro-thermal coupling under dynamic conditions in modern EVs BDUs. Thus, through limited memory resources and CPU simulation power of EVs BMS, a 1D heat transfer flow dissipated within the device (i.e. self-heating) and other components (i.e. thermal coupling) are extended based on work from [13] and considered as preferable modelling path.

1.3 Organisation

The work presented here is structured into 7 chapters:

I. **Introduction -** into the topic of the master's thesis is given and explained why the selected topic is currently relevant, and that it will gain in importance in the future. Descriptive literature research has been done, and an overview of the main methods used in the thermal building for the last 50 years is given.

II. **Safety of Electrical Vehicles** - the ongoing developments in the automotive sector and particularly for the EV, is pushing the safety components to their limits. The main safety components (e.g. the shunts and relays) used in EV are described and the impact of high temperature on their operation is explained.

III. **Measurement Setup** - and test overview of the shunt and relay of the Samsung SDI BDUs is described. The principle of and importance of the measurements for the thermal model validation is given. Furthermore, the positions of the thermocouples are given schematically for easier understanding.

IV. **Thermal Model Generation** - the basics of heat transfer is given simply and intuitively. Thus, the reader can easily follow the thermal model generation for the shunt and relay. An appropriate modelling method was chosen to be the Finite Difference Method (FDM). The FDM is explained using lots of figures and a direct connection to the developed thermal models is explained.

V. **Model Validation** - the developed thermal model has no value and no application if it does not correspond to the real-world system. Thus, the thermal model data is compared with the measurements along with statistical analysis for comparison in the mathematical sense.

VI. **Thermal Model for the Battery Disconnect Unit** - the BDU with all its components forms a system, which only performs as it should if all the components are operating correctly. Thus, a thermal model that describes the behaviour of the selected part of the BDU is presented and validated.

VII. **Conclusion and Outlook** - finally, the work presented here is summarized and it is pointed out to all its pros and cons. An outlook and proposal for further work based on developed models are given.

2 Safety of Electrical Vehicles

The world's biggest economies and largest companies are facing the same challenge to reduce the environmental impact and the overall CO_2 emissions. The automotive industry has accepted this challenge and is investing a lot in research and development of energy-efficient EV. The media is contributing a lot to the rising popularity of EV; on one side because of decreasing car prices and on the other because we are bombarded with news about ongoing climate change. To achieve the high set goals, the engineers and scientists are trying to optimize and design the best possible way to store electrical energy, and for now, those are the batteries.

Fundamental electrical safety and protection of those who operate with EV are the number one priority in the automotive industry. The safety of the user is going to be more challenging because of increasing operating voltage, making the protection against direct and indirect contacts more complex. Energy conversion between the EV battery and the motor takes place in the drivetrain (see *Figure 2*). Conversion of the fixed battery's DC voltage into a variable voltage and frequency signal is done by the converter. The AC voltage and its frequency are depended on the user inputs (e.g. push of pedals to accelerate or breaks to stop, …). The controller regulates the user signal to maintain the EV's predefined operational parameters. The main safety blocks (not shown in *Figure 2*) are placed between the battery and the converter. [14]
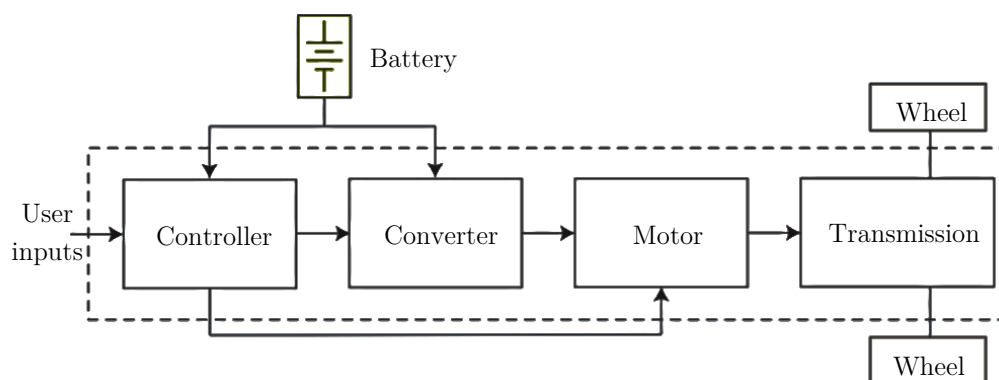
Figure 2: General block diagram the drivetrain of an EV

The battery is the most important part of any EV and the biggest factor affecting the rate of growth in adoption it is the battery. As mentioned before (see **Motivation**) right after the price comes, as a matter of choice, the battery range, lifetime, power, and time needed to reach full charge. The existing batteries are being redesigned and are made lighter, more compact, and with high volumetric energy density. Also, the charging rates and the driving range with one full charge is improving dramatically.

Nevertheless, safety devices inside the EV must work properly at any time because safety is the number one priority in the automotive sector. From all safety devices placed in EV, the BDU and the BMS play the most important role and includes the most important safety components, which ensure the safety of people while driving, handling, or maintaining the vehicle. [15]

2.1 Battery Management System

BMS plays a crucial role, keeping the battery functioning correctly and, in all situations, save for the people driving or maintaining it. Improvements in the field of sensor technology and controller computing power have led that the customer sees the EVs as a good or even better choice over the conventional vehicle. [15]
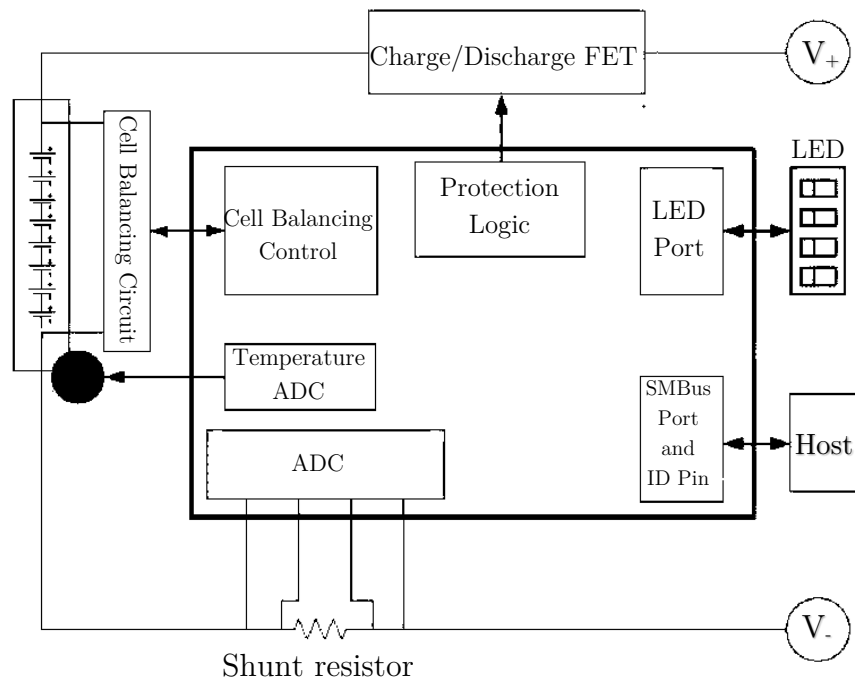
Figure 3: Schematic representation of the Battery Management System (BMS) [16]

BMS is the hidden intelligence behind the organized operation of the battery and the safeguard in combination with BDU to protect the battery from damage and malfunction. Damage to the battery can happen if the Lithium-ion cells are above or below its charging limits, and the BMS has a safeguard device called the Lithium-ion protector circuit, which helps in optimum charging of the battery pack. Energy management within the battery pack is also performed by the BMS, where the status of charge is digitally sent through a signal-bus or displayed on the LED indicator. [16]

One of the most important functions of the BMS is to protect the battery from overheating due to Joule heating and even explosion or flame. This happens if the battery pack or single cell is overcharged and the BMS provides important over-voltage protection. The most important BMS functions can be summarized as follows: [16]

Protection against:
- *Over-temperature*
- *Under-temperature*
- *Over-voltage* (during charging)
- *Under-voltage* (during discharging and especially important for Lithium-ion batteries)
- *Over-temperature*

The BMS may include an internal switch, such as a relay, which can be opened if the battery is outside its safe operating area. The BMS can terminate the usage of devices connected to the battery to reduce energy consumption and it can actively control the battery environment, such as through heaters or cooling fans if the temperature is outside the limits. [16] Nevertheless, the ability of the BMS to perform this function depends on the accuracy of its sensor inputs and one of them is for certain the current sensing which plays a significant role in modern EV. Accurate current measurements are needed to precisely determine the state of charge levels, which data can inform the user of the remaining range and prevent the damaging over-discharging levels.

With high stored power in the batteries, there is always a possibility of an accident. The possibilities for an accident to occur must be minimized and if so, the battery must be disconnected from the rest of the power train as fast as possible. BDU should perform exactly that and disconnect the main source of energy as fast as possible.

2.2 Battery Disconnect Unit

The BDU is the primary interface between the battery pack and the inverter inside the EV. The motor is supplied with electrical energy over the BDU and, also the same way the electrical energy is being recouped back to the battery while braking. The BDU includes electromechanical switches that open or close the electrical path and the BDU provides feedback to the BMS with inputs such as voltage and current measurements. The BMS controls the electromechanical switches via low current paths based on inputs from the BDU sensors and in that way the BDU as a safety device performs several different functions:

 – **Fusing**

The flow of electrical current between the battery and the rest of EV is interrupted when the current as a magnitude greater than a predefined value (e.g. external short circuit).

 – **External charging**

The flow of electrical current between the battery and the outside charger station with the power source is controlled and interrupted if predefined values are reached.

 – **Pre-charging**

High inrush current may occur when the components are first activated (e.g. when the vehicle is first turned on). To protect the other components (e.g. the inverter) from the high current surges the BDU performs pre-charging by controlling current flow from the battery.

 – **Terminal interfacing**

The BDU must include a terminal that satisfies the requirements of a vehicle application. For example, terminal size and the type and whether the terminal is touch-proof.

 – **Current sensing**

The BDU is measuring the current flow through high current paths between the battery and the inverter. [17, p. 12]

The design and the placing of the safety components in the finished BDU can differ a lot, but the basic schematic layout (see *Figure 4*) is very much the same for all BDUs. It consists of a pre-charge circuit with a relay in series with battery and capacitor and inverter in parallel. The two main relays and melting fuse are also in series and this type of connection enables fast to connect and disconnect the battery from the drive train. In normal operation, the two main relays are used to switch both poles, where the negative pole is connected first. In case of an accident or some sort of electrical fault, the main relays disconnect the current. [18]

■ife
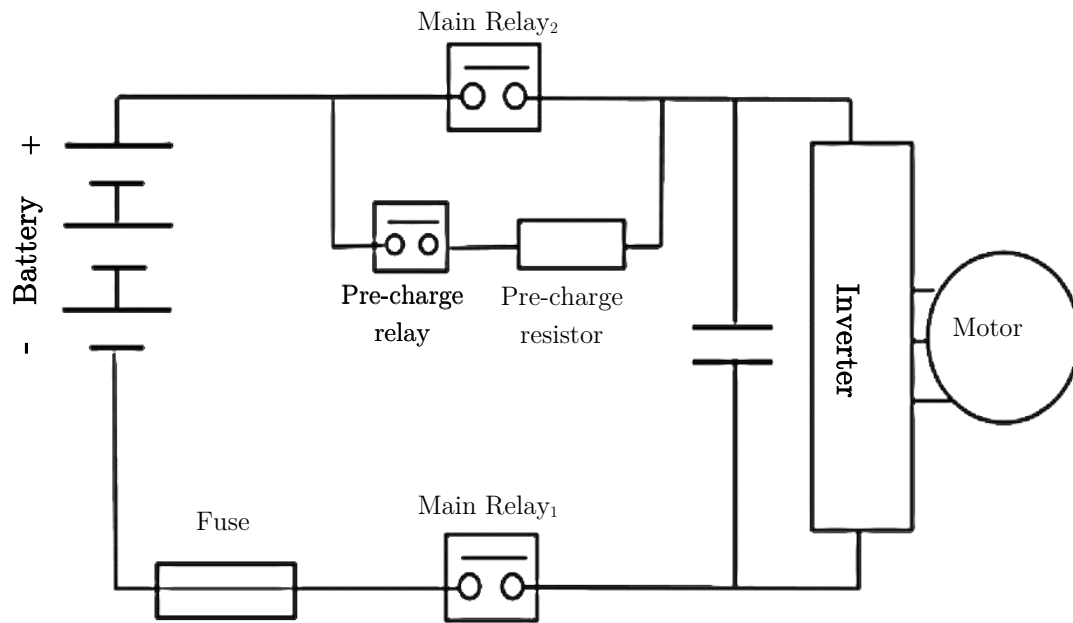
Figure 4: Typical design of BDU, tasked to disconnect the battery and inverter with main relay, pre-charge relay with resistor and fuse *[18]*

The melting (safety) fuse disconnects the current path only in cases of extremely high currents (> 1500 A and short circuit currents up to 16000 A). The fuse melts to be cut-out and thereby protecting the battery and the driving train from the over-current or short circuit current. The nominal rating for the fuse is strongly dependent on the voltage of the battery pack as the conventional EV uses a voltage range of 400 to 600 V. In the future, the importance of the melting fuse will certainly increase because the EV platforms are considering changing to 800 V and higher voltage levels.

The pre-charge circuit consists of a pre-charge relay, a pre-charge resistor, and one main relay. Their connection is configured in such a manner to prevent the damage of the inverter and the main relay due to inrush current. When an EV is turned on, the main relay$_1$ (connecting the negative poles, see ***Figure 4***) turns into a closed state by the controller placed inside the BMS. Shortly after that, the pre-charge relay is closed by the BMS. The inrush current from the battery is reduced by the pre-charge resistor. When the capacitor is completely charged as predetermined time passes, the pre-charge relay will be turned into an open state and the second main relay turns into a closed state. In that way the motor is supplied with AC power converted from DC power by the inverter and the EV can be driven. [3, p. 5]

Thus, the BDU has the function to prevent the damage due to large inrush current or short circuit, it doesn't have a device to protect the circuit form high ambient temperatures and, on the other hand, from the temperature rise due to

Joule heating. Like mentioned before (see **Motivation**), functions of electrical components can be guaranteed to work properly if the ambient temperature is between -40°C and 85°C and the temperature of the components does not rise above 120°C. That is, protection devices against an excessive increase of components temperature are not implemented in conventional BDUs and this may cause damage of components or a complete failure of the BDU. [3, pp. 5, 6]

Redesigning a finished product like BDU to implement another component can be a very expensive venture in many cases other solutions are considered. Those are mostly complex 3D simulation programs that use a lot of CPU processing power and demand large memory storage. Nevertheless, more simple computer simulations can be performed to determine the thermal heating of the different components. The simple programs can use just one input as a parameter for the calculations in that way provide fast and memory-efficient but precise results. In many cases, the electrical current I is used as an input for different calculations and optimizations. Thus, the current level must stay in predefined limits for the complete electrical system of EV to work properly. This is where the batterie's sensors come to play in the performance of the battery as a whole and the importance of current measurement inside the EV.

2.3 Shunts for Current Measurement

While evaluating the efficiency of an electrical system or when analysing the usage of a battery, voltage and current are measured and then power and other parameters are calculated. The accuracy of the derived values (e.g. power) directly depends on the accuracy of the instruments used to measure the initial values. The total error should be kept under 0.1% and at first glance, it seems that current measurement is an uncomplicated operation of applying Ohm's law. With known voltage drop ΔU over the resistor, the passing current is easily calculated using the Ohm's law:

$$I \; = \; \frac{\Delta U}{R} \tag{1}$$

However, conventional measurement devices can often measure just up to 10A. External Current clamps typically only allow moderate measuring accuracies from 0.5 to 1%. Current clamps can be easily installed in the measurement setup, but they have a significant temperature drift and must be manually zeroed at regular intervals. [19] [20]

There are numerous ways to determine the magnitude of the electrical current passing through the components and one of the most frequently used is the

■ife

current measurement using shunt resistors. Shunt resistors are very precise and over a wide range of temperature stable resistors with low ohmic values (as little as few μΩ).

2.3.1. Resistors for Current Measurement in EV

The current measurement resistor, the so-called shunt, has been known for decades. In the meantime, extremely low-resistance, almost error-free resistors, and very precise measurement value acquisition are available. The control and regulation of actuators in the EV usually require currents in the range 1 to 300 A, in special cases up to 600 A for a short time while the vehicle is in operation. On the other hand, while the vehicle is in the idle state just a few mA must be reliably detected. [21]

For resistors with a resistance of 1 Ω and greater, measuring currents in the range of some 100 mA, the voltage drop is evaluated as a direct measure of current (see Equation (1)). But, for currents ranging above 10A, the measuring setup changes because of the general power loss due to Joule heating in the resistor, which cannot be neglected anymore:

$$P_{Loss} = R \cdot I^2$$

(2)

The power loss can be minimized using lower resistance values, but since the voltage drop becomes lower at the same time, the resistance value is often limited by the maximal resolution and quality of the evaluation electronics. [21]

Looking at the resistivity (or conductivity) of metals as a function of temperature T, it is easily noticeable that if the thermal resistance coefficient α is high, the temperature has a great impact on the resistance:

$$R(T) = R_{Ref}[1 + \alpha(T - T_{Ref})]$$

(3)

For an accurate measurement, it is not desirable that a resistor changes predefined ratios, amplitudes, or other set factors due to a change in temperature. Most cheap resistors change 5-10% in an interval of -20°C to 80°C and come with 5-10% tolerances. Quality resistors come with a 0.01% change in resistance over the same temperature interval. Like mentioned before, the shunt develops a voltage drop across its resistance and the current passing through it is, according to Ohm's law, proportional to its resistance. The current path should be affected as little as possible and this is the reason the shunt resistors are in order of a few mΩ or even μΩ. Depending on the magnitude of passing current the voltage drop is also quite small and often requires amplification before being converted by an Analog-to-Digital converter (ADC). [19]

As in *Figure 5* shown, a configuration for measuring the current involves an operational amplifier to amplify the voltage drop across the shunt, an ADC to convert the signal into digital form and a controller. The controller uses the digitized measurement to monitor, optimize, or implement safety protocols to prevent the damage if the current exceeds the predefined limit. [19]
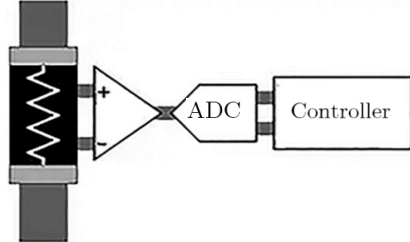
Figure 5: Common signal chain for measuring current flow with shunt resistor [19]

Even if the structure of shunt sounds simple, it consists of three resistances (see *Figure 6),* the resistance of shunt resistor itself, the resistance of shunt's two leads and the leads on the printed circuit board connected to the shunt (which are not shown in the picture). These lead resistances are insignificant, but shunt resistors have very low values and if the magnitude of the current is high, like in modern EV, they can have a significant impact on the measurement.

R_{Lead} R_{Shunt} R_{Lead}

Figure 6: Schematic representation of two-terminal shunt resistor

The possible measurement errors due to lead resistances can be avoided using a Kelvin connection[5] by running separate sense traces (voltage leads) to the terminals of the shunt resistor (see *Figure 7*). These sense traces generate a voltage drop over the shunt to be measured according to the Ohm's law. Because they are placed immediately to the target resistance, the do not include the voltage drop in the force leads or contacts. Since almost no current flows to the measuring instrument, the voltage drop in the sense traces is negligible. [22]

Current

V_-
V_+
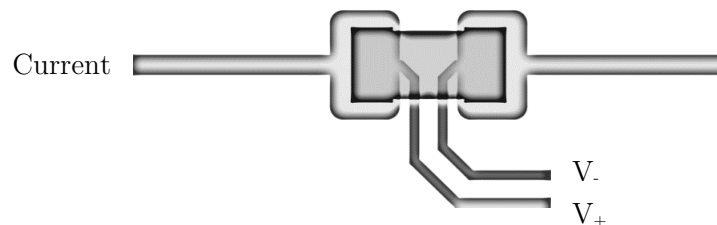
Figure 7: A Kelvin connection to a two-terminal shunt resistor *[22]*

---

[5] Kelvin sensing is also known as four-terminal sensing after William Thomson, Lord Kelvin.

Even this method is widespread it may not be the best option for current sensing where high currents are involved. This is often the case in the EV BDUs, and for this type of measurement, shunts with four terminals, which implement the Kelvin method are used. As visible in *Figure 8* the Kelvin connection with high precision sense traces located very near the shunt sensor, helping to improve the measurement accuracy. The separate terminations for high current flow and voltage measurement are also visible. Using a four-terminal shunt also improves the temperature stability over the two-terminal shunt. [19]
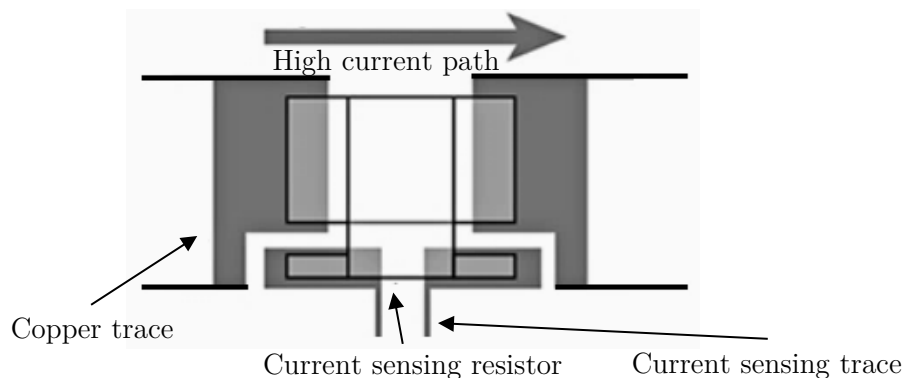
Figure 8: A four-terminal shunt resistor [19]

2.3.2. Manganin and other Resistance Alloys

An electrical resistor can be made of any conductive material. Since the resistance value will depend on parameters such as temperature, time, voltage, frequency, etc., the material should be carefully selected. Ideally, the measuring resistor should be completely independent of these parameters, which of course does not exist. The real resistance is described by the properties such as temperature coefficient, long-term stability, thermal voltage, load capacity, inductance, linearity, etc. Some of these properties are essentially material-related, others are strongly influenced by the design. [21]

In modern EV the currents are too high (ranging up to 800 A) for conventional ammeters, implying that different measurement setup is needed. The solution is to place the ammeter in parallel with a precision resistor, called a shunt resistor. The high precision shunt resistor has a low ohmic value and is usually made from an alloy of copper, manganese, and nickel. This alloy, called manganin, was discovered in 1892 and was an improvement over constantan, an alloy of copper and nickel. Manganin has its melting point at 1020°C and maximum usage ambient temperature limited to around 140°C, which makes it a perfect choice for EV BDUs' current sensing. It has a very low coefficient of thermal resistance $\alpha = 0.00001$ K^{-1} (10 ppm/K), in other words, its resistance has a wide range of temperatures where it remains almost constant.

$$\alpha = \frac{R(T) - R(T_{Ref})}{R(T_{Ref})} \cdot \frac{1}{T - T_{Ref}} = \frac{\Delta R}{R(T_{Ref})} \cdot \frac{1}{\Delta T} \qquad (4)$$

For comparison, a different resistor with $\alpha = 200$ ppm/K for a temperature change of $\Delta T = 50$ K (or °C) would have a relative resistance change of more than 2%, which is enough for 1% limit. Even more extreme is using copper resistors for measuring because copper has $\alpha = 4000$ ppm/K (or 0.4 %/K) and ΔT of just 10 K, already causes a drift more than 4%. [21]

The reference temperature T_{Ref} is usually 20°C and because there is some resistance dependency of manganin for different temperatures (see *Figure 9*) it is necessary to indicate the upper temperature while measuring (e.g. T = 300K or 27°C).
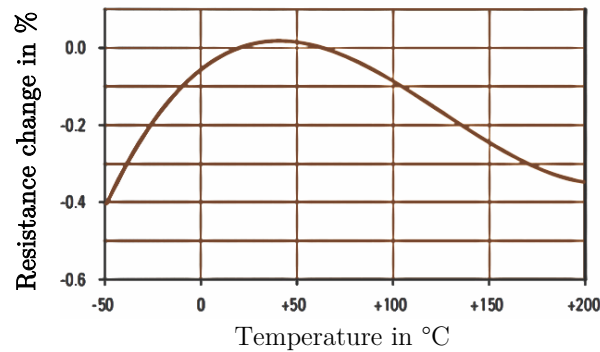
Figure 9: Manganin resistance over temperature from -50°C to 200°C

With the improvements of offset, temperature coefficient and noise of operational amplifiers (see *Figure 5*), the resistance values of shunts are reduced to lower μΩ range and the problem with power dissipation (Equation (2)) is minimised. However, the measurement error caused by interference or thermal voltages increases, and the importance of low inductance and low thermal voltage becomes important.

Stability over time is extremely important for a shunt resistor because the user wants to be able to rely on calibration once, even after years of use. For the resistance materials, this means that they must be corrosion-resistant and must not undergo any metallurgical-related conversions during their service life. The alloy manganin meets these requirements as homogeneously mixed crystal alloy, which is besides carefully annealed and stabilized.

2.3.3. Impact of Temperature on Current Measurement

Temperature stability is very important because as underlined before (see **Introduction**) the current generates heat in the resistor as a consequence of Joule heating[6]. The energy transfer (or heat transfer) Q, results in an increase of the object's temperature ΔT as following equation states:

$$Q \; = \; m \cdot c \cdot \Delta T \tag{5}$$

The energy dissipated is then absorbed by the thereby components and the gas inside the BDU and the component, through which the current is passing, is heated up as well. The rate at which the components (or resistor) dissipate energy:

$$P_{Loss} \; = \; \Delta V \cdot I \tag{6}$$

After an amount of time t has elapsed, the energy dissipated in the resistor is:

$$E \; = \; P_{Loss} \cdot t \; = \; \Delta V \cdot I \cdot t \tag{7}$$

Assuming an ideal system[7] with constant pressure, considering Equation (5) and (7), follows:

$$Q \; = \; E$$

$$m \cdot c_p \cdot \Delta T \; = \; \Delta V \cdot I \cdot t \; = \; I^2 \cdot R \cdot t$$

$$\Delta T \; = \; \frac{I^2 \cdot R \cdot t}{m \cdot c_p} \tag{8}$$

Considering the Equation (8) it is easily noticeable, that the temperature rise is directly proportional to the square of current passing through the shunt resistance R and inversely proportional to the thermal mass $C_{th} = m \cdot c_p$ of the component. Using the real-world example in ***Figure 10***, under ideal assumptions, the temperature in the shunt resistor would rise very quickly as shown in ***Figure 11***.

---

[6] For definition please refer to **3.**

[7] System where all electrical energy is converted into thermal energy and there are no losses through conduction, convection, or radiation.
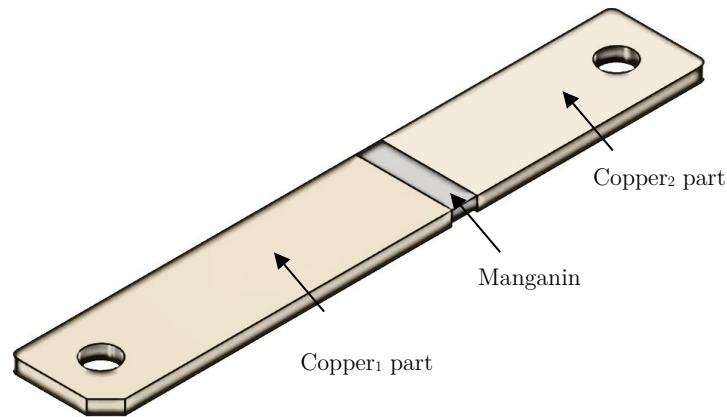
Figure 10: CAD Drawing of one of the Samsung SDI shunts used for testing. The width of the used shunt was 20 mm, the thickness of 3 mm, and the length 125 mm. Manganin part was just 5.3 mm in length where copper parts ware 70.3 mm and 46.4 mm, respectively.
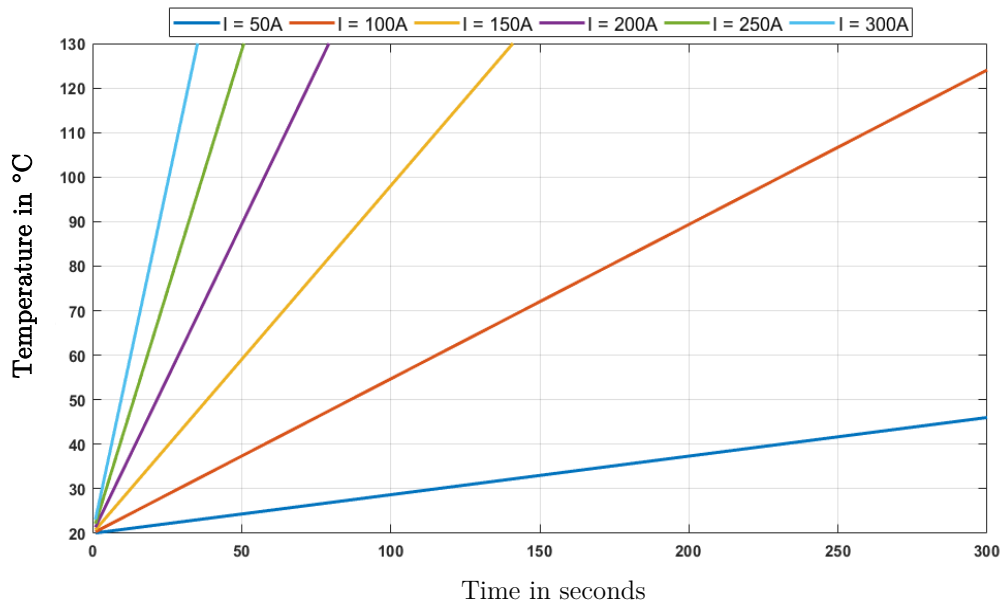
Figure 11: Temperature of the shunt as a function of time for different currents. The maximal temperature of 120°C is reached in just 32 seconds for 300 A, in 46 seconds for 250 A and in 287 seconds for 100 A.

The shunt's temperature should not rise above 120°C for the shunt to have high long-term stability of electrical resistance, which is very important for current measurements. Thus, when shunt resistors are designed the chemical composition of manganin is chosen so that the peak will occur in the operating temperature range. Usually, the shunts in EV applications carry high currents and have peak operation temperature between 45°C and 65°C. Manganin is susceptible to selective oxidation or preferential corrosive attack and exceeding the maximum

working temperature may result in a resistance drift and generate by oxidizing processes on manganin surface. [23]

Oxidizing processes on manganin are not the only type of problem due to thermal generation during current measurement, but also thermal voltages that can have a significant impact, especially at higher temperatures. The shunt is made up of different materials and in this case from copper and manganin part, and if there is a temperature gradient between connections of those different materials, a thermal voltage is generated. In electrical engineering, thermal voltage is an electrical voltage caused by temperature difference in conduction material.

If there is a temperature difference between two materials of the same conductor (e.g. the shunt used for measurements in *Figure 10*), as a consequence of that terminal voltage is generated. This potential difference is a function of temperature drift along the conductor and depends on its material. The value and the sign of the thermal voltage U_{th} are determined by the product of the temperature difference ΔT and the Seebeck coefficient S:

$$U_{th} = S \cdot \Delta T \tag{9}$$

Seebeck coefficient can be understood as voltage build-up when a small temperature gradient is applied to the conductor, and when the conductor's material has come to a steady-state where the current density $J = 0$ Am^{-2}. In general form, the Seebeck coefficient is defined as a vector[8] differential equation: [24]

$$\boldsymbol{J} = -\sigma_{el}(\boldsymbol{\nabla}V - S\boldsymbol{\nabla}T)$$

$$0 = -\sigma_{el}(\boldsymbol{\nabla}V - S\boldsymbol{\nabla}T) \ \rightarrow \ S = \frac{\boldsymbol{\nabla}V}{\boldsymbol{\nabla}T} \tag{10}$$

Interestingly, the voltage expressed by the Seebeck effect cannot be measured directly, since by attaching the voltmeter an additional voltage contribution takes place, due to the temperature gradient and Seebeck effect in measurement leads of the voltmeter (see *Figure 12*). Therefore, the measured Seebeck coefficient is a contribution from the Seebeck coefficient of the material of interest and the material of the measurement electrodes[9]. The measured Seebeck coefficient can then be written as:

$$S = S_1 - S_2 = \frac{1}{\Delta T}(V_2 - V_1) \tag{11}$$

---

[8] The vector values are denoted in **bold**.

[9] This arrangement of two conducting materials is known as a thermocouple.

■ife

The Seebeck coefficient S depends on the material (mostly metal or alloy), the absolute temperature, and the purity (lattice defects, contamination) of the materials. In following **Table 2** there are Seebeck coefficients for some materials:

Material	S μVK^{-1}
Constatan	-35
Manganin	0.6
Aluminium	3.5
Copper	6.5
Nickle-Chrome	25

Table 2: Seebeck coefficients for common materials relative to Platin at $T = 273.15$ K
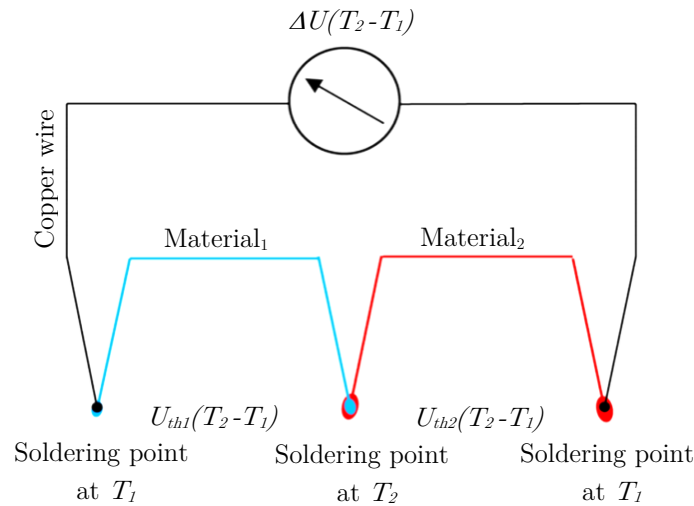
Figure 12: Seebeck effect of a combination of two different materials

This effect is particularly important for low-impedance resistors since very small voltages must be measured and therefore thermal voltages U_{th} in the μV range can falsify the result. Analysing the shunt used in tests (see **Figure 10**) the resistance of manganin part is:

$$R_{Manganin} = \frac{1}{\sigma_{el}} \frac{L_{Manganin}}{A_{Shunt}} \bigg|_{\substack{L_{Manganin} = 5.3\text{mm} \\ A_{Shunt} = 0.6\mu\text{m}^2}} \approx 0.38 \ \mu\Omega \tag{12}$$

and current I in range of 100 A, then the voltage drop over shunt is:

$$U = I \cdot R_{Manganin} = 38 \ \mu\text{V} \tag{13}$$

which implies that thermal voltages cannot be neglected.

2.3.4. Impact of Inductance Current Measurement

In many EV applications, the current must be measured in defined intervals and the inductance of the shunt or measuring circuit is of great importance. The shunt resistors are manufactured as low inductance as a flat version with no or with closely spaced meanders. The diamagnetic property of precision alloys like manganin, the metallic substrate, and the four-wire (Kelvin) connection further contribute to the improvement. Using the four-wire connection (see *Figure 8*), the sense lines together with the resistor from an antenna in which a magnetic field is generated. The induction voltage is generated by the current flow and other external changes in the magnetic field. It is particularly important to keep the area enclosed by the sense lines as small as possible. [21]

2.3.5. Low total Resistance of Shunt

To use a shunt made entirely of manganin (see *Figure 13)* is not the best option, because the total resistance, measured using the four-wire method, is sometimes 2 to 3 times higher than actual measuring resistance. Correspondingly the power loss is higher, and the resistor is heated up more which leads to higher thermal voltage. [21]

Figure 13: Shunt used for testing made out from one stamped sheet of manganin

These errors are largely eliminated in the case of resistors stamped from a composite material (see *Figure 14*). The total resistance is increased by less than 10% and the user can rely on proven Cu-Cu connection technologies.

Figure 14: Actual shunt used for testing stamped from two sheet of copper and one sheet of manganin

2.4 Application of Relays in EV

EV relays operate in conjunction with fuses to shut off a circuit safely and securely in the event of an error or accident. A typical application in the EV is to place the main relays in primary circuits positioned between the battery and inverter (see *Figure 15* marked in green where the function of pre-charge relay was described in **Battery Disconnect Unit**). The EV contains several other relays (see *Figure 15* marked in pink and orange) that perform different functions like controlling rapid charging and high voltage accessory equipment, respectively. They are smaller in size and operating voltage.
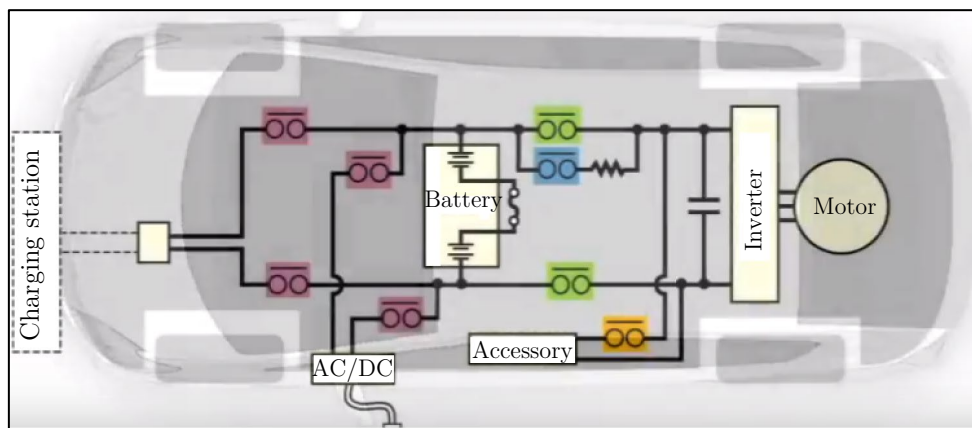
Figure 15: Position of HVDC relays in EV *[25]*

To ensure normal switching on-off of EV, high-voltage direct current (HVDC) relays must be installed between the battery system and the inverter (see *Figure 2*). When the EV is turned on the HVDC relays ensure a secure connection and when the EV stops they isolate. In case of emergency, they must operate as fast as possible and protect the user. HVDC relays are the key safety devices of EV and without them, the vehicle would not start, drive, or stop (see *Figure 16*).
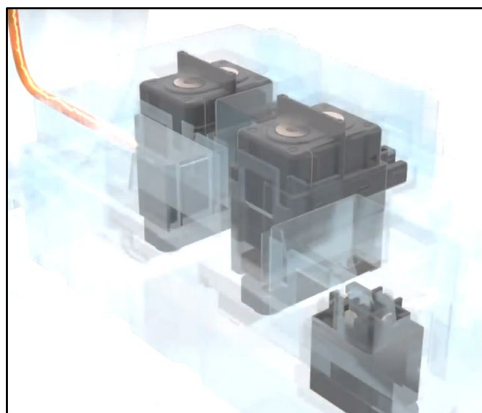
Figure 16: Position of the relays inside a typical EV BDU *[26]*

The electrical life expectancy of power relays used in Samsung SDI testing is generally rated to be $2 \cdot 10^5$ operations, while mechanical life expectancy maybe 10^6 or even 10^7 operations. The reason electrical life is rated so low compared with mechanical life is that contact life is application dependent. The electrical rating applies to contacts switching their rated loads. Correspondingly, when the relay switches a load less than the rated value, contact life may be significantly greater. [27]

2.4.1. Basic Functions of High Voltage DC Relay

As a key safety device, the HVDC relay should have the basic functions of *high voltage resistance, load resistance, impact resistance,* and *strong braking ability.*

- **High voltage resistance**

The working platform voltage of EV is higher than 12-24 V of a traditional vehicle, so its high voltage DC relay is required to withstand high working voltage and reliable closing and breaking high voltage load.

- **Load resistance**

Peak power of EV motor is far over 60 kW and for buses over 160 kW and corresponding to the mentioned voltage platforms the currents reach from 100 to 300 A, respectively. The HVDC relay must have strong load-resisting capacity while the volume of the relay must be as small as possible, because the smaller the device, the lower the cost.

- **Impact resistance**

When the EV is started the HVDC relay must not only withstand high voltage and but also huge inrush current because of capacitive load (please refer to **Battery Disconnect Unit**). This current is usually several times to tens of times of rated current of load and can cause contact adhesion or even relay contact separation. This can lead to serious damages to vehicles or even human death. Therefore, HVDC relays must have good impact resistance.

- **Strong braking ability**

In case of accident or electrical system failure (e.g. short circuit), the HVDC relays in the BDU of EV must be able to cut off the fault current as fast as possible without causing the relay to explode or contact adhesion. This requires relay contacts to be able to cut off smoothly under the extremely high current and therefore have good impact and adhesion resistance. [28]

2.4.2. Undesirable phenomena occurring in EV relays

Electric arcing occurs while contact under high voltage is closing or breaking. It is an unwanted phenomenon that greatly reduces the lifespan of EV relays. It is extensively searched for new methods to reduce arc energy and damage to the contacts, and therefore extend the life of EV relays. From an application point of view, the most widely used HVDC relays are *vacuum* and *gas-filled* relays.

The vacuum is an ideal insulator and therefore the electric arc, which happens because of gas ionization, cannot be generated between the contacts. Nevertheless, a complete vacuum is only an ideal state and between the contacts in the arc chamber (see *Figure 17*) will be some residual oxygen (O_2). In the case of arc, the oxygen will form a copper oxide with the copper electrode. The contact resistance will increase, and the relay will be at risk of failure.

Gas-filled HVDC relays are mainly used in today's EV applications. The gas-filled refers to hydrogen (H_2) or nitrogen (N_2) gas compressed in the arc chamber (see *Figure 18*). Pure H_2 is difficult to ionize and in combination with a deflection, a magnet is a better option than a vacuum relay. [28]
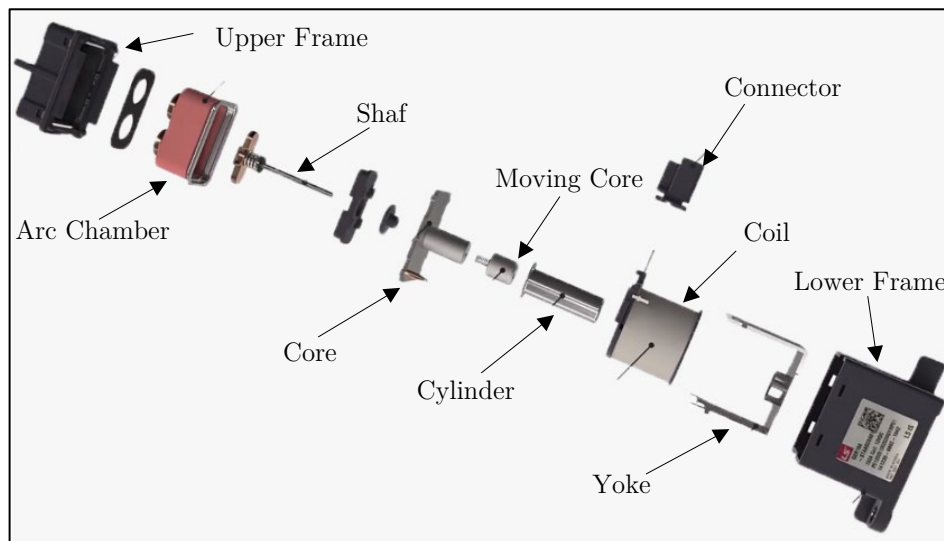
Figure 17: Structural arrangement of a typical EV relay *[26]*

Hydrogen sealed technology has been used in mass production of hybrid and EV since 1997. The sealed structure provides greater safety when switching off high DC voltages and, in that way, eliminates arcing space requirements. The capsule contact design ensures a dust-free and waterproof environment, eliminating oxidation and providing reliable contact performance over an extended time.
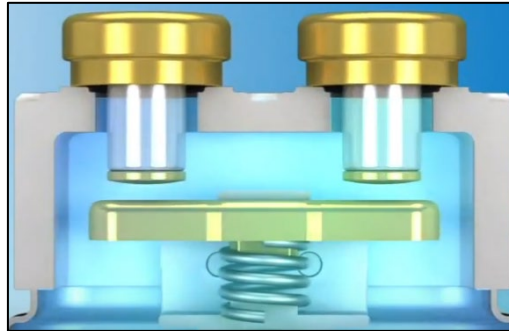
Figure 18: Hermetically sealed arc chamber containing pressured H_2 *[25]*

The integrated capsule contact block is enclosed by permanent magnets. The benefit of capsule contact block with the hydrogen-filled chamber and magnetic field is that hydrogen gas quickly cools arcing when it occurs (see ***Figure 19***). This cooling mechanism allows a quick shut down of potentially high DC voltages. The presence of the magnetic field inside the EV relays forces the arc to displace and stretch along the edges of chamber walls (see ***Figure 19***).
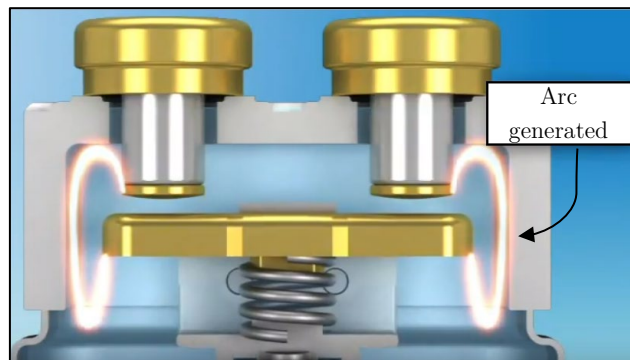
Figure 19: Electric arc generated between HVDC relay contacts while shutting off in an arc chamber with hydrogen sealing. The arc is "stretched" along the arc chamber walls because of the presence of a magnetic field. This allows that the arc is extinguished as quickly as possible. *[25]*

As stated before, electric arcing can shorten the contact life of the HV relay significantly. By the use of appropriate arc suppression, contact life may be lengthened. An arc will ignite if both minimum arc voltage and current are exceeded. At the voltage and current values of less than those required to ignite an arc, a spark may occur between separating contacts. This spark is a capacitive discharge and is weak compared with an arc. Even so, the spark may be enough to keep sulfidation, oxidation, and contaminates from building up on the contacts. Contact life is terminated when the contacts stick or weld, or when excessive material is lost from one or both contacts and good electrical contact is not possible. These conditions are the result of cumulative material transfer during successive switching operations, and material loss due to splattering. [27]

Material loss and *material transfer* occur as a result of heat:

$$Q = I^2 R \tag{14}$$

The current flowing through this constricted area generates heat Q, which causes contact material to melt and lose material. Material loss and transfer occur even more while arcing because more energy is being generated. Such loss can be significant throughout thousands of relay operations and different load applying. [27]

On the other hand, it can be beneficial to control electrical arcing because short term arcing can burn off the build-up deposits on contacts. For this reason, it is best to apply general-purpose and power relays only in applications where load voltage and current is more than the arc voltage and current ratings of those contacts. [27]

2.4.3. Contact Protection of EV Relays

When the relay contact begins to separate and an electric arc ignites (see *Figure 19*), the most popular method of extinguishing the arc is with an RC-Network placed directly across the contacts (see *Figure 20*). Load current feeding the arc will be redirected into the capacitor C, through the resistance R, taking away some of the arc energy. In such a way, the arc duration is shortened, and the loss of contact material will be reduced. [27]
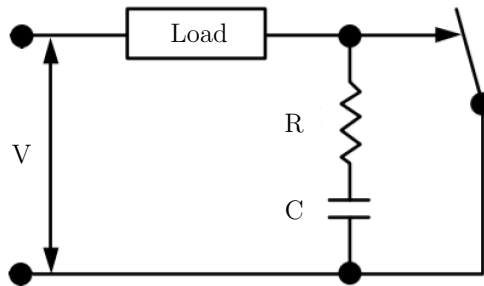
Figure 20: RC-Network for protecting relay contacts from electrical arcing

An ideal arc suppression method would simply be just capacitor C, placed directly across the contacts. However, with no resistance R, in the circuit, the discharge current would not be limited, causing a brief, but severe arc that may cause welded contacts, depending on contact material. Thus, using a large resistance R could produce a negative effect, isolating the capacitance C. The resistance R should be carefully selected and kept as small as possible.

3 Measurement Setup

Thermal modelling of different safety components (e.g. shunts and relays) placed inside Samsung SDI BDUs depends completely on the conducted test measurements. Without measurement data, the verification of the thermal model could not be possible and thus the thermal model itself would be unusable. Nevertheless, it is important to conduct a detailed measurement report, so that the test can be reproduced without making any mistakes. The following *Chapters 3.1* and *3.2* are based on the measurement test report and the values obtained therefrom. The tests were performed at Samsung SDI premises and all data and the pictures are the property of the same.

3.1 Measurements on shunts

For the BDU test, several components were tested. **Table 3** below summarizes the four different shunts connected with busbars of different cross-sections forming the test setup. The main objective of the test was to show the temperature behaviour of the different components, where the thermocouples were used for temperature measurement of the busbars and shunts.

Shunt No.	Dimensions L; a; b [mm]	Busbar No.	Dimensions L; a; b [mm]
A	125; 20; 3	1	500; 20; 2
		2	500; 20; 3
B	125; 20; 2.6	3	500; 20; 4
C	72; 31; 3	4	500; 30; 3
		5	500; 30; 4
D	125; 36; 2.6	6	500; 30; 5

Table 3: Different shunts and busbars used during tests. For easier interpretation of the table: e.g. shunt$_A$ was connected to busbar 1, 2 and 3 during tests, etc. *[29]*

The busbars are made from copper and the shunts, as described in *Chapter 2.3.5,* from copper and manganin. For a better overview of actual shunts and busbars used please refer to *Figure 21*.

■ife

Figure 21: Shunts A to D from top to bottom (on the left) and busbars 1 to 6 (on the right) *[29]*

3.1.1.   Test Description for Shunts

The BDU Test was performed using a high current power supply (PSU) with a maximal output current of 3000 A. The temperatures sensors were connected to CAN measurement modules. To give a better overview of the whole test, the following test sequence was performed:

i.   The desired combination of shunt and busbar was mounted to the high-power PSU (see **Table 3**).

ii. The resistance of the shunts, busbars, and the whole component arrangement was done before the test.

iii. To mimic the actual BDU environment, the shunt was covered with the provided BDU housing (see *Figure 23*).

iv. Test current was applied in the following sequence:
100/150/200/250/300/500/750/1000/1500/2000 A

v.   Following *breaking criteria* were considered:

    a.   Stop the test when the maximum temperature of 120°C was reached or the temperature rise was <1°C in 15 min interval.

    b.   Cooldown until every temperature sensor reaches the start temperature of 25°C

The output current from the high-power PSU had to be measured with high precision and with its wide current output interval, an ammeter could not be used. Instead, the current was measured using high precision shunt with $\Delta U = 60mV$ for $I = 600$ A. The principle of current measurement over the shunt resistor as described in *Chapter 2.3.* A general overview of the whole testing setup is shown in *Figure 22* and *Figure 23*.

■ife
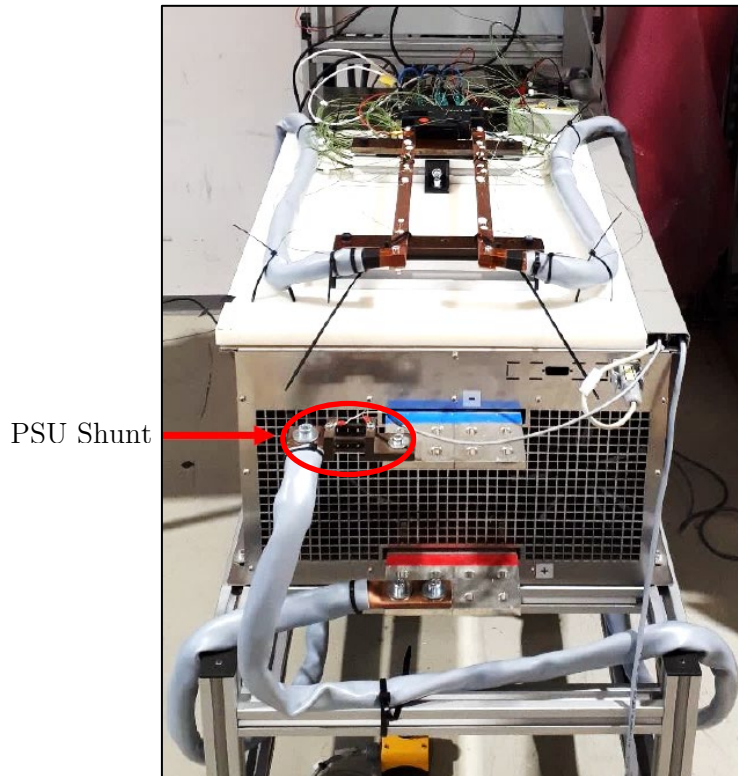
Figure 22: Test setup overview with current PSU with mounted cables and the shunt *[29]*
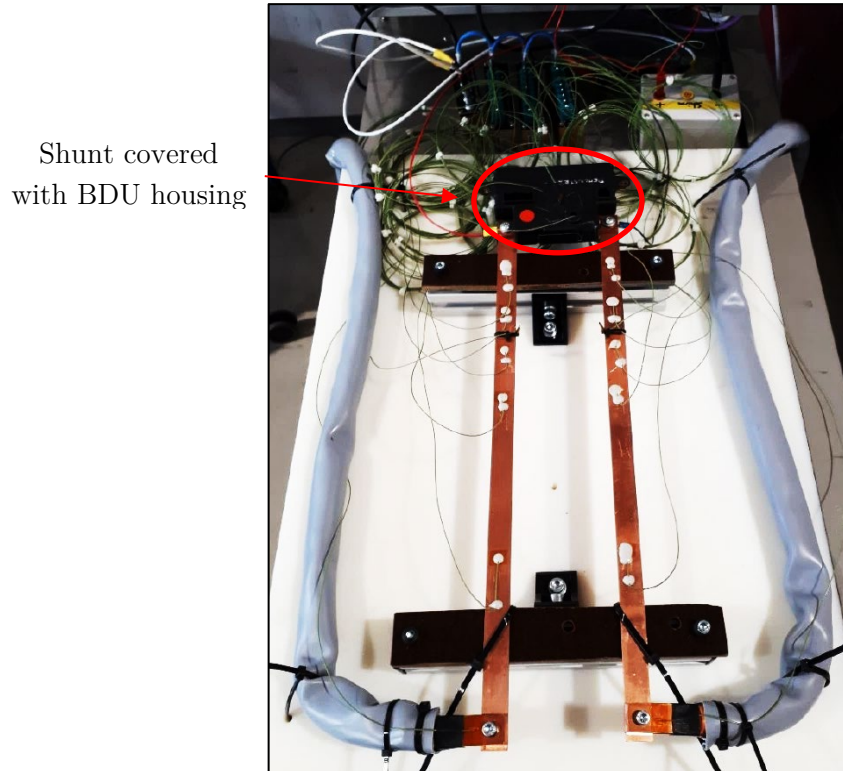
Figure 23: Test setup with busbars connected shunt covered with BDU housing *[29]*

3.1.2. Allocation of the Thermocouples

For the temperature measurements at different locations, 24 thermocouples were used. The thermocouples consist of two dissimilar electrical conductors forming an electrical junction (e.g. a point/area where multiple conductors make physical contact). Because of the different electrical conductivity properties of the conductors a temperature-dependent voltage U_{th} is generated as a result of the thermoelectric effect (see *Chapter 2.3.3*). The generated thermal voltage U_{th} was used as input to three THMM temperature measurement modules with 8 signal inputs.

Because of the limited number of the thermocouples, their placement had to be carefully considered. The governing idea was to place them closer where the temperature changes a lot and leave more space between where the temperature did not differ a lot. Because the busbars and parts of the shunts are made from copper with good *electrical* and *thermal* conductivity, the attention was devoted to the manganin part with rather low electrical and thermal conductivity. The comparison between the important material properties of these two materials is given in *Table 4*.

Material property	Symbol	Unit	Manganin	Copper
Melting point	-	°C	960	1085
Density	ρ	kg/m^3	8400	8940
Electrical resistivity	ρ_{el}	$p\Omega \cdot m$	430	1.72
Specific heat capacity	c_p	$J/kg \cdot K$	410	386
Thermal conductivity	k	$W/m \cdot K$	22	398
Resistivity temp. coeff.	α	$1/K$	0.00001	0.0039

Table 4: Material properties comparison between manganin and copper

Looking at the table above, electrical resistivity $\rho_{el,M}$ of manganin[10] (M) is 250 times that of copper. For the same length *L,* cross-section *A,* and current *I* for the two materials the dissipated power P_{Loss} would be:

$$\frac{P_{Loss,M}}{P_{Loss,Cu}} = \frac{\cancel{I}^2 \cdot \rho_{el,M} \frac{\cancel{L}}{\cancel{A}}}{\cancel{I}^2 \cdot \rho_{el,Cu} \frac{\cancel{L}}{\cancel{A}}} = 250$$

---

[10] The copper alloy manganin does not have a unique (chemical) symbol used. The chemical formula of this substance is CuMnNi, but in this paper the symbol *"M"* will be used.

■ife

For a unit of time *t,* the manganin dissipates 250 times the heat of copper. Thus, the manganin part of the shunt has been expected to heat up the most and so more thermocouples have been placed in its proximity (see **Figure 24**). On the two busbars, the thermocouples have been placed every 50 mm to the 200 mm mark and one thermocouple has been placed at 350 mm from the screw connection (see **Figure 25**).
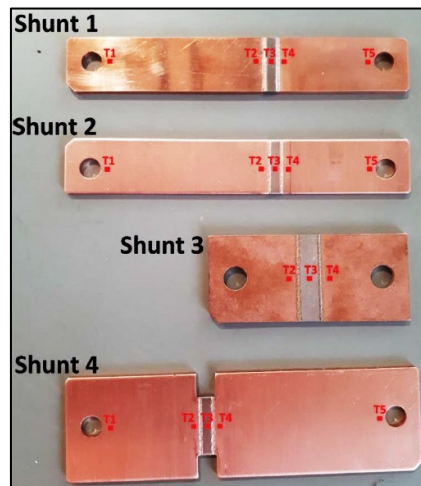
Figure 24: Shunt thermocouples position *[29]*
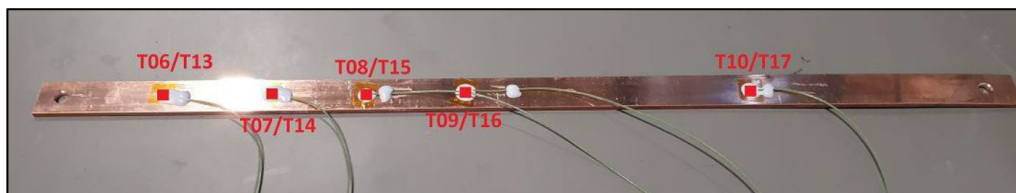
Figure 25: Busbar thermocouples position *[29]*

Besides the measured temperatures on the shunts and busbars, it was necessary to measure the ambient temperature (e.g. room air) and the temperature inside the BDU housing. These temperatures are were used for the thermal model generation and the calculation of heat transported via *convection* and *radiation* (see **Chapter 4.1.2** and **4.1.3**).

Figure 26: Thermocouple inside the BDU housing (on the left) and outside the BDU with 1 cm distance (on the right) *[29]*

Table 5 should give the reader a better overview of the allocation of different thermocouples.

Thermocouple No.	Position	Thermocouple No.	Position
T01	Shunt	T13	BB -
T02	Shunt	T14	BB -
T03	Shunt	T15	BB -
T04	Shunt	T16	BB -
T05	Shunt	T17	BB -
T06	BB +	T18	BB - (on the PSU cable)
T07	BB +	T19	BB - (Air between T14 and T15)
T08	BB +	T20	BDU housing inside
T09	BB +	T21	BDU housing outside
T10	BB +	T22	BDU housing 1cm distance
T11	BB + (on the PSU cable)	T23	-
T12	BB + (Air between T07 and T08)	T24	Room temperature

Table 5: Allocation of the thermocouples *[29]*

3.1.3. Measurement of Transition Resistances

To obtain the heat generated $\dot{E}_g$ (see **Chapter 4.1.4**) in the test setup, it was necessary to measure the transition resistances of the shunts and the busbars. The used conductors had small cross-sections and good electrical conductivity, and because of that, resistances in the range of few $\mu\Omega$ were expected. Because of that, the Megger Low Resistance Ohmmeter was the device of choice with a measuring range of 0.1 $\mu\Omega$ - 1.999 Ω. The transition resistances were obtained using the four-wire method (see **Figure 27** and **Table 6**). The principle and benefits of the four-wire (or Kelvin method) was explained in **Chapter 2.3.1.**

Figure 27: Shunt transition resistance measurement (on the left) and manganin transition resistance measurement (on the right). Note how the voltage clamps are always placed "inside" the larger current clamps. *[29]*

| Shunt No.	Transition resistance whole shunt in μΩ	Transition resistance manganin in μΩ
A	77.77	44.2
B	84.97	46.03
C	59.33	50.63
D	72.47	49.67

Table 6: Shunt transition resistances *[29]*

The transition resistance of the whole test setup (busbar and shunt) was measured using the four-wire method, where the current clamps of the Megger device were placed on the PSU cable and the voltage clamps at the beginning of the busbars. The busbars were not measured separately because their resistance could be easily calculated, having the same length, and known shunt resistance. **Table 7** summarises the transition resistances of the whole test setup.

Shunt No.	Busbar cross-section mm^2	Transition resistance μΩ
A	40	507.4
A	60	348.8
A	80	303.6
B	40	517.6
B	60	389.2
B	80	325.3
C	90	243.8
C	120	214.8
C	150	166.5
D	90	340.9
D	120	212.8
D	150	192.5

Table 7: Measurement of the transition resistances *[29]*

Looking at **Table 7** it is interesting to notice how the transition resistances of the whole test setup decrease with the increase of the cross-sections. For example, the 80 mm^2 busbar setup has approximately 2 times greater resistance than the 150 mm^2 busbar setup, because the ohmic resistance is inversely proportional to the cross-section surface.

■ife

3.2 Measurements on Relays

The BDU relay tests should[11] be performed on several relays. **Table 8** below summarizes the three different relays connected with busbars of different cross-sections forming the test setup. The main objective of the test was to show the temperature behaviour on the different positions on the relay (see *Figure 31*). As for the shunt measurements, the same thermocouples were used for temperature measurement.

Relay No.	Name	Nominal Current A	Busbar No.	Dimensions L; a; b [mm]
1	Supplier A	120	1	500; 20; 2
			2	500; 20; 3
			3	500; 30; 3
2	Supplier B	250	1	500; 20; 3
			2	500; 30; 3
			4	500; 30; 5
3	Supplier B	300	4	500; 30; 5
			5	500; 40; 5
			6	500; 50; 5

Table 8: Different relays and busbars used during tests. *[29]*
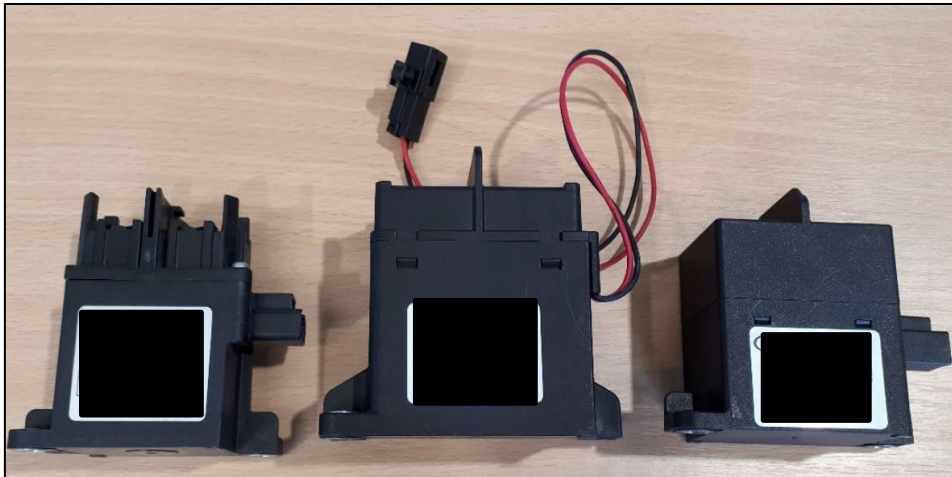
Figure 28: Overview of different relays used *[29]*

---

[11] Due to the unexpected situation with the COVID-19 virus, which inevitably postponed all the planed deadlines, the tests were conducted on only one relay from Supplier A.

3.2.1. Test Description for Relays

As for the shunts, the BDU relay test was performed using the PSU. Following test sequence during measurements was performed:

i.   The desired combination of shunt and busbar was mounted to the PSU (see **Table 8**). Unfortunately, because of the unexpected situation regarding the COVID-19 virus, the test was only conducted on the Supplier A relay with a 40 mm² connected busbar.

ii. The resistance of the relay and the whole component arrangement was done before the test.

iii. Following parameters were measured:
     a.   Temperatures in different positions
     b.   Current and relay contact voltage drop

iv. Test current was applied in the following sequence:
     50%, 75%, 100%, 125%, 140%, 175% and 200% of the nominal relay current (see **Table 8**).

v.   Following breaking criteria were considered:
     a.   Stop the test when the maximum temperature of 150°C was reached or the temperature rise was <1°C in 15 min interval.
     b.   Cooldown until every temperature sensor reaches the start temperature of 25°C (except relay housing thermocouples)

Because the current was used as input for the developed thermal models, it must be measured with high precision. As for the shunts, the current was measured with over a high precision shunt resistor with $\Delta U = 60mV$ for $I = 600A$. The principle of current measurement over the shunt resistor as described in *Chapter 2.3.* A general overview of the whole testing setup is shown in *Figure 29* and *Figure 30*.
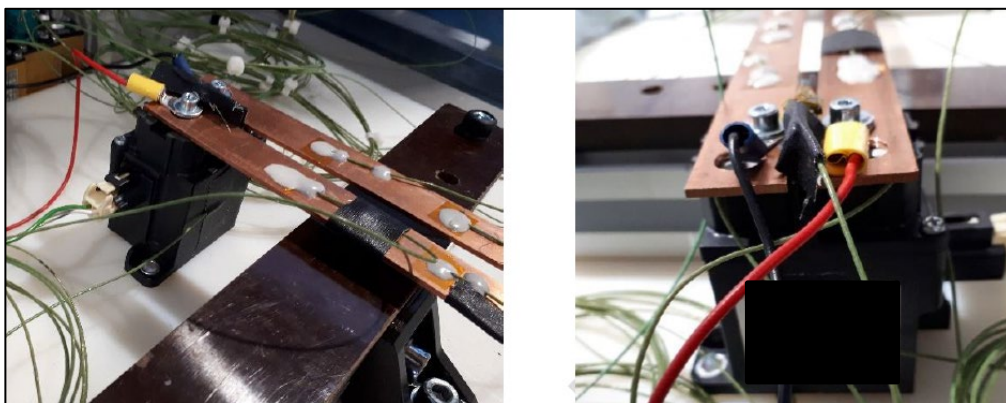
Figure 29: Relay test setup side view and test setup from the back view *[29]*
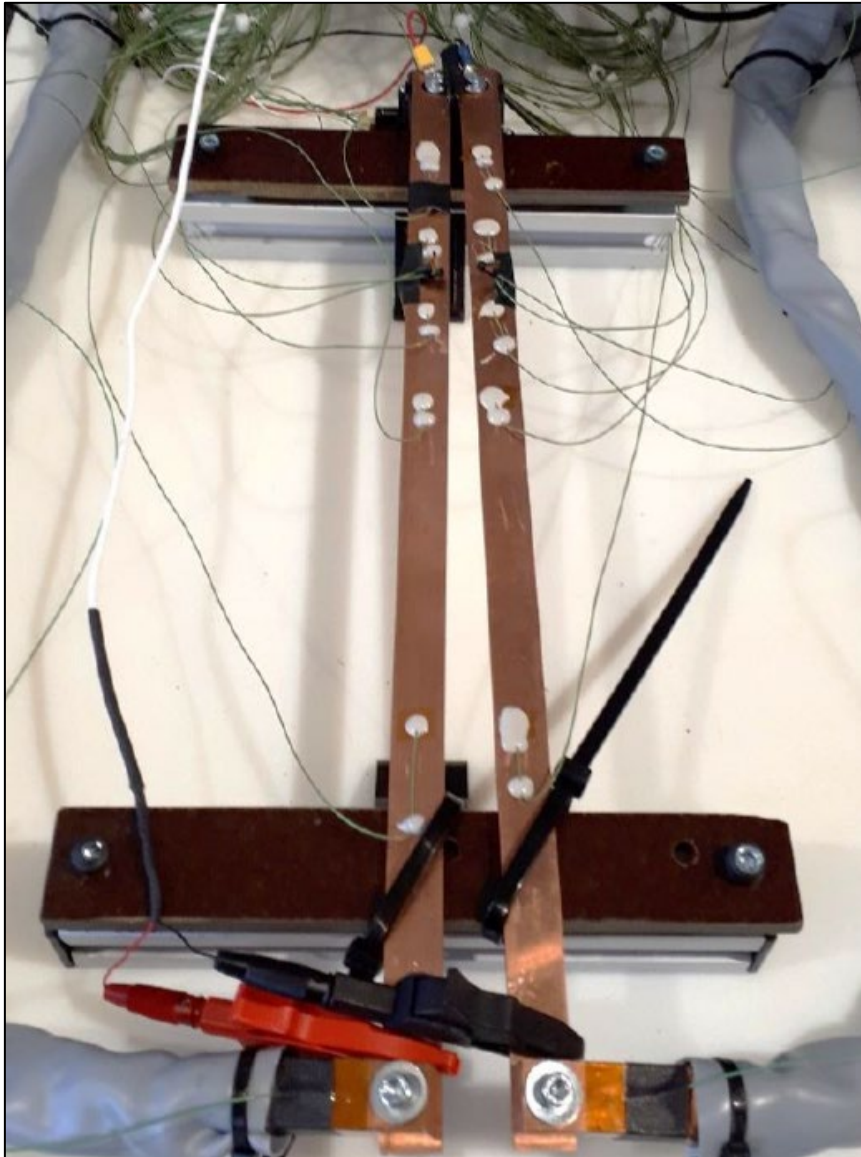
Figure 30: Relay test setup with connected 40 mm² cross-section busbars. *[29]*

3.2.2. Allocation of the Thermocouples

During temperature measurement, a total of 20 thermocouples were used. The thermocouples were placed on 5 different places on the relay (see *Figure 31*) and for the busbar, the same placement was done as for the shunt measurements (see *Figure 32)*. Because the used relay is hermetically sealed, no thermocouples could be placed inside the relay. Another difference to the shunt measurements is that there is no manganin involved.
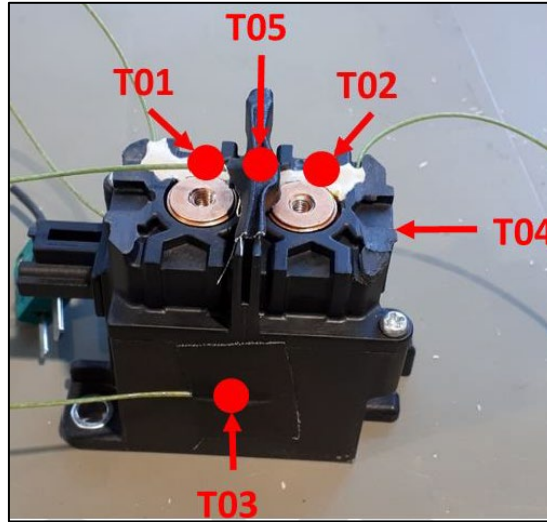
Figure 31: Relay thermocouple position *[29]*

Figure 32*: Busbar thermocouples position [29]*

Table 9 below summarises the position of thermocouples during relay measurements.

Thermocouple No.	Position	Thermocouple No.	Position
T01	Relay Contact+ side	T11	BB + (on the PSU cable)
T02	Relay Contact- side	T12	Not used
T03	Relay Contact inner side	T13	BB -
T04	Relay Contact outer side	T14	BB -
T05	Relay Contact top	T15	BB -
T06	BB +	T16	BB -
T07	BB +	T17	BB -
T08	BB +	T18	BB - (on the PSU cable)
T09	BB +	T19	Not used
T10	BB +	T20	Room Temperature

Table 9: Allocation of thermocouples used for relay measurements *[29]*

3.2.3. Measurements of transition resistances

The transition resistance test was performed with a Megger Low Resistance Ohm-meter and the transition resistances were obtained using the four-wire method (see *Figure 33*). The principle and benefits of the four-wire (or Kelvin method) was explained in *Chapter 2.3.1*.
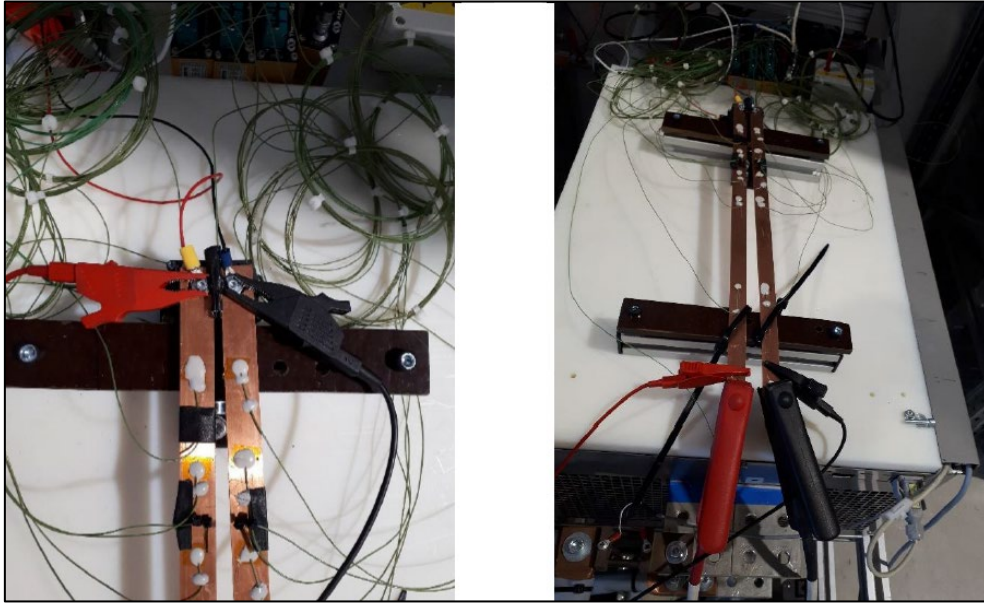
Figure 33: Transition resistance of relay and transition resistance of the whole test setup. *[29]*

Looking at **Table 10** there is a noticeable difference in resistances before and after the test for the relay itself as for the whole test setup. This may lie in the fact, that during the temperature increase the components thermal expand, and therefore the cross-sections become larger. The resistance is inversely proportional to the cross-section and therefore the noticeable difference.

Relay		
Supplier A		
Before test	After test	Diff.
mΩ	mΩ	mΩ
0.4775	0.5347	0.0572
Relay with 40mm² Busbar		
Before test	After test	Diff.
mΩ	mΩ	mΩ
0.845	0.9655	0.1205

Table 10: Transition resistances of measured relay *[29]*

4 Thermal Model Generation

Progress in automotive technologies and especially in the EV sector has been remarkable in the last decade. Computer simulations and 3D modelling software optimally expand the alternatives available for experimental technologies and thereby reveal different critical problems (e.g. such as critical temperatures) already at the design stage. This reduces the cost of production, but on the other hand, the electrical components are pushed to their limits. Designers continually make them even more compact to save weight and space of the final BDU. Thus, thermal modelling is getting significant importance. Knowing the thermal efficiency of the BDU components can help to avoid switching problems and sink the probability of occurring accidents because of component failure.

4.1 Basic of Heat Transfer

A general definition of heat transfer would be: *Heat Transfer is thermal energy in transit due to a spatial temperature difference.* Whenever there exists a temperature difference in a medium or between media, heat transfer must occur (see *Figure 34*). If there is a temperature difference in solid or fluid, then heat transfer in that medium is defined as *conduction.* In contrast, the term *convection* is used for heat transfer that occurs between a surface and a moving fluid when they are at different temperatures. Last but not least mode of heat transfer is defined as *radiation.* Radiation is nothing else then electromagnetic wave energy emitted from all surfaces with a temperature greater than 0 K. [30, p. 2]
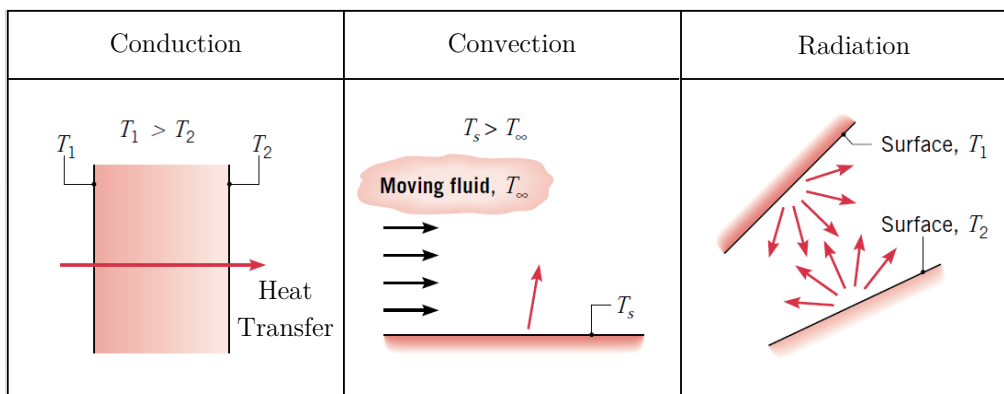
Figure 34: Different heat transfer modes (conduction, convection, and radiation) *[30]*

4.1.1. Conduction

Conduction may be defined as the transfer heat from the higher energy state (e.g. hotter medium, T_1) to state with less energy (e.g. cooler medium, T_2) due to interactions between particles (see ***Figure 35***). In conduction, heat is spread by the mechanism of direct contact of the elementary particles of the body, such as molecules, atoms, or free electrons. In parts of a medium with higher temperatures, the elemental particles move faster and in collision with nearby, slower particles, they slow down losing their energy. At the same time, there is a mechanism of heat propagation by the motion of free electrons. Depending on the properties of the medium the heat is conducted in two ways: (i) through collisions of atoms and molecules, which is the case with *electrical insulators*, (ii) through electron motion if the medium is an *electrical conductor.* An everyday example of spreading heat through conduction would be a spoon dipped in hot coffee: the free end of the spoon has almost the same temperature as that part immersed in coffee. [31, p. 91]
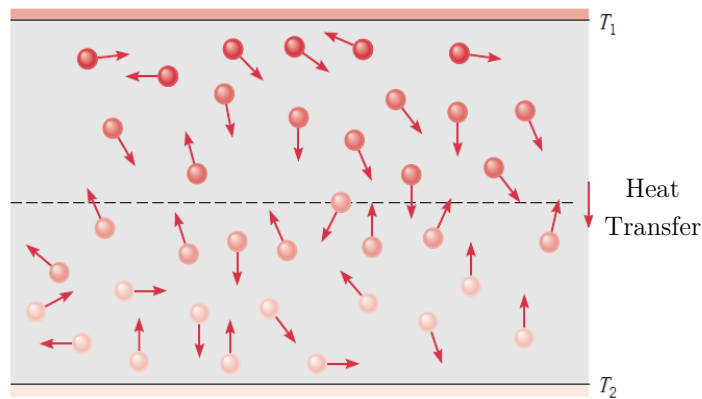
Figure 35: Conduction heat transfer at the molecular level *[30]*

Fourier[12] set up an experimental law for the stationary propagation of heat by conduction: conduction heat transfer through a plane wall is directly proportional to the temperature difference ΔT, to the wall surface A and time t, and inversely proportional to the wall thickness L (see ***Figure 36***). The proportionality coefficient in Equation (15) is thermal conductivity k, which is a physical property of a medium and it is experimentally determined.

$$Q = -k \frac{T_2 - T_1}{L} A \cdot t \tag{15}$$

---

[12] *Jean-Baptiste Joseph Fourier* (21 March 1768 – 16 May 1830) was a French mathematician and physicist born in Auxerre and best known for initiating the investigation of Fourier series and their applications to problems of heat transfer and vibrations.

■**ife**
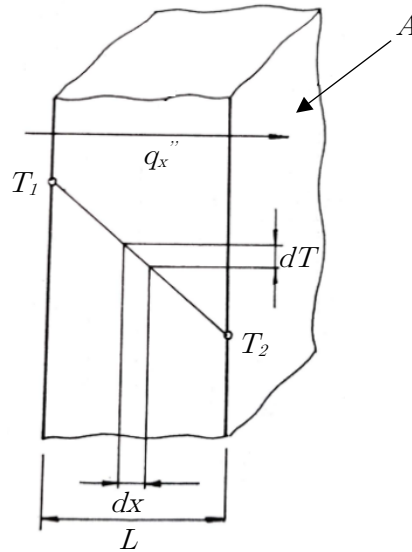
Figure 36: Conduction heat transfer through a plane wall *[31]*

Calculating per unit area ($A = 1$ m^2) and per unit time ($t = 1$ s) for the one-dimensional plane wall (see **_Figure 36_**), the Equation (15) is expressed as:

$$q''_x = -k\frac{dT}{dx} \tag{16}$$

The heat flux q''_x is the heat transfer rate in *x*-direction per unit area *perpendicular* to the direction of heat transfer, and it is proportional to the temperature gradient $\frac{dT}{dx}$ in this direction. The minus sign is a consequence of the fact that heat is transferred in the direction of decreasing temperature which means that the temperature gradient $\frac{dT}{dx}$ is negative in the direction of heat transfer. [30, p. 4] [31, p. 93]

Under the steady-state conditions, where the temperature distribution is linear (see **_Figure 36_**), the temperature gradient $\frac{dT}{dx}$ can be expressed as:

$$\frac{dT}{dx} = \frac{T_2 - T_1}{L} \tag{17}$$

and the heat flux q''_x is then:

$$q''_x = -\frac{T_2 - T_1}{\frac{L}{k}} = -\frac{\mathit{\Delta}T}{R_{th}} \tag{18}$$

which is like the Ohm's Law (see Equation (1)). In analogy to this law, the term R_{th} in Equation (18) is referred to as thermal resistance. [31, p. 93]

4.1.2. Convection

The basic law of heat transfer was experimentally investigated and mathematically formulated by Newton[13]. According to that law, if the surface A is in contact with some gas or liquid (see **_Figure 37_**), the heat exchanged by _convection_ is:

$$Q = h \ (T_s - T_\infty)A \cdot t \tag{19}$$

Like conduction for the unit area and unit time the heat transferred via _convection_:

$$q''_{conv} = h \ (T_s - T_\infty) \tag{20}$$

the _convective_ heat flux q''_{conv} is proportional to the difference between the surface temperature T_S and fluid temperature T_∞. the q''_{conv} is presumed to be positive if heat is transferred from the surface is $T_S > T_\infty$ and negative if heat is transferred to the surface $T_\infty > T_S$. [31, p. 100] [30, p. 8]
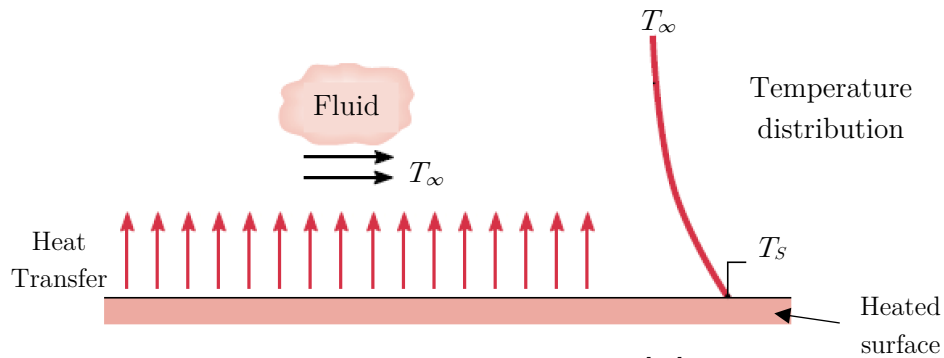
Figure 37: Convection heat transfer _[30]_

The parameter h is defined as the _convection heat transfer coefficient_. It depends on conditions in the boundary layer, which are influenced by surface geometry, the nature of the fluid motion, and an assortment of fluid thermodynamic and transport properties. Analysing the Equation (20) it is easily noticeable that the heat transfer via convection reduces to a study of how the convection heat coefficient h can be determined. Although h is experimentally determined and usually depends on more than one factor, in the solution of problems to come will be presumed h to be constant. Some typical values for h are given in **Table 11** below. [30, pp. 8-9]

---

[13] Sir Isaac Newton (25 December 1642 – 20 March 1726/27) was an English mathematician, physicist, astronomer, and theologian recognised as one of the most influential scientists of all time and as a key figure in the scientific revolution.

∎ife

Process	h W/m²K
Free Convection	
Gases	2 - 25
Liquids	50 - 1000
Forced Convection	
Gases	25 - 250
Liquids	100 - 20000
Convection with phase change	
Boilng or condensation	2500 - 100000

Table 11: Heat transfer coefficient typical values

4.1.3. Radiation

Unlike the propagation of heat by conduction and convection, *radiation* of heat is not related to the matter. Electromagnetic waves propagate from the radiating medium and transmit it to another medium receiving the radiation, although there may be a vacuum between the two. An example of such a way of heat transfer is the Sun's radiation into the environment, and partly to the Earth. [31, p. 118]

Radiation that is emitted by the surface originates from the thermal energy of matter bounded by the surface. The rate at which energy is released per unit area is termed the as Stefan–Boltzmann[14,15] law for ideal *radiator* or *blackbody*:

$$E_b = \sigma \, T_S^4 \tag{21}$$

Important to note is that the absolute temperature of the surface T_S must be expressed in Kelvin (K). Nevertheless, the heat emitted by a real surface is always less than that of a blackbody at the same temperature:

$$E \ = \varepsilon \, \sigma \, T_S^4 \tag{22}$$

---

[14] Josef Stefan (24 March 1835 – 7 January 1893) was an ethnic Carinthian Slovene physicist, mathematician, and poet of the Austrian Empire.

[15] Ludwig Eduard Boltzmann (February 20, 1844 – September 5, 1906) was an Austrian physicist and philosopher.

■ife

The factor ε in Equation (22) is radiative property of the surface termed as *emissivity* ranging from 0 to 1. It depends strongly on the surface material and provides a measure of how efficiently a surface emits energy relative to a blackbody. [30, p. 10]
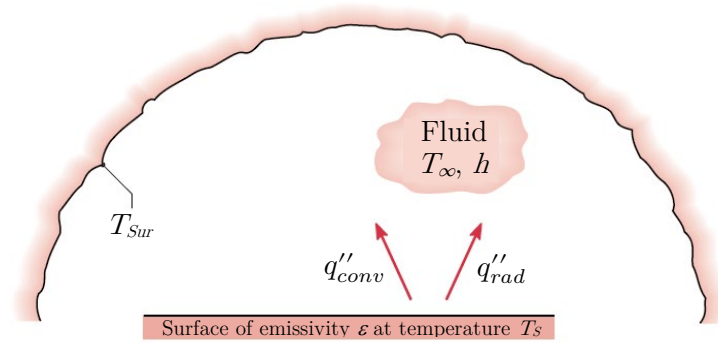
Figure 38: Radiation heat exchange *[30]*

Usually, radiation heat exchange happens between a small surface at T_S and a much larger, isothermal surface that surrounds the smaller one (see ***Figure 38***). The surroundings could be the walls of a room whose temperature T_{Sur} differs from that of an enclosed surface. If the surface has an emissivity of ε, the heat flux from the surface per unit area is defined as:

$$q''_{rad} = \varepsilon \, \sigma \, [T_S^4 - T_{Sur}^4] \tag{23}$$

Looking closely at ***Figure 38*** it can be noticed that the surface may simultaneously transfer heat by convection and radiation. This is usually the case in many applications because there is adjoining gas responsible for the convection. The total heat transfer from a surface can be calculated as follows:

$$q = q_{conv} + q_{rad} = hA(T_S - T_\infty) + \varepsilon A \sigma (T_S^4 - T_{Sur}^4) \tag{24}$$

Note that in the Equation (24) the convective q''_{conv} and radiative q''_{rad} heat flux are multiplied with the area A of the surface. The resulting quantity is termed as *heat rate q_{conv}* and q_{rad} respectively.

4.1.4. The Conservation of Energy

One of the most important laws of nature is that the total energy of a closed system (a region of fixed mass) must be conserved. Therefore, the only way that the amount of energy in a system can change is if the energy leaves the boundaries of the system. For a closed system, there are only two ways in which the energy can cross its boundaries: (i) *heat transfer through the boundaries* and (ii) *work done on the system or by the system.* [30, p. 13]
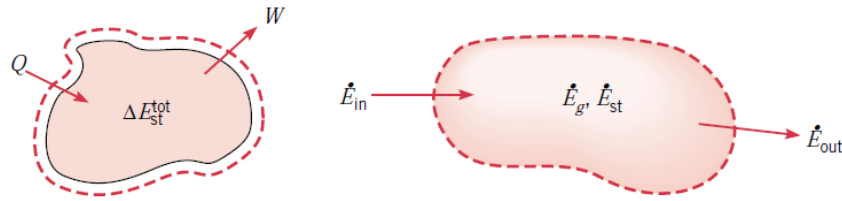
Figure 39: Conservation of energy in a closed system *[30]*

The increase in the amount of energy stored in a closed system must equal the amount of energy that enters the closed system minus the amount of energy that leaves the closed system. This statement is known as the First Law of Thermodynamics and can be described as:

$$\Delta E_{st}^{tot} = Q - W \tag{25}$$

The symbol Δ in Equation (25) represents the change in total energy stored in the system E_{st}^{tot}, which consists of *kinetic energy* (the motion of molecules and atoms), *potential energy* and *internal energy*. It will most often be the case in heat transfer problems that the changes in kinetic and potential energy are small and can be neglected. The Q is the net heat transferred to the system, and the W is the work done by the system (see ***Figure 39***). [30, p. 14]

In ***Figure 39*** there are few other energy terms which must be defined: E_{st} stands for the stored thermal and mechanical energy[16], E_g is the energy generation (e.g. the Joule heating caused by current flow), and the thermal and mechanical energy transport across the system, that is, the inflow and outflow energy E_{in} and E_{out}, respectively. The *dot* over the energy terms indicates the rate change, and so the statement in (25) becomes:

$$\dot{E_{st}} = \frac{dE_{st}}{dt} = \dot{E_{in}} - \dot{E_{out}} + \dot{E_g} \tag{26}$$

Equation (26) provides essential tools for solving heat transfer problems. Every application of the First Law Thermodynamics must begin with the identification of an appropriate control volume and its control surface. The next step is to identify the energy terms that are relevant to the problem. The last step is to decide whether to perform the steady-state analysis, where the control volume is in the thermal equilibrium or to solve it as time-dependent using Equation (26). This choice depends on the objective of the solution and in this work the time-dependent approach is the preferred one. [30, p. 15]

---

[16] Mechanical energy is defined as the sum of the kinetic and potential energy.

■ife

4.1.5. General Case of Heat Transfer

The heat transfer occurs if there is a temperature difference or temperature gradient. The process of heat exchange will last until all points of the body have the same temperature (complete *thermal equilibrium*). Points of a body with the same temperature can relate to a line termed as *isotherm* (see **Figure 40**). There are an infinite number of isotherms on a body that cannot intersect, meaning one point cannot have two temperatures. The temperature gradient is always perpendicular to the isotherm line. This implies that there is no heat exchange between points on the same isotherm. Recognizing that heat flux is a vector quantity, a more general statement of conduction can be written as:

$$q_n'' = -k\frac{\partial T}{\partial n}\boldsymbol{n} \tag{27}$$

where q_n'' is the heat flux in a direction $\boldsymbol{n}$, which must be normal to the isotherm line as shown in **Figure 40**.
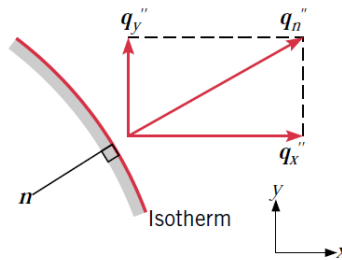
Figure 40: Heat flux vector in the two-dimensional coordinate system *[30]*

Since the heat flux is a vector quantity it can be resolved into components represented in Cartesian coordinates. The general expression for the heat flux is:

$$q'' = -k\boldsymbol{\nabla} T = -k\left(\underbrace{\boldsymbol{i}\frac{\partial T}{\partial x}}_{q_x''} + \underbrace{\boldsymbol{j}\frac{\partial T}{\partial y}}_{q_y''} + \underbrace{\boldsymbol{k}\frac{\partial T}{\partial z}}_{q_z''}\right) \tag{28}$$

The $\boldsymbol{\nabla}$ is the three-dimensional delta operator and $T(x,y,z)$ is the scalar temperature field. The medium in which the conduction is occurring is *isotropic*. For such medium thermal conductivity k is independent of the coordinate system. To determine the scalar temperature field $T(x,y,z)$ is the goal of heat transfer analysis. The temperature distribution in a closed system is resulting from the conditions imposed on its boundaries. The approach to determine how the temperature varies with the position is the same as described in the section above, applying the energy conservation equation on a differential control volume (see **Figure 41**). Solving the resulting heat differential equation, with appropriate boundary conditions, gives the temperature distribution $T(x,y,z)$. [30, p. 70]
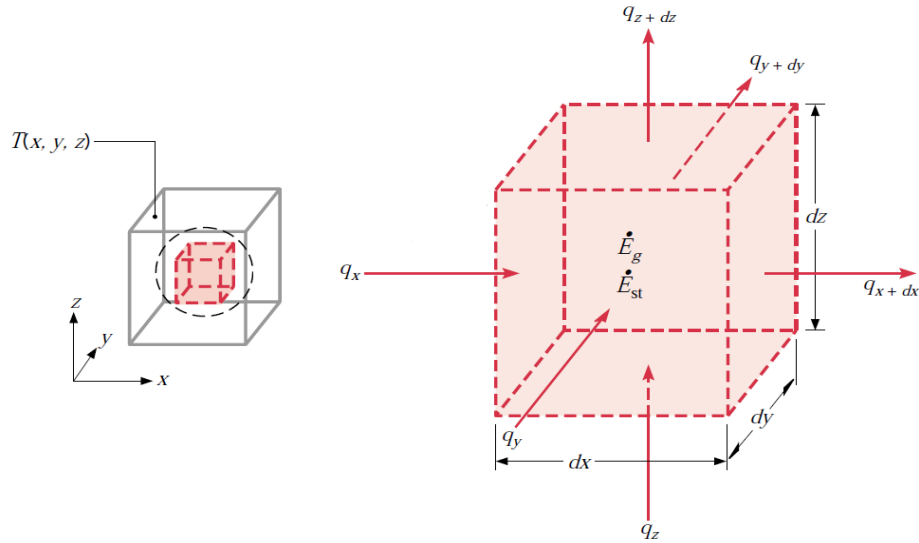
Figure 41: Differential control volume $V(dx, dy, dz)$ *[30]*

Looking at **Figure 41** and if only the heat transfer in the *x-direction* is considered, the conduction heat rate q_x at the opposite sites can be expressed as a Taylor[17] series expansion (the higher-order terms are neglected):

$$q_{x+dx} = q_x + \frac{\partial q_x}{\partial x} dx \tag{29}$$

In the control volume in **Figure 41**, there is an energy source (e.g. heat generated caused by current flow) with heat generation rate $\dot{q}$ per unit volume:

$$\dot{E}_g = \dot{q} \; dx \; dy \; dz \tag{30}$$

and since the control volume has a specific heat capacitance c_P the energy being stored may be expressed as:

$$\dot{E}_{st} = \rho c_P \frac{\partial T}{\partial t} dx \; dy \; dz \tag{31}$$

Important to notice in Equation (31) is the term $\rho c_P \frac{\partial T}{\partial t}$, which represents the *time* rate of change of thermal energy. That is exactly the part where the time dependency of the heat transfer problem is hidden. For the time-dependent heat transfer problems, the temperature distribution is a function of time t and the coordinates of the preferred coordinate system. It is easily concluded that the heat transfer problems (if not restricted to simple geometries) do not always have analytical solutions and that simplifications of the problem must be considered.

---

[17] Brook Taylor (18 August 1685 – 29 December 1731) was an English mathematician who is best known for Taylor's theorem and the Taylor series.

 With all of the energy forms defined they can be substituted into the Equation (26):

$$\underbrace{\rho c_P \frac{\partial T}{\partial t} dx\ dy\ dz}_{\dot{E}_{st}} = \underbrace{q_x + q_y + q_z}_{\dot{E}_{in}} - \underbrace{q_{x+dx} + q_{y+dy} + q_{z+dz}}_{\dot{E}_{out}} + \underbrace{\dot{q}\ dx\ dy\ dz}_{\dot{E}_g} \qquad (32)$$

Substituting from Equation (29) for all coordinates:

$$\rho c_P \frac{\partial T}{\partial t} dx\ dy\ dz = -\frac{\partial q_x}{\partial x} dx - \frac{\partial q_y}{\partial y} dy - \frac{\partial q_z}{\partial z} dz + \dot{q}\ dx\ dy\ dz \qquad (33)$$

The conduction heat rates q [W] can be evaluated from the Equation (16), where the heat flux q'' [W/m^2] components must be multiplied by differential area [m^2] to obtain the transfer rate q [W] (here represented only for *x-coordinate*):

$$q_x = -k\ \underbrace{dydz}_{dA}\ \frac{\partial T}{\partial x} \qquad (34)$$

Substituting everything into the Equation (33) and dividing with the control volume ($dxdydz$) the *general heat diffusion equation* is obtained:

$$\rho c_P \frac{\partial T}{\partial t} = k \left[\frac{\partial}{\partial x}\left(\frac{\partial T}{\partial x}\right) + \frac{\partial}{\partial y}\left(\frac{\partial T}{\partial y}\right) + \frac{\partial}{\partial z}\left(\frac{\partial T}{\partial z}\right) \right] + \dot{q} \qquad (35)$$

The thermal conductivity k is *constant* for the simplicity of further work. The heat diffusion equation is the basis for the heat transfer analysis. Nevertheless, it looks complicated, but it describes the basic condition, that is, conservation of energy. [30, p. 72]

■ife

4.1 Numerical Methods used for Thermal Analysis

As stated, before the Equation (35) represents the basis for any thermal analysis and solving it, by applying the boundary and initial conditions, gives the temperature distribution as a function of time $T(x(t), y(t), z(t))$. This, rather, the complicated mathematical endeavour is simplified by introducing the numerical approach using *Finite Difference Method* (FDM) and *Finite Element Method* (FEM) (please refer to **Chapter 1.2** for comparison between these two methods).

There are many heat transfer simulation software existing today, which give an intuitive approach to solving heat transfer problems. The user is supposed to draw or import model geometry into the program and apply the boundary and initial conditions. After starting the simulation, the software's algorithm generates the meshes and solves the Equation (35) at each node depending on the density of the mesh, which can also be user selected.

The focus of this work is not to recreate the existing thermal simulation software's, but to solve the heat problem using current I as model input. The goal is to obtain the maximal temperature of the different BDU components as a function of time by solving a *simplified* time-dependent heat transfer problem, where the heat transfer coefficients for thermal conduction k, convection h and properties of materials (ρ, c_P, ε) are constant.

4.1.1. Limitations of Analytical Methods

Various heat conduction problems can be solved systematically by deriving the governing differential Equation (35) by performing the energy balance on a differential volume of elements. To solve the equation proper boundary and initial conditions must be set. [32]

$$\frac{1}{r^2}\frac{d}{dr}\left(r^2\frac{dT}{dr}\right) + \frac{\dot{e}}{k} = 0$$

Sphere   0 r_o r

$$\frac{dT(0)}{dr} = 0$$

$$T(r_o) = T_1$$

Analytical solution:

$$T(r) = T_1 + \frac{\dot{q}}{6k}(r_0^2 - r^2)$$
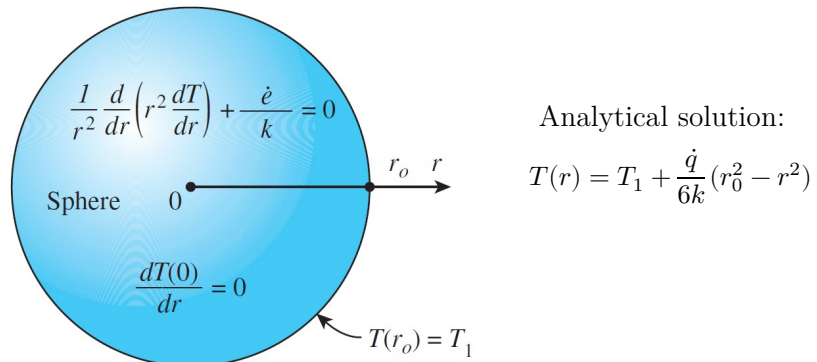
Figure 42: Analytical solution for heat transfer problem in a sphere. The analytical solution requires the governing differential equation (written inside the sphere). Analytical solutions are often limited to simple geometries. [32]

■ife

Even though the analytical solutions give the exact results to the specified heat problem, they are often limited to simplified geometries (see ***Figure 42***), where the entire geometry can be described mathematically in an appropriate coordinate system. Even in simple geometries, heat transfer problems cannot be solved analytically if the thermal conditions are not sufficiently simple or can be simplified with reasonable approximations. On the other hand, while attempting to derive an analytical solution to a physical problem, there is always a tendency to oversimplify the problem by transforming it into sufficiently simple geometries, which can be described mathematically. Therefore, it is common practice to ignore any effects that cause mathematical complications such as nonlinearities in the differential equation or the boundary conditions (see ***Figure 43***). [32]

An oval-shaped body

Simplified model

Realistic model

Sphere

An analytical solution can be easily found, but the physical model is oversimplified and the solution is far from correct.

Numerical (approximate) solution, but an accurate solution of actual problem.
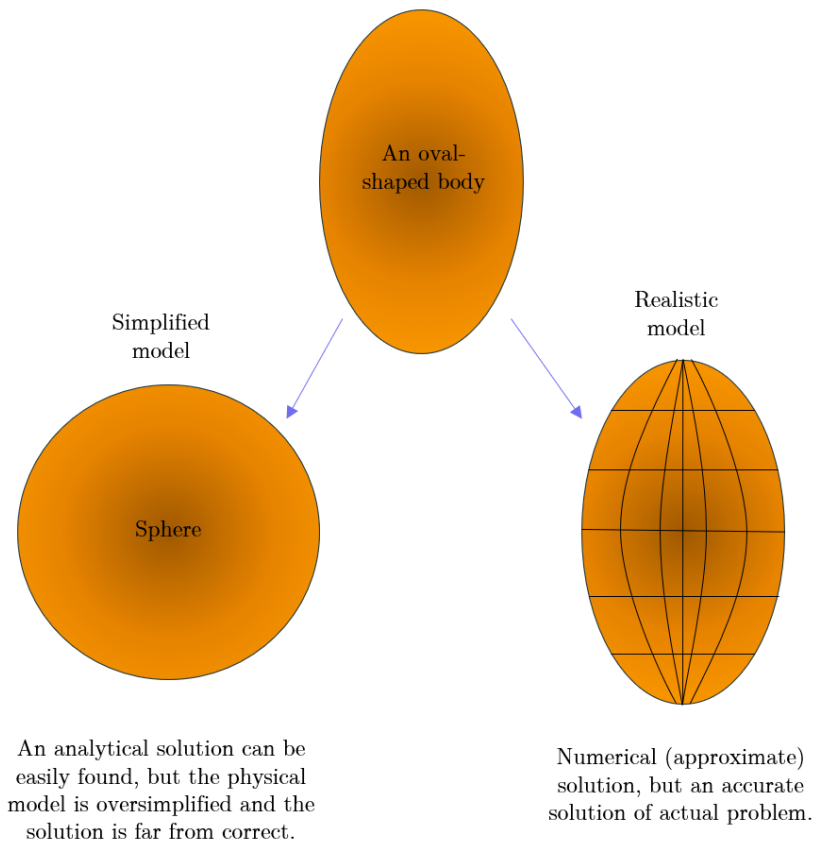
Figure 43: Numerical solution of the real-world problem may be just an approximation but also more accurate than the analytical one based on oversimplification. [32]

A mathematical model intended for a numerical solution is likely to represent the actual problem better. This is an iterative process that is extremely tedious and time-consuming if done by hand. Thus, the numerical methods are ideal for computers, which are ideally suited for calculations. Once the numerical equations are set up and coded into a computer program, a wide range of related problems can be solved just by changing the variables or parts of the algorithm. [32]

4.1.2. Finite Difference Formulation for Heat Conduction Problems

The numerical methods for solving differential equations are based on replacing the differential equations by algebraic approximations. In the case of the FDM this is done by replacing the derivatives by finite differences (see ***Figure 44***):

$$\frac{df(x)}{dx} = \lim_{\Delta x \to 0} \frac{\Delta f}{\Delta x} = \lim_{\Delta x \to 0} \frac{f(x + \Delta x) - f(x)}{\Delta x}$$

$$\frac{df(x)}{dx} \cong \frac{f(x + \Delta x) - f(x)}{\Delta x}$$

Which is the finite difference form of the first derivative. Performing a *Tylor series expansion* of the function $f(x)$ around the point x:

$$f(x + \Delta x) = f(x) + \Delta x \frac{df(x)}{dx} + \frac{1}{2} \Delta x^2 \frac{d^2 f(x)}{dx^2} + \ldots$$

It is easily noticeable that the smaller Δx, the smaller the error and, thus more accurate the approximation.
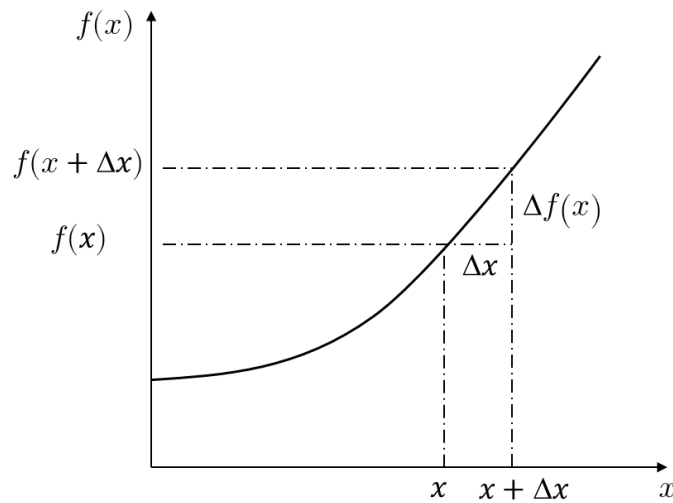
Figure 44: Derivative of a function approximated by finite difference

Considering steady-state[18] 1D heat conduction in a plane wall (see ***Figure 45***) of thickness L divided into internal nodes m with heat generation $\dot{q}$, the finite difference representation of the second derivative can be written for any node as:

$$\frac{dT_{m-\frac{1}{2}}}{dx} \cong \frac{T_m - T_{m-1}}{\Delta x} \quad and \quad \frac{dT_{m+\frac{1}{2}}}{dx} \cong \frac{T_{m+1} - T_m}{\Delta x} \tag{36}$$

---

[18] The system is in thermal equilibrium and there is no change in temperature $\frac{dT}{dt} = 0$.

$$\frac{d^2T_m}{dx^2} \cong \frac{\frac{dT_{m+\frac{1}{2}}}{dx} - \frac{dT_{m-\frac{1}{2}}}{dx}}{\Delta x} = \frac{\frac{T_{m+1} - T_m}{\Delta x} - \frac{T_m - T_{m-1}}{\Delta x}}{\Delta x} = \frac{T_{m-1} - 2T_m + T_{m+1}}{\Delta x^2} \quad (37)$$

Where the Equation (37) is the finite representation of the second derivative at a general internal node m. Equivalent, the finite difference formulation for steady 1D heat conduction in the region with heat generation and constant thermal properties is:

$$\frac{T_{m-1} - 2T_m + T_{m+1}}{\Delta x^2} + \frac{\dot{q_m}}{k} = 0 \quad (38)$$
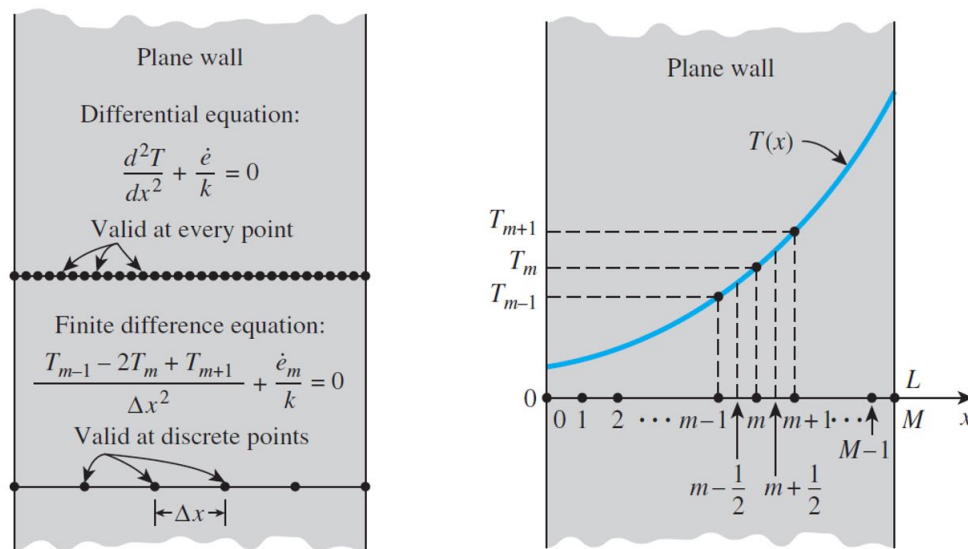
Figure 45: (a) The differential equation is valid at any point of a medium, whereas the finite difference equation is valid only at a discrete point (nodes m).
(b) Schematic of the nodes used in the development of FDM of heat transfer the wall. [32]

As noted above, the FDM for steady heat conduction is based on *subdividing* the medium into enough *volume* elements (see **Figure 46**) and then applying energy balance on each element. This is done by first selecting the nodal points at which the temperatures are to be determined and then forming control volumes over the nodes by drawing lines through the midpoints between the nodes. This way, the interior nodes remain in the middle of the elements, and the properties at the node such as the temperature and the rate of heat generation represent the average properties of the element. [32]
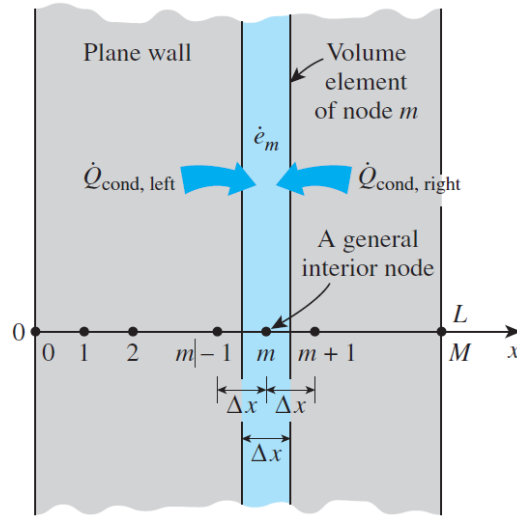
Figure 46: The nodal points and volume elements for the FDM [32]

Looking at **_Figure 46_**, the plane wall is subdivided into M equal regions of thickness $\Delta x = \frac{L}{M}$ with constant properties. The coordinate of any node m is simply $x_m = m\Delta x$ with corresponding temperature at this point $T(x_m) = T_m$, which will be extensively used for the different positions of used thermocouples. It is important to notice that all interior nodes ($m = 1, \dots, M-1$) are full-size elements of thickness Δx, whereas the two elements ($m = 0$ and $m = M$) at the boundaries are half-sized with the thickness $\frac{\Delta x}{2}$. Assuming the heat conduction to be into the elements on all surfaces, the energy balance equation[19] is: [32]

$$
\begin{bmatrix} \text{Rate of heat} \\ \text{conduction at} \\ \text{left surface} \end{bmatrix} + \begin{bmatrix} \text{Rate of heat} \\ \text{conduction at} \\ \text{right surface} \end{bmatrix} + \begin{bmatrix} \text{Rate of heat} \\ \text{generation} \\ \text{inside element} \end{bmatrix} = \begin{bmatrix} \text{Rate of change} \\ \text{of the energy} \\ \text{contect of the} \\ \text{element} \end{bmatrix} \quad (39)
$$

$$
\dot{Q}_{cond,left} + \dot{Q}_{cond,right} + \dot{E}_g = \frac{\Delta E_{st}}{\Delta t} = 0 \quad (40)
$$

The stored energy within each element $\dot{E_{st}}$ does not change under steady-state conditions and thus $\frac{\Delta E_{st}}{\Delta t} = 0$. The rate of energy generation $\dot{E}_g$ is:

$$
\dot{E}_g = \dot{q}_m V_{Element} = \dot{q}_m A \ dx \quad (41)
$$

The $\dot{q}_m$ is the heat generation per unit volume [W/m³] and it is treated as a constant for the entire element. Under steady-state conditions the rate of heat conduction can be expressed as:

---

[19] Where the "*dot*" above the letters denotes the change in rate of energy, where the unit for all the values is Watt [W].

$$\dot{Q}_{cond,left} = kA\frac{T_{m-1} - T_m}{\Delta x} \ \text{ and } \ \dot{Q}_{cond,right} = kA\frac{T_{m+1} - T_m}{\Delta x} \qquad (42)$$

The direction of heat transfer is on both surfaces A is assumed to be toward the node m. Substituting the Equations (41) and (42) into Equation (40):

$$kA\frac{T_{m-1} - T_m}{\Delta x} + kA\frac{T_{m+1} - T_m}{\Delta x} + \dot{q}_m A \ dx = 0, \qquad \text{where } m = 1, 2, \dots, M - 1 \qquad (43)$$

which is identical to the difference Equation (38). The Equation (43) applies to each of $M - 1$ nodes, where the additional two equations needed to solve the $m = 0$ and $m = M + 1$ nodal temperatures are obtained by applying the appropriate boundary conditions: [32]

    i.   Specified Heat Flux q_0'' Boundary Condition

$$q_0'' A + kA\frac{T_1 - T_0}{\Delta x} + \dot{q}_0 A \ \frac{dx}{2} = 0 \qquad (44)$$

    ii.   Convection Boundary Condition

$$hA \left[T_\infty - T_0 \right] + kA\frac{T_1 - T_0}{\Delta x} + \dot{q}_0 A \ \frac{dx}{2} = 0 \qquad (45)$$

    iii.   Radiation Boundary Condition

$$\varepsilon\sigma A \left[T_{Sur}^4 - T_0^4 \right] + kA\frac{T_1 - T_0}{\Delta x} + \dot{q}_0 A \ \frac{dx}{2} = 0 \qquad (46)$$

    iv.   Combination of the same

$$q_0'' A + \ hA \left[T_\infty - T_0 \right] + \varepsilon\sigma A \left[T_{Sur}^4 - T_0^4 \right] + kA\frac{T_1 - T_0}{\Delta x} + \dot{q}_0 A \ \frac{dx}{2} = 0 \qquad (47)$$

The FDM results in a system of N algebraic equations where the N unknown nodal temperatures represent a system of equations which is solved simultaneously. If the system is small (e.g. $N = 3$) the elimination method may be the best choice. For larger systems, another approach is needed and, in this work, the direct method for solving a system of algebraic equations is used. The method is based on a fixed number of defined steps that result in the solution systematically. [32, p. 318]

The solution to Equation (43) is valid for any time point in time because under steady-state conditions the temperature does not change with time $\frac{dT(t)}{dt} = 0$. For transient heat problems, however, the temperature changes with time as with position, and thus the FDM formulation also requires discretization in time. As shown in **Figure 47** the space in the *x-direction* is discretised by finite steps of length Δx and by choosing a time step Δt the time axis is also discretised. The nodal temperatures are solved for every point m and for every time step i. The *superscript "i"* is used as the index for time steps, with $i = 0$ corresponding to initial condition. Thus, the computation time of transient conduction problems is $\frac{t}{\Delta t}$ times that of a steady state conduction problem. [32, p. 334]
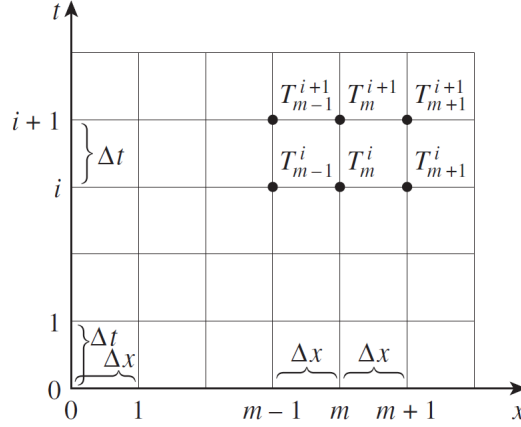
Figure 47: FDM formulation of transient heat conduction problems requires discretization in time in addition to discretization in space, where T_m^i is used to represent the temperature at the node m at time step i. [32, p. 334]

The volume elements in transient conduction problems are chosen is the same fashion as they are in steady-state conduction. The energy balance on a volume element during time step Δt can, therefore, be expressed as:

$$\begin{bmatrix} \text{Heat transfered into} \\ \text{the volume element} \\ \text{form all of its surfaces} \\ \text{in time step } \Delta t \end{bmatrix} + \begin{bmatrix} \text{Heat generated} \\ \text{within the} \\ \text{volume element} \\ \text{in time step } \Delta t \end{bmatrix} = \begin{bmatrix} \text{Change in the} \\ \text{energy content of} \\ \text{the volume element} \\ \text{in time step } \Delta t \end{bmatrix} \tag{48}$$

$$\Delta t \sum_{All\ sides} \dot{Q} + \Delta t \dot{E}_g = \Delta E_{element} \tag{49}$$

The Equation (49) differs from the steady-state formulation in that way, that is the change in energy content changes with time:

$$\Delta E_{element} = \rho c_p V_{element} \frac{\Delta T}{\Delta t} \tag{50}$$

For any node m and its volume element at any time step i the transient conduction energy balance can be expressed as:

$$\sum_{All\ sides} \dot{Q} + \dot{q}_m^i V_{Element} = \rho c_p V_{element} \frac{T_m^{i+1} - T_m^i}{\Delta t} \tag{51}$$

where the T_m^i and T_m^{i+1} are the temperatures of node m at times $t_i = i\Delta t$ and $t_{i+1} = (i+1)\Delta t$ respectively. The rate of heat transfer $\dot{Q}$ consists of conduction terms for interior nodes, but may involve convection, radiation, and heat flux for boundary nodes. [32, p. 335]

4.2 Thermal Model Generation for Shunt Resistor

As pointed out in ***Chapter 3.1***, four different shunts were used, which were connected to different cross-sections of the busbars. In the following text, a thermal model for the shunt$_A$ in combination with 40 mm^2 busbars will be presented (see ***Figure 48***). It is understood that the method is analogous to other tested shunts and any other combination of busbars.
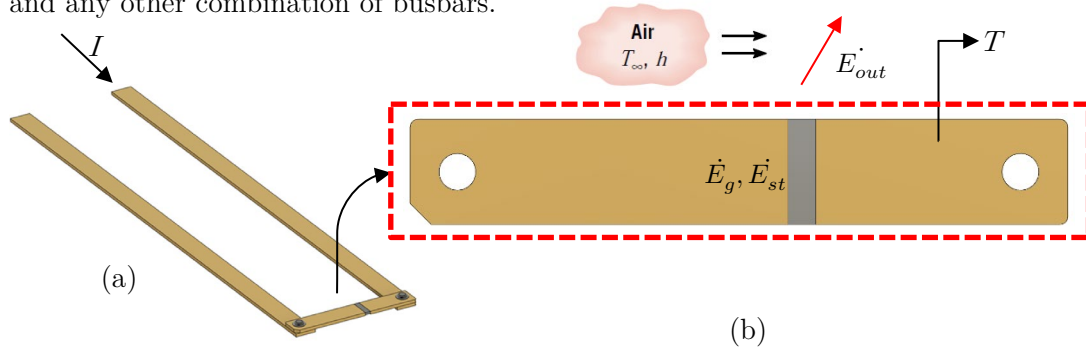
Figure 48: (a) Shunt$_A$ with connected 40 mm^2 busbars and

(b) Shunt$_A$ in larger view for easier understanding of thermal model development

The model from ***Figure 48 (a)*** was initially in thermal equilibrium with the ambient air and its surroundings. This equilibrium is disturbed when an electrical current I is passed through the busbars and the shunt$_A$. A developed thermal model should be able to compute the variation of the temperature T as a function of time t. To compare the calculated temperatures T with measured ones by the different thermocouples (see ***Chapter 3.1***) the thermal model should give the temperatures at the same places where the thermocouple is placed.

In this case, relevant terms include heat transfer by *convection* and *radiation* from the surface, energy generation due to *Joule heating* within the conductor, and a change in thermal energy storage. Due to different ohmic resistances of copper and manganin, the manganin part of the shunt will generate the most *Joule heat,* and therefore the conduction from the manganin to the copper parts of the shunt must be considered as well.

In ***Figure 49*** schematically, all the heat transfer mechanisms for shunt$_A$ and 40 mm^2 cross-section busbar have been displayed. The simulation has been done in *COMSOL Multiphysics*, which is a cross-platform finite element analysis solver and simulation software.
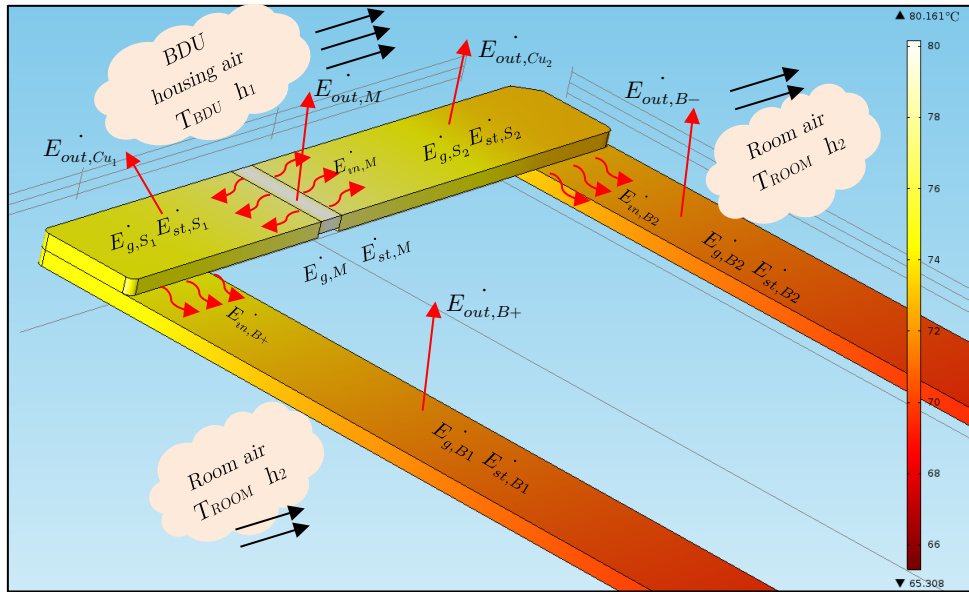
Figure 49: Heat transfer phenomena occurring on the shunt$_A$ and 40 mm^2 cross-section busbar as a consequence of current of $I = 300\ A$ after $t = 7000\ s$

This should give the reader a better perception of how the different components of the test setup get heated up while under current *I*. **Figure 49** serves as an example and is not the basis for any of the thermal models. Thus, in the further text, it will not be explained how to use the COMSOL Multiphysics Software, import geometries or how to place boundary conditions, etc. Furthermore, in **Figure 50** the position of the thermocouples, for which the temperature should be computed, is shown. It is understood that the same heat transfer phenomena occur for any other test setup combination.
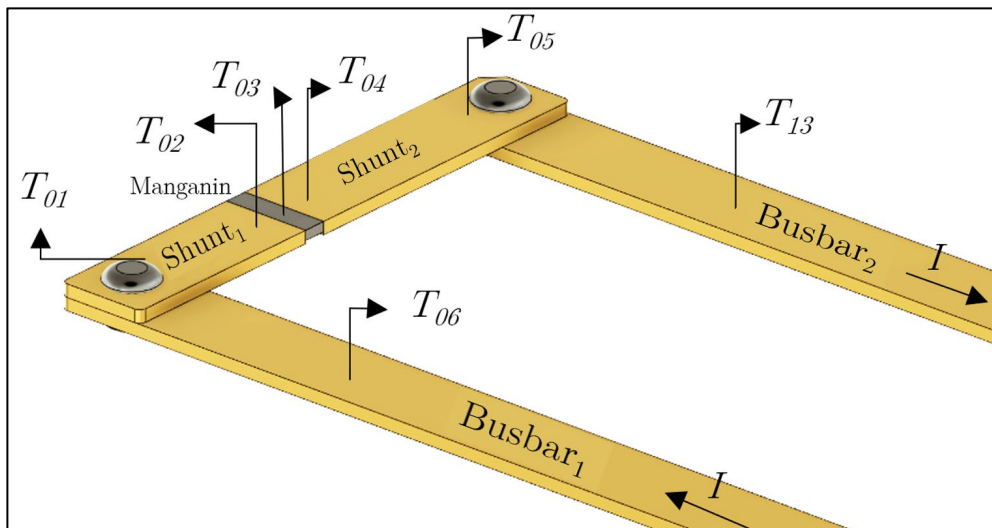
Figure 50: Allocation of thermocouples for which the temperature should be computed

To use the FDM introduced in *Chapter 4.1* the shunt and busbar setup from *Figure 50* was divided into the finite number of volume elements, where the transient heat conduction is considered only in *x-direction*. Thus, representing the real-world system as a 1D system involves some simplification. *Figure 51* to *Figure 55* should give the reader a sort of intuition on how the system was downscaled to 1D and prepared for FDM analysis.

For simplicity reasons, the geometry was further divided into 5 regions (see *Figure 51*) and, thus, the nodes and corresponding finite element volumes could be easily defined, and the energy balance equations could be applied.
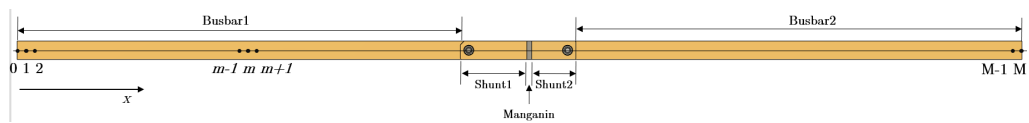
Figure 51: $Shunt_A$ and 40 mm^2 busbars in 1D representation suited for FDM analysis.

Important to notice is that the thermal equations for *convection*, *radiation*, *conduction*, and *energy generation* for each of the regions are given in **Appendix A: Thermal Model for Shunt** at the end of this document. The reason for doing this is the very long equations that are like each other with different subscripts indicating which element/region is described. In that way, only the governing energy balance equations are given with the occurring thermal phenomena. The interested reader is at this point referred to the end of this document.

I.   Boundary Equation where Busbar$_1$ connects to PSU-Cable

The physical connection to the PSU-Cable (see *Figure 22*) was selected as the starting point for the FDM analysis and its shown in *Figure 52*.
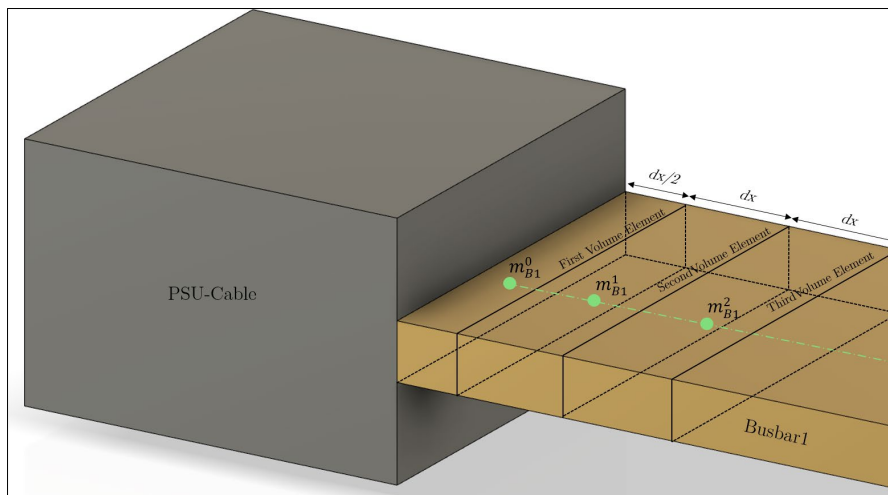
Figure 52: Schematic representation where busbar$_1$ connects to PSU-Cable

Even though the PSU-Cable connects to the Busbar$_1$ ($B1$), it is not a part of the thermal model. Its effect on the $B1$, being five times thicker, is addressed as negative Heat Flux from the $B1$ to the PSU-Cable. The first volume element m_{B1}^0, where the *superscript* is the nodal element and *subscript* the component, is defined as half of its volume because it connects to the PSU-Cable. Next elements m_{B1}^1, m_{B1}^2, … are defined as a whole. Thermal phenomena occurring at the m_{B1}^0 volume element are[20]: convection $\dot{E}_{Conv,B1-PSU}$ (85), radiation $\dot{E}_{Rad,B1-PSU}$ (86), conduction $\dot{E}_{Cond,B1-PSU}$ (87) and energy generation $\dot{E}_{Gen,B1-PSU}$ (88) due to electrical current I. Writing each of the energy terms in energy conservation equation, it follows:

$$\frac{dT}{dt} = \frac{1}{2}\dot{E}_{Conv,B1-PSU} + \frac{1}{2}\dot{E}_{Rad,B1-PSU} + \dot{E}_{Cond,B1-PSU} + \frac{1}{2}\dot{E}_{Gen,B1-PSU} \qquad (52)$$

where the "1/2" in front of the energy terms for convection, radiation, and energy generation indicate that only half of the element volume is considered. Important to notice is that (52) is only solved for the node m_{B1}^0 for every time step Δt but is fully coupled with the next volume element m_{B1}^1, which is then coupled with m_{B1}^2 and so on.

II.   Node Equation for Busbar$_1$

The same heat transfer phenomena occur at the general node m_{B1}^n for the B1 finite element. Thus, writing the energy conservation equation:

$$\frac{dT}{dt} = \dot{E}_{Conv,B1} + \dot{E}_{Rad,B1} + \dot{E}_{Cond,B1} + \dot{E}_{Gen,B1}, \text{where } m = n_{B1}^2,\ldots,n_{B1}^{End} \qquad (53)$$

The included energy terms in Equation (53) are, again, the energy term for convection $\dot{E}_{Conv,B1}$ (90), radiation $\dot{E}_{Rad,B1}$ (91), conduction $\dot{E}_{Cond,B1}$ (92) and energy generation $\dot{E}_{Gen,B1}$, (93). Because the first node n_{B1}^1 is part of the boundary Equation (52), the node equation for $B1$ started at second node n_{B1}^2.
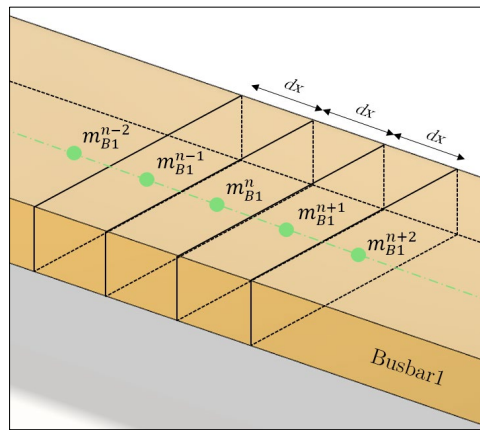
Figure 53: General node for busbar$_1$

---

[20] For Equations please refer to **Appendix A** to Equations (86), (87), (88), (89), (90) respectively.

III.   Node Equation for Shunt₁

The *B1* connects to shunt₁ (*S1*) (see ***Figure 23***) and the system expands for the *S1* thermal equations. Because both *B1* and *S1* are made of the same material, the system is further divided into finite elements without introducing new boundary equations. Nevertheless, an additional division would contribute to the accuracy of the results but as simulations have shown this division is negligible and the system becomes more complex and thus the computational time rises.

In this way, the screw connection between the *B1* and *S1* is also neglected (see ***Figure 54***). As from ***Figure 23*** and in real-world operations the *S1* is covered with BDU housing, the energy generated in the *S1* is spent on heating the housing itself. Thus, the BDU is indirectly included in the thermal model and the percentage of generated energy (see Equation (97)) in *S1* transferred to the housing was obtained through "try and error" method.
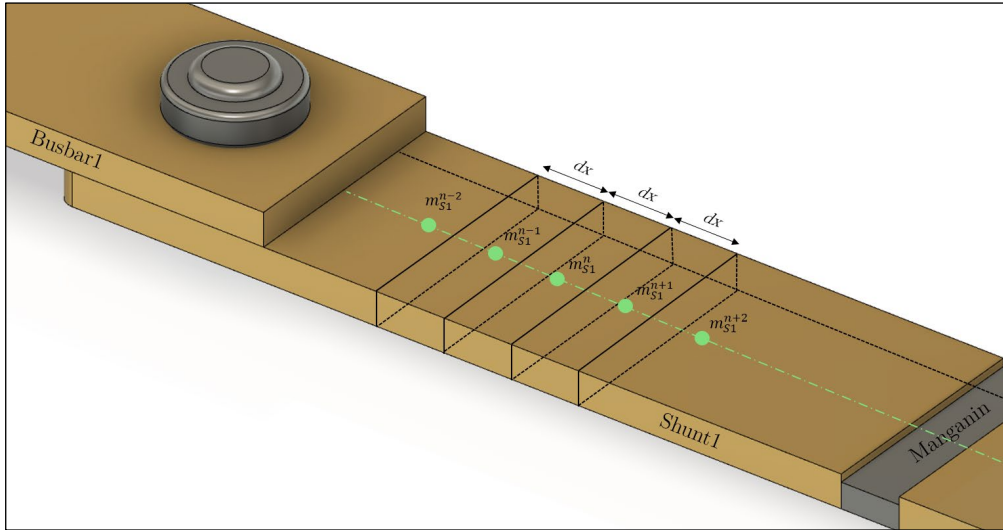
Figure 54: General node for shunt₁

Through the thermal simulation, it was found that 38% of the generated energy $\dot{E}_{Gen,B1}$ (97) in the *S1* is transferred to the BDU housing. Because the BDU housing has a rather small volume relative to *S1*, the convection is much reduced and therefore in energy equations neglected. The general node equation for *S1* can be written as:

$$\frac{dT}{dt} = \dot{E}_{Rad,S1} + \dot{E}_{Cond,S1} + \dot{E}_{Gen,S1}, \qquad \text{where } m = n_{S1}^2, \ldots, n_{S1}^{End} \qquad (54)$$

IV.   Boundary Equations where Shunt₁ connects to Manganin

Following the geometry, the *S1* connects to the manganin (*M*) and the boundary node equation at the contact place is built accordingly to **Figure 55**, where the first node of *M*, m_M^1 has its half volume in *S1* and the other half in *M*. The division was necessary because of the different materials from which *S1* and *M* were made off. In comparison to copper, manganin has high specific relative resistance (see **Table 4**) and because of its small dimensions, it generates the most heat energy and therefore it heats the most. Because of the enclosed environment, the convection is negligible, and radiation is a small part of heat loss. Therefore, the generated heat is transferred mostly via conduction to *S1* and *S2* on the other side:

$$\dot{E}_{Cond,S1-M} = \frac{4}{(\rho_{Cu}c_{p,Cu}a_S b_S + \rho_M c_{p,M} a_M b_M)} \left[a_S b_S k_{Cu} \frac{T_{n_{S1}^{End}} - T_{n_M^1}}{dx^2} \right.$$
$$\left. + a_M b_M k_M \frac{T_{n_M^2} - T_{n_M^1}}{dx^2} \right] \tag{55}$$
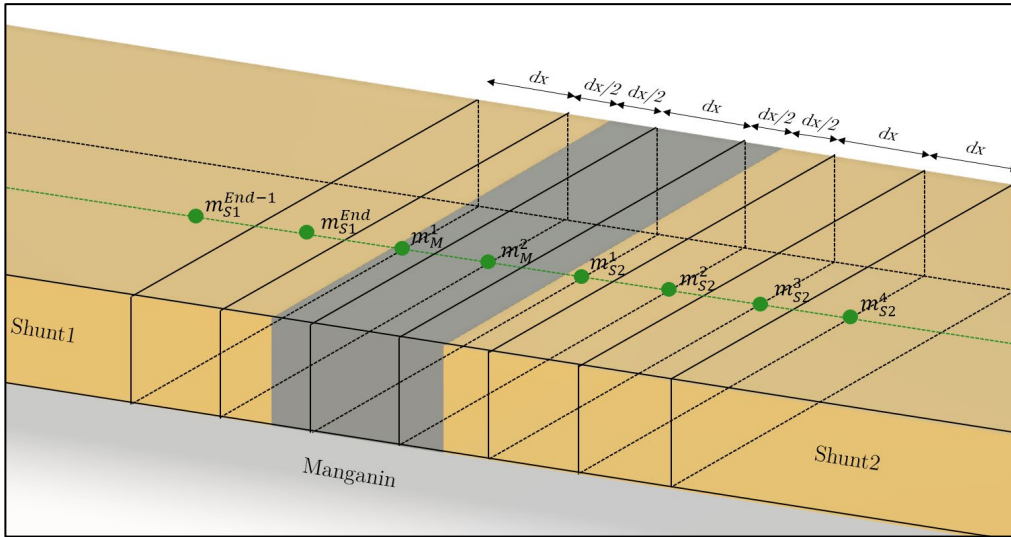
Figure 55: Boundary node equation and general node equation where S1/S2 connects to manganin

An analogy to *B1* and *S1*, the radiation $\dot{E}_{Rad,S1-M}$ (99), conduction $\dot{E}_{Cond,S1-M}$ (100) and the energy generation $\dot{E}_{Gen,S1-M}$ (101) are all part of the energy conservation equation:

$$\frac{dT}{dt} = \frac{1}{2}\dot{E}_{Rad,S1-M} + \dot{E}_{Cond,S1-M} + \frac{1}{2}\dot{E}_{Gen,S1-M} \tag{56}$$

where the "1/2" in front of energy terms represent the half of volume considered at the contact place. As for *S1*, 38% of the generated energy is transferred to the BDU housing.

V.   Node Equation for Manganin

As shown in previous **Figure 55**, due to the small dimension of M relative to other components, it was divided into two nodes for the FDM computation. Theoretically, it could be divided into an infinite number of nodes with $\Delta x \to dt$, but because the mesh in space Δx was taken as constant it would contribute to much higher system complexity and number of equations, which, on the other hand, extend the computational time. The thermal equations describing the M are equivalent to the previous, namely conduction $\dot{E}_{Cond,M}$ (104) and electricity generation $\dot{E}_{Gen,M}$ (105). The equations are combined in the following expression:

$$\frac{dT}{dt} = \dot{E}_{Rad,M} + \dot{E}_{Cond,M} + \dot{E}_{Cond,M} \tag{57}$$

VI.   Boundary Equation where Manganin connects Shunt$_2$

Looking at **Figure 23**, it is easy to conclude that the used test geometry is symmetrical, and based on that, the thermal FDM equations for $S2$ and $B2$ are analogous to the $S1$ and $B1$, respectively. Even the connections between M and $S2$ and $B2$ and PSU-Cable are formed the same way. The only difference is that the $S2$ is shorter than $S1$, but this does not represent any deviation from the basic principle. In this way, it is easy to set up the thermal equation for the connection point between M and $S2$:

$$\frac{dT}{dt} = \frac{1}{2}\dot{E}_{Rad,S2-M} + \dot{E}_{Cond,S2-M} + \frac{1}{2}\dot{E}_{Gen,S2-M} \tag{58}$$

As for the Equation (56), the Equation (58) is only solved at the one point, and in this case, it is m_{S2}^1, where the subscript represents the element and superscript is the node number.

VII.   Node Equation for Shunt$_2$

The general node m_{S2}^n for the $S2$ is analogous to the $S1$ general node with m_{S1}^n, with the difference that the $S2$ is shorter than $S1$. Thus, a lesser number of finite elements is used to thermally describe $S2$:

$$\frac{dT}{dt} = \dot{E}_{Rad,S2} + \dot{E}_{Cond,S2} + \dot{E}_{Gen,S2}, \qquad \text{where } m = n_{S2}^2, \ldots, n_{S2}^{End-1} \tag{59}$$

VIII.   Node Equation for Busbar$_2$

The $S2$ is connected to the Busbar$_2$ ($B2$) with the screw connection. Furthermore, the screw connection is left out of the simulation because its effects on thermal behavior are minimal and it would contribute to unnecessary complexity of the system. As from the previous figures, the dimensions of $B2$ are equal to $B1$ and thus both the equations and thermal phenomena are the same:

$$\frac{dT}{dt} = \dot{E}_{Conv,B2} + \dot{E}_{Rad,B2} + \dot{E}_{Cond,B2} + \dot{E}_{Gen,B2}, \text{where } m = n_{B1}^2, \ldots, n_{B1}^{End} \tag{60}$$

IX. Boundary Equations where Busbar$_2$ connects to PSU

Finally, the *B2* is connected to the PSU-Cable and this is where the FDM division ends. Thus, it is necessary to write the boundary equation equivalent to the (52) so that the system is well defined and can be solved:

$$\frac{dT}{dt} = \frac{1}{2}\dot{E}_{Conv,B2-PSU} + \frac{1}{2}\dot{E}_{Rad,B2-PSU} + \dot{E}_{Cond,B2-PSU} + \frac{1}{2}\dot{E}_{Gen,B2-PSU} \tag{61}$$

The Equation (61) is solved only for the boundary node m_{B2}^{End}.

Solving the FDM equations system

To validate the developed model (see **Chapter 5.1**), the temperatures could be easily extracted from the temperature matrix by indexing $x_m = m\Delta x$ the positions of placed thermocouples with the corresponding temperature at that node $T(x_m) = T_m$. The resulting matrix $\boldsymbol{T}(T_m, t)$ has a dimension of (N, J) where the number of rows N represents the nodal points and J is the length of time vector used for evaluation. The result is a system of N algebraic equations and represented in matrix form:

$$\frac{d\boldsymbol{T}}{dt} = f(t, \boldsymbol{T}), \quad \boldsymbol{T}(t_0) = T_{\mathbf{0}} \tag{62}$$

where t, is the independent variable of time and $\boldsymbol{T}$ is the vector with of dependent variables of thermocouple temperature:

$$\boldsymbol{T}(t) := \begin{bmatrix} T(t)_1 \\ \vdots \\ T(t)_{N-1} \\ T(t)_N \end{bmatrix} \tag{63}$$

After specifying the initial conditions:

$$\boldsymbol{T}(t_0) = \begin{bmatrix} T_{Room} \\ \vdots \\ T_{Room} \\ T_{Room} \end{bmatrix} \tag{64}$$

where T_{Room} is the initial temperature for every component, the system is set and can be solved. Nevertheless, the different regions are fully dependent on each other the energy balance equations must be solved simultaneously. There are numerous methods to solve a system of algebraic equations, but the *Forward Euler Method* is one of the methods which is efficient from the computational point of view. Given the initial problem from Equation (62), which cannot be evaluated analytically (see **Chapter 4.1.1**), has the limit $\Delta t \to 0$, that defines the derivate:

$$\frac{d\boldsymbol{T}}{dt} = \lim_{\Delta t \to 0} \frac{\boldsymbol{T}(t + i\Delta t) - \boldsymbol{T}(t)}{\Delta t} \tag{65}$$

■ife

As introduced in the previous chapter, the differential Equation (65) can be approximated with the difference equation:

$$f\big(t, \boldsymbol{u}(t)\big) = \frac{\boldsymbol{u}(t + i\Delta t) - \boldsymbol{u}(t)}{\Delta t} \tag{66}$$

Given $\boldsymbol{u}(t)$ at time step $t = i\Delta t$, the $\boldsymbol{u}(t)$ can be computed at later time $t + i\Delta t$, by solving following finite difference equation:

$$\boldsymbol{u}(t + i\Delta t) = \boldsymbol{u}(t) + \Delta t f\big(t, \boldsymbol{u}(t)\big) \tag{67}$$

Which represents the exactly one-time step of the *Forward Euler Method*. With introduced notation from the FDM for any of the finite volume elements *m:*

$$\boldsymbol{u}_m^{t+i\Delta t} = \boldsymbol{u}_m^t + \Delta t f(t, \boldsymbol{u}_m^t) \tag{68}$$

From the computational point of view, the Equation (68) is very efficient because it includes the two basic mathematical operations such as addition and multiplication. Thus, it can be easily coded in some of the programming languages and the program of choice in this work was MATLAB. Even though the algorithm was fully developed in MATLAB, in the following text the method of entering the MATLAB code and algorithm will not be explained because it would go beyond the scope of work. Extensive literature can be found on the Internet, as well as numerous tutorials on the basics of MATLAB as well as Euler's method.

4.3 Thermal Model Generation for Relay

The relay posed a greater challenge when creating the thermal model. Mainly because of its complex internal structure. In *Figure 56* a cross-section through the tested relay is presented. To create a thermal model, simplifications had to be assumed. The simplification that made the most sense, was that only the part of the relay circled in red was modelled in the thermal model.
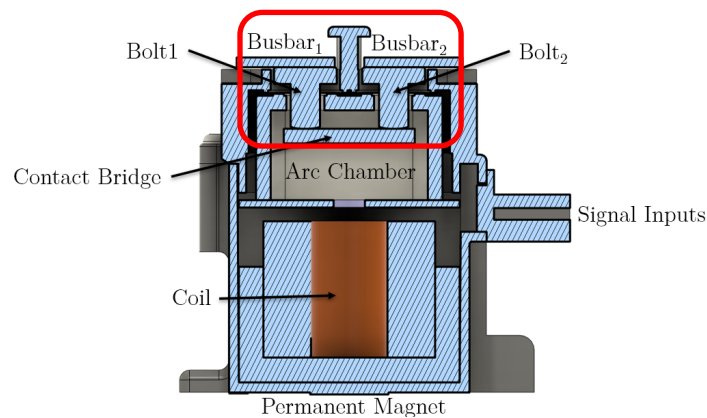
Figure 56: Cross-section of tested relay

The internal part of the relay and the connected busbars used for the thermal model building are shown in **Figure 57**. The relay coil and the other metal and plastic parts are not part of the model. Nevertheless, their effect on the thermal behaviour cannot be neglected and they are indirectly coupled into the model by substitute heat flux (see Equation (76)).
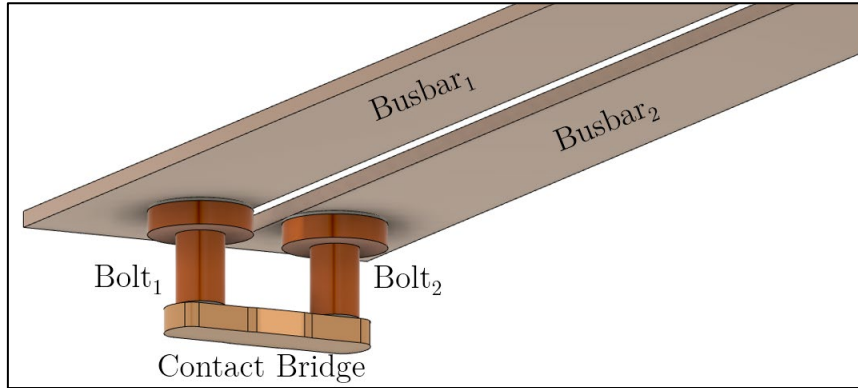
Figure 57: Simplified model of the relay used for thermal model building

The change in the thermal state of the geometry is due to the current flow *I*, and the way the thermal equations are set up is completely analogous to the thermal model of the shunt in previous **Chapter 4.2**. Thus, the geometry from **Figure 57** is divided into finite volumes with internal nodes and for each of the nodes, the thermal equations are set up. For simplicity reasons the geometry was divided into different regions:

The interested reader is at this point referenced to **Appendix B** where all the thermal equations are given in the full form. They were intentionally left out so that the text would not be cluttered with formulas.

I.   Boundary Equations where Busbar₁ connects to PSU-Cable

The connection with the PSU-Cable was selected as the starting point for the FDM analysis and because of the same geometrical and physical properties the governing equation is the same as Equation (89):

$$\frac{dT}{dt} = \frac{1}{2}\dot{E}_{Conv,B1-PSU} + \frac{1}{2}\dot{E}_{Rad,B1-PSU} + \dot{E}_{Cond,B1-PSU} + \frac{1}{2}\dot{E}_{Gen,B1-PSU} \qquad (69)$$

II.   Node Equation for Busbar₁

The *B1* for the relay test setup was the same, so the formulations are equivalent to the Equation (94):

$$\frac{dT}{dt} = \dot{E}_{Conv,B1} + \dot{E}_{Rad,B1} + \dot{E}_{Cond,B1} + \dot{E}_{Gen,B1}, \qquad \text{where } m = n_{B1}^2, \dots, n_{B1}^{End} \qquad (70)$$

III.   Boundary Equations where Busbar$_1$ connects to Bolt$_1$

Because the relay is hermetically sealed with H$_2$, the mass of the gas is very small, so the convection can be neglected. Furthermore, the radiation is just a small part of the thermal distribution and it is also neglected. Thus, the boundary equation is easier to solve and not demanding for the CPU:

$$\frac{dT}{dt} = \dot{E}_{Cond,B1-BT1} + \dot{E}_{Gen,B1-BT1} \tag{71}$$

Important to add is the different approach for calculating the generated heat for the components placed inside the relay (Bolt$_1$, Contact Bridge, and Bolt$_2$). Because of the complex inner structure of the relay, the heat generated in the components is lost through *conduction* to plastic, ceramic of the arc chamber and the stell parts surrounding the coil. Thus, a function $F_{Gen_2} = f(I)$ was found trough MATLAB Curve Fitting Tool to mimic the real-world behaviour. It is a power function with 2 number of terms: $f(I) = a \cdot I^b + c$, where $a = \frac{3}{50}$, $b = 0.43$, and $c = 0.837$.

$$F_{Gen_2} = -\frac{3}{50} I^{0.43} + 0.837 \tag{72}$$

$$\dot{E}_{Gen,B1-BT1} = F_{Gen_2} \frac{I^2 \; \rho_{el,Cu}}{\rho_{Cu} c_{p,Cu} \left(\frac{D_{BTop}}{4}^2 \pi\right)^2} (1 + \alpha_{Cu}(T_{n_{BT2}^{End}} - T_{Ref})) \tag{73}$$

In this way, the complex 3D geometry of the relay was included in the simplified 1D thermal model. The terms of the $f(I)$ would differ for other types of the relay but can easily be found using the same Curve Fitting Tool.

IV.   Node Equation for Bolt$_1$

As for the boundary equation between Bolt$_1$ (*BT1*) and *B1*, the convection and radiation are neglected. The F_{Gen_2} describing the heating of other components is included as well. The energy conservation equation is:

$$\frac{dT}{dt} = \dot{E}_{Cond,BT1} + \dot{E}_{Gen,BT1}, \qquad \text{where } m = n_{BT1}^2, \ldots, n_{BT1}^{End} \tag{74}$$

V.   Boundary Equation for the contact between Bolt$_1$ and Bridge

Because the geometry of the Contact Bridge (*BR*) is different, so it was necessary to include a boundary equation at the contact point of the two components. Again, the convection and radiation is neglected with included F_{Gen_2} factor:

$$\frac{dT}{dt} = \dot{E}_{Cond,BT1-BR} + \dot{E}_{Gen,BT1-BR} \tag{75}$$

VI.   Node Equation for Bridge

The heat is generated in the coil, which is connected to 12 V_{DC} when the relay contacts are closed. According to the laws of thermodynamics, the heat generated in the coil must be transferred or converted into other forms of energy. Part of this energy is transferred to the BR, and in the thermal model, this energy defined as the heat flux. According to the datasheet of the tested relay, the generated power in standby mode (= the relay contacts are closed but there is no current flowing through) is $P_{StandBy} = 4.2$ W and approximately 25% of this power are transferred to the BR:

$$\dot{H}F_{Coil} = \frac{\dot{q_{Coil}}}{\rho_{Cu}c_{p,Cu}\,a_{BR}b_{BR}dx}a_{BR}dx, \quad \text{where } \dot{q_{Coil}} = \frac{25\% \cdot P_{StandBy}}{a_{BR}L_{BR}}\left[\frac{\text{W}}{\text{m}^2}\right] \quad (76)$$

where a_{BR} is the width of the BR and L_{BR} is the length of the BR. Reason why the $\dot{q_{Coil}}$ [W/m²] was divided by the $a_{BR}L_{BR}$ [m²] is to preserve the units. In *Figure 58* the heat flux from coil $\dot{H}F_{Coil}$ is represented in schematic way for easier understanding. It is understood that the $\dot{H}F_{Coil}$ is only applied to the bottom surface of the BR and for each of its nodes.
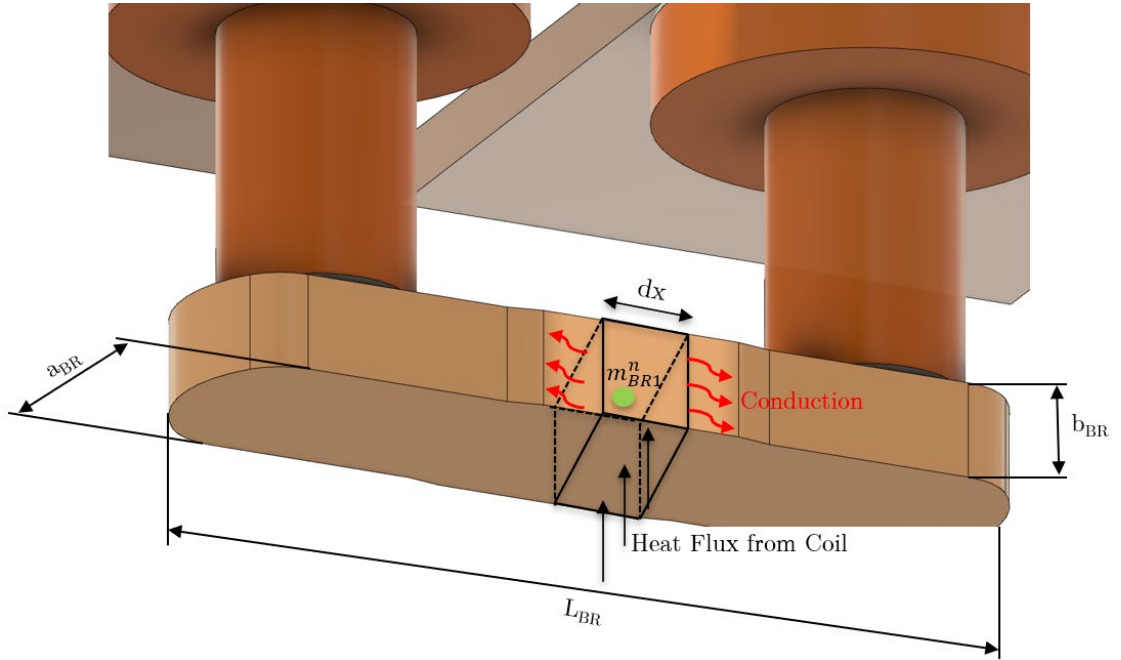
Figure 58: Transfer of the heat generated in the coil to the contact bridge

The governing equation for the BR node can be written as:

$$\frac{dT}{dt} = \dot{E}_{Cond,BR} + \dot{E}_{Gen,BR} + \dot{H}F_{Coil}, \quad \text{where } m = n_{BR}^1, \dots, n_{BR}^{End} \quad (77)$$

Because the geometry is symmetrical it is easy to conclude that the node equations for the other side of the relay test geometry are equivalent to previous. In further text, only the node equations are given, and the interested reader is once again pointed to **Appendix B** where the equations are given in the full form.

VII.   Boundary Equation for the contact between Bridge and Bolt$_2$

$$\frac{dT}{dt} = \dot{E}_{Cond,BT2-BR} + \dot{E}_{Gen,BT2-BR} \tag{78}$$

VIII.   Node Equation for Bolt$_2$

$$\frac{dT}{dt} = \dot{E}_{Cond,BT2} + \dot{E}_{Gen,BT2}, \qquad where\ m = n_{BT2}^1, \ldots, n_{BT2}^{End-1} \tag{79}$$

IX.   Boundary Equations where Busbar$_2$ connects to Bolt$_2$

$$\frac{dT}{dt} = \dot{E}_{Cond,B2-BT2} + \dot{E}_{Gen,B2-BT2} \tag{80}$$

X.   Node Equation for Busbar$_2$

$$\frac{dT}{dt} = \dot{E}_{Conv,B2} + \dot{E}_{Rad,B2} + \dot{E}_{Cond,B2} + \dot{E}_{Gen,B2}, \qquad where\ m = n_{B2}^1, \ldots, n_{B2}^{End-1} \tag{81}$$

XI.   Boundary Equations where Busbar$_2$ connects to PSU-Cable

$$\frac{dT}{dt} = \frac{1}{2}\dot{E}_{Conv,B2-PSU} + \frac{1}{2}\dot{E}_{Rad,B2-PSU} + \dot{E}_{Cond,B2-PSU} + \frac{1}{2}\dot{E}_{Gen,B2-PSU} \tag{82}$$

The developed FDM thermal models for the shunt and relay would not have any value if they do not correspond to the measured values. In **Chapter 5** the calculated temperatures for the different positions of thermocouples for the tested shunt and relay are compared with the measured data. Furthermore, a small statistical evaluation is given so the temperature curves can be compared in the mathematical sense.

5 Model Validation

During the process of thermal model building of different BDU components (e.g. shunts and relay), there must be a concern of how closely the developed model reflects the real system. There will always be a difference between the developed model and the real system. Nevertheless, the model must be within the domain of applicability, meaning it is sufficiently accurate for the intended application. There is no simple test to establish the validity of a model, as the validation is an inductive process in which the modeller concludes its accuracy. If the model is compared to the real system and there is no large discrepancy between the two, it is said that the model has validity. (Schlesinger, 1979)

5.1 Model Validation for Shunt

A thermal modelling method was developed to use for estimation of temperatures on the Samsung SDI shunts and parts of connected busbars (see *Figure 22*). This provided a simple method to evaluate the temperatures, which can be critical points during EV operation. For the validation of the model, the measurements on shunts (see *Chapter 3.1*) were used as a basis. The generalized approach described in *Chapter 4.2* is used to describe the capability of the thermal model and particularly its adaptation to calculations of temperatures. The temperatures measured with thermocouples are functions of time and the model needed to be solved in transient state. The comparison between the measured and calculated temperatures are given in the figures below.

During the measurements, a large amount of data was obtained and for the reason of simplicity, the different temperature distributions for each of the mounted thermal sensors ($T(t)_{T01}$ to $T(t)_{T13}$) are shown in one figure. Their position is given in *Chapter 3.1.2* and schematically in *Figure 50*. Furthermore, the figures are given just for $shunt_A$ with connected 40, 60, and 80 mm² busbars. Besides the visual interpretation of the validity of the developed model, a simple statistical calculation between the measured and model data has been performed.
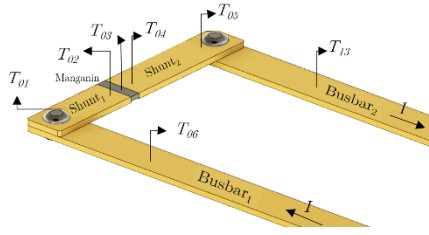
■ife
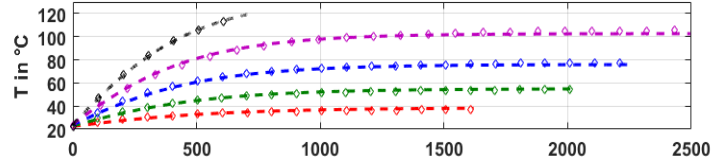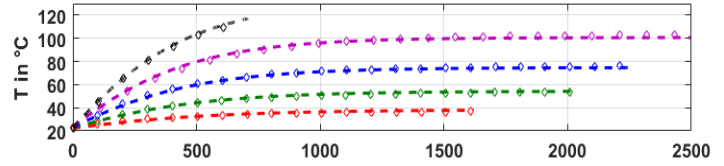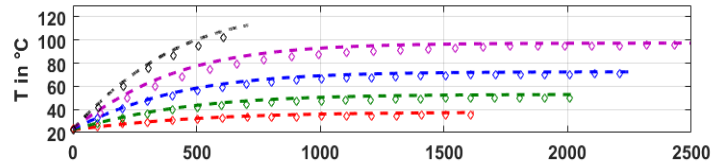
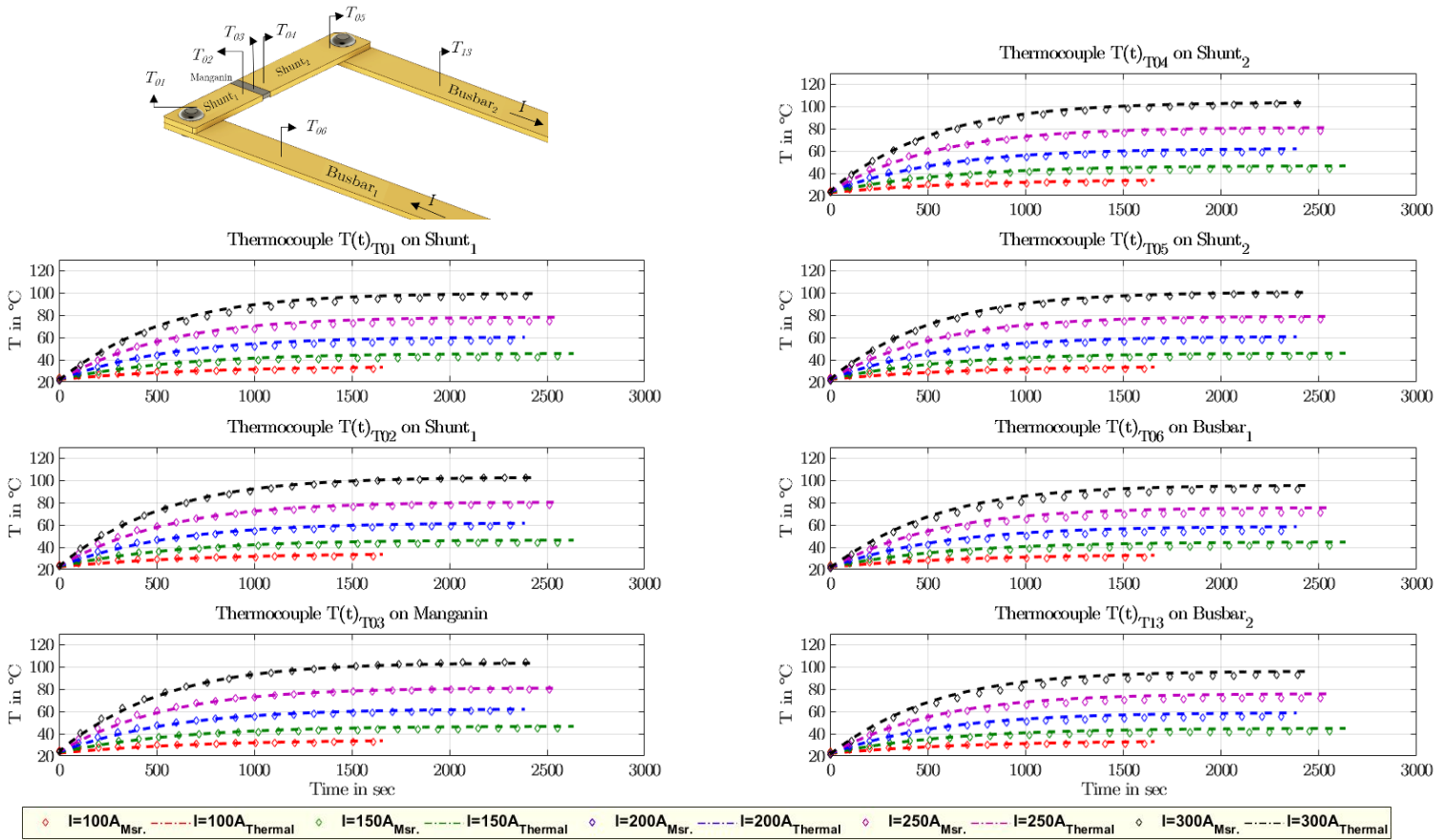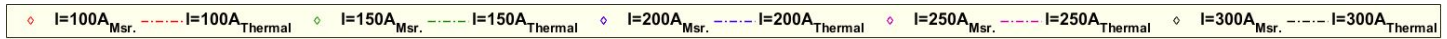➢ **Shunt$_A$ with connected 40 mm^2 cross-section busbar**
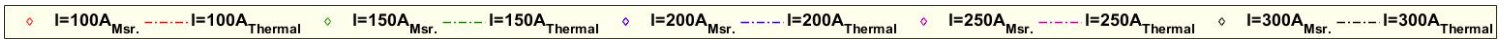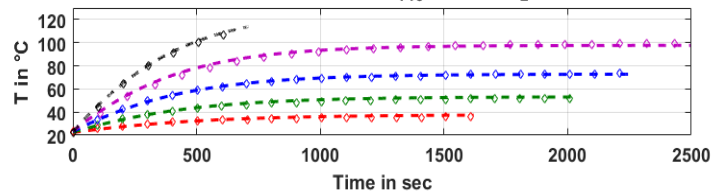
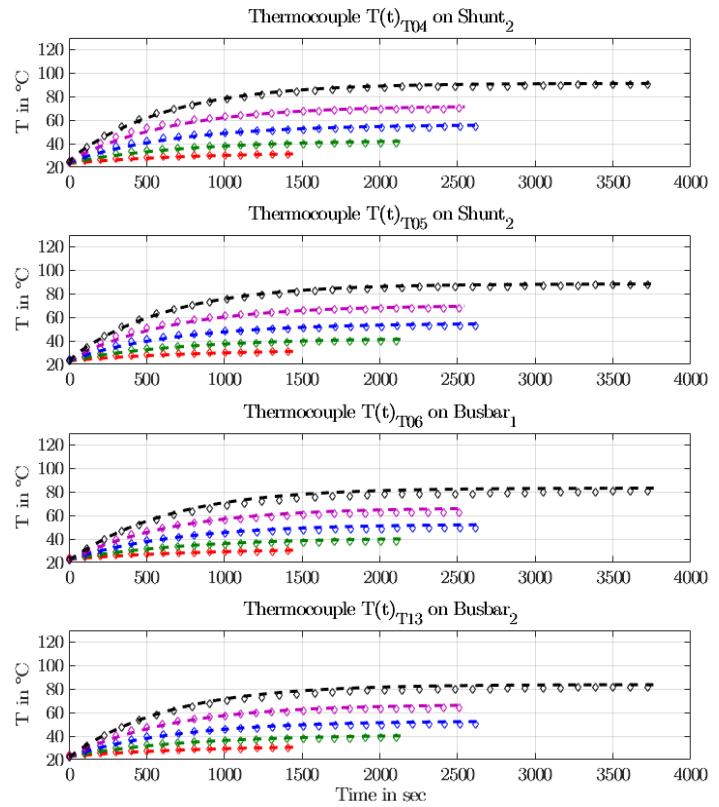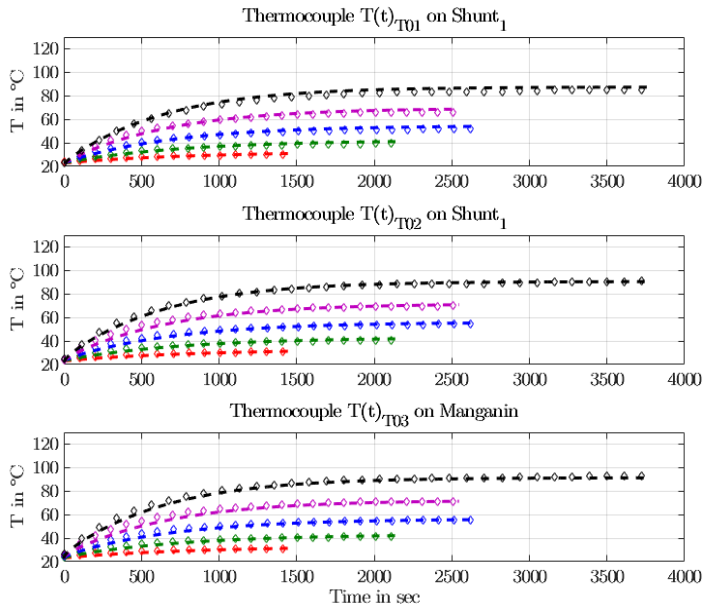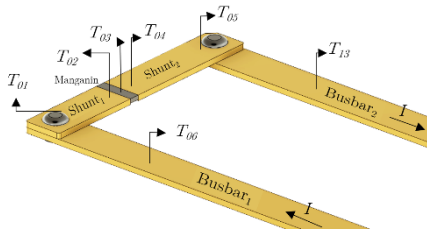**Figure 59:** Comparison between the developed thermal model (dashed line) and measured data (circles) for shunt$_A$ with connected 40 mm^2 cross-section busbar. The position of the mounted thermocouples is given in the upper left corner of the figure.

Looking at **Figure 59**, the shunt$_A$ and busbar was initially at the reference temperature $T_{Ref} = 23$°C. The thermal equilibrium was disturbed by the input current sequence $I = 100, 150, 200, 250$, and 300 A (which cover the current-draw range of normal EV operation). Because of generated heat, the shunt$_A$ and busbar heat up in logarithmic curve fashion until the new thermal equilibrium state is achieved. The logarithmic curve trend is due to the thermal mass C_{th}, which is analogous to the electrical capacitance C and the convection and conduction lose. The new steady state is achieved first for the 100 A input, and the longest time to the new steady-state was for 250 A. The reason the black curve for the 300 A is that short is that the maximum temperature of 120°C was reached very fast and the test is stopped (see **Test Description for Shunts**). Looking at the temperature curves, the thermal model reflects very well the temperature curves obtained from the measurements.

Table 12 shows the maximal relative error η for the *last* 15 min of temperature measurement:

$$\eta = max \left| \frac{T(t)_{Measured} - T(t)_{Model}}{T(t)_{Measured}} \right| \tag{83}$$

between the measured and temperatures gained through the thermal model. The reason why the two curves are compared for the last 15 min is that the thermal equilibrium and the maximal temperature of the components have been achieved. The maximal temperature difference ΔT_{Max} (e.g. absolute error) between the two curves for the last 15 min is also shown in **Table 12**:

$$\Delta T_{Max} = max |T(t)_{Measured} - T(t)_{Model}| \tag{84}$$

Thermocouple		I = 100A		I = 150A		I = 200A		I = 250A		I = 300A	
		η	ΔT_{Max}	η	ΔT_{Max}	η	ΔT_{Max}	η	ΔT_{Max}	η	ΔT_{Max}
Position		%	°C	%	°C	%	°C	%	°C	%	°C
Shunt 1	$T(t)_{T01}$	5.32	1.90	3.50	1.82	0.40	0.29	0.09	0.09	4.18	4.65
	$T(t)_{T02}$	4.10	1.50	1.95	1.04	1.45	1.11	2.20	2.29	1.11	1.30
	$T(t)_{T03}$	3.01	1.12	0.57	0.31	2.84	2.22	3.56	3.78	0.50	0.61
	$T(t)_{T04}$	3.60	1.33	1.18	0.64	1.93	1.50	2.57	2.71	0.71	0.84
	$T(t)_{T05}$	0.71	1.26	1.34	0.72	1.83	1.39	2.24	2.31	2.24	1.88
Busbar 1	$T(t)_{T06}$	6.84	2.39	5.86	2.93	2.38	1.68	1.36	1.31	5.93	6.32
Busbar 2	$T(t)_{T13}$	4.44	1.59	2.65	1.37	0.71	0.52	1.54	1.53	2.03	2.26
Max. value		6.84	2.39	5.86	2.93	2.84	2.22	3.56	3.78	5.93	6.32

Table 12: Maximal relative error and the maximal temperature difference between the measured and model data for shunt$_A$ with connected 40 mm^2 cross-section busbar.

The maximal relative error η for every thermocouple position and the whole-time span is below 7%, and the maximal temperature difference ΔT_{Max} does not exceed 4°C. This implies the usability of the developed FDM model. Nevertheless, the model could be improved by introducing the second dimension or choosing smaller dx.

■**ife**

➢ **Shunt$_A$ with connected 60 mm^2 cross-section busbar**

Figure 60: Comparison between the developed thermal model (dashed line) and measured data (circles) for shunt$_A$ with connected 60 mm^2 cross-section busbar. The position of the mounted thermocouples is given in the upper left corner of the figure.

The initial thermal equilibrium is, again, disturbed by the same input current sequence. The components are heated up until a new steady-state is reached. Nevertheless, the temperature curves resemble the curves from **Figure 59**. To compare the measured curves and thermal model curves the maximal relative error η and maximal temperature difference ΔT_{Max} for the last 15 min has been evaluated and is represented in **Table 13** below. The reason why 120°C is not achieved for 300 A may lie in the fact, that the busbars have larger convection and radiation area. Because of that, the cooling of the busbars is much better, and the heat generated in the shunt is transferred to the cooler busbars via conduction. This implies that by carefully choosing and optimizing the busbar area, the whole system could dissipate the heat much better even if the geometry of the shunt and relay is left the same. Looking at **Table 13** the maximal relative error is 7.7% and the maximal temperature difference is 5.92°C for every thermocouple and every current.

Thermocouple		I = 100A		I = 150A		I = 200A		I = 250A		I = 300A	
		η	ΔT_{Max}	η	ΔT_{Max}	η	ΔT_{Max}	η	ΔT_{Max}	η	ΔT_{Max}
Position		%	°C	%	°C	%	°C	%	°C	%	°C
Shunt 1	$T(t)_{T01}$	5.60	1.76	6.84	2.93	5.69	3.25	5.02	3.75	2.88	2.79
	$T(t)_{T02}$	4.58	1.47	5.28	2.33	3.81	2.26	2.69	2.11	0.40	0.41
	$T(t)_{T03}$	4.15	1.34	4.18	1.87	2.61	1.58	1.35	1.08	0.92	0.96
	$T(t)_{T04}$	4.90	1.58	5.62	2.48	4.45	2.64	3.44	2.69	1.31	1.34
	$T(t)_{T05}$	4.61	1.47	5.46	2.38	4.28	2.49	3.29	2.52	1.34	1.33
Busbar 1	$T(t)_{T06}$	6.09	1.89	7.69	3.19	6.71	3.68	5.92	4.22	3.69	3.40
Busbar 2	$T(t)_{T13}$	5.39	1.69	6.83	2.87	6.01	3.33	5.01	3.62	3.75	3.47
Max. value		6.09	1.89	7.69	3.19	6.71	3.68	5.92	4.22	3.75	3.47

Table 13: Maximal relative error and the maximal temperature difference between the measured and model data for shunt$_A$ with connected 60 mm² cross-section busbar

➢ Shunt$_A$ with connected 80 mm² cross-section busbar

Figure 61: Comparison between the developed thermal model (dashed line) and measured data (circles) for shunt$_A$ with connected 80 mm² cross-section busbar. The position of the mounted thermocouples is given in the upper left corner of the figure.

The temperature curves in **Figure 61** resemble the measurement data very well. The reason why the temperature curve for 300 A is so long may lie in the fact that a greater area of busbars is dissipating heat much better. The overall temperatures are lower than for the smaller busbar cross-sections. The similarity between the measured and thermal model curves is given in **Table 14**, where the maximal relative error is 5.54% and the maximal temperature difference does not exceed 3.3°C.

Thermocouple		I = 100A		I = 150A		I = 200A		I = 250A		I = 300A	
		η	ΔT_{Max}	η	ΔT_{Max}	η	ΔT_{Max}	η	ΔT_{Max}	η	ΔT_{Max}
Position		%	°C	%	°C	%	°C	%	°C	%	°C
Shunt 1	$T(t)_{T01}$	2.32	0.70	4.50	1.77	4.06	2.10	3.84	2.54	2.50	2.13
	$T(t)_{T02}$	1.14	0.35	2.93	1.19	1.87	1.01	1.26	0.88	0.35	0.31
	$T(t)_{T03}$	0.50	0.16	1.70	0.70	0.57	0.32	0.23	0.16	1.75	1.62
	$T(t)_{T04}$	1.29	0.40	3.45	1.40	2.61	1.42	2.22	1.55	1.00	0.90
	$T(t)_{T05}$	1.40	0.43	3.28	1.31	2.71	1.44	2.25	1.53	0.90	0.79
Busbar 1	$T(t)_{T06}$	2.89	0.86	5.54	2.11	5.38	2.67	5.12	3.21	3.50	2.82
Busbar 2	$T(t)_{T13}$	1.73	0.52	4.17	1.62	3.87	1.95	3.67	2.35	2.52	2.06
Max. value		2.89	0.86	5.54	2.11	5.38	2.67	5.12	3.21	3.50	2.82

Table 14: Maximal relative error and the maximal temperature difference between the measured and model data for shunt$_A$ with connected 80 mm² cross-section busbar

5.2 Model Validation for Relay

In comparison to the shunt, the relay is of symmetrical structure (see **Figure 56**), so it was sufficient to consider only one side for thermal model validation. In **Figure 62** the left side of the test setup with *B1, BT1,* and the *BR* is shown. As pointed out earlier, the relay is hermetically sealed, so it was not possible to place the thermocouples inside the relay. The thermocouple closest to the *BR* is the thermocouple T_{01}.
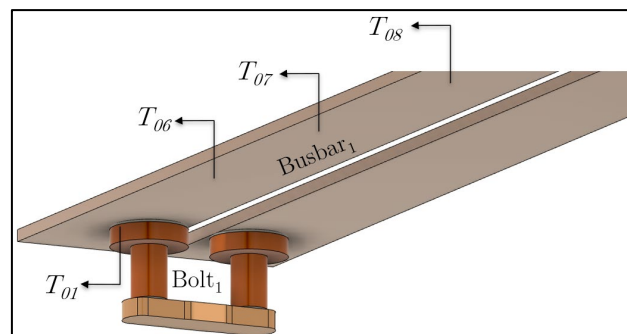
Figure 62: The inner structure of the relay is symmetrical thus it is sufficient to compare just one site to the measurement data. The position of the mounted thermocouples is also presented in the figure.

A current sequence ranging from 60 to 240 A was passed through the relay, and as can be concluded only by observing the curves in *Figure 63*, they correspond quite well to the measurements for currents from 60 to 168 A. For currents 210 and 240 A we notice a deviation from the measured for $t = 0$ s to $t = 1300$ s. This is a consequence of the complex structure of the relay where, in addition to copper and iron, there are a lot of plastic and ceramics parts, which are characterized by poor conduction properties, thus, they heat up much slower compared to metal. This deviation could be corrected by raising the complexity of the thermal system and considering other dimensions. As the thermal simulation is developed only in one dimension, the curves correspond well to each other.
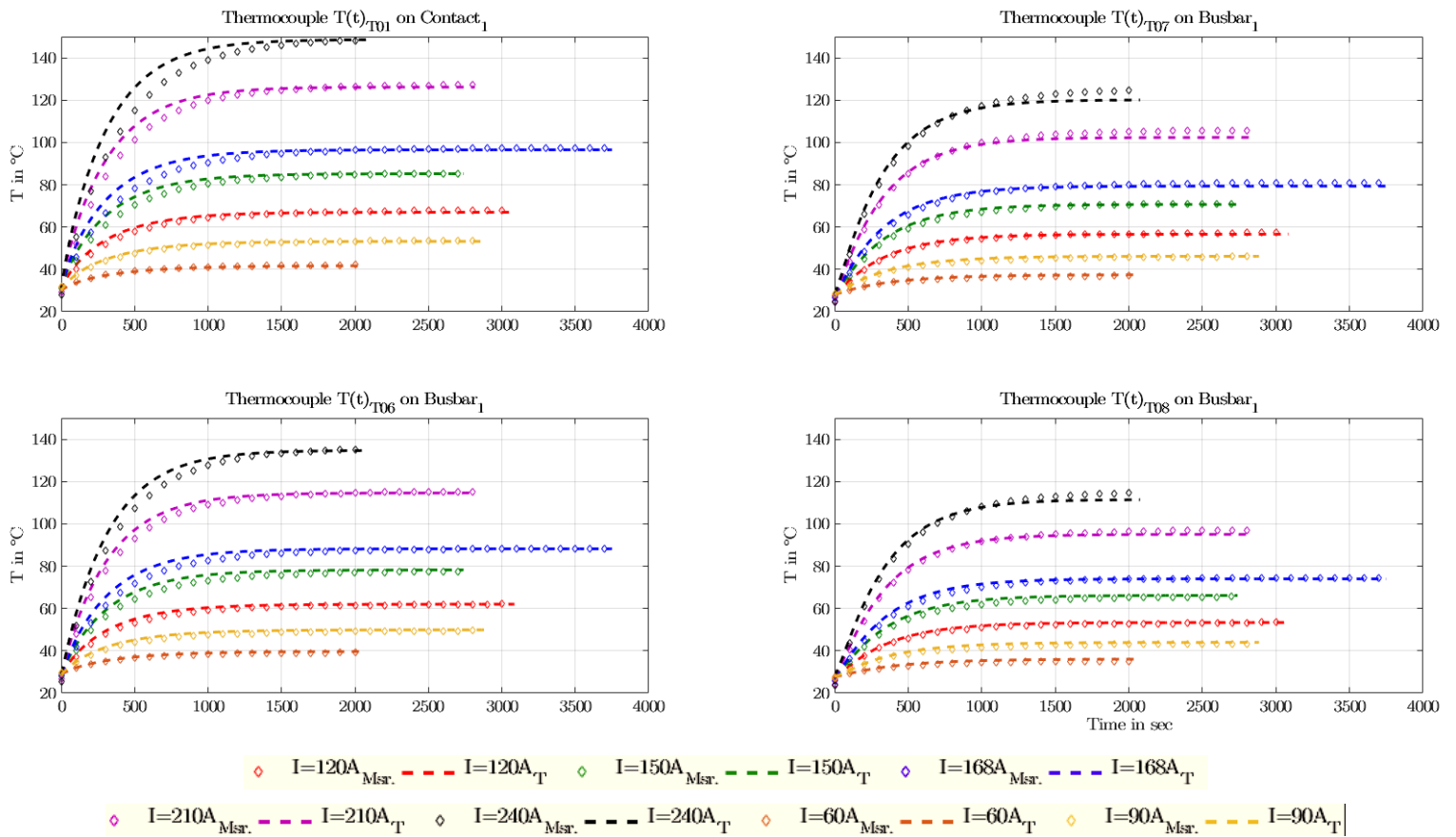
Figure 63: Comparison between the developed thermal model and measured data for the relay and connected 40 mm² cross-section busbar. The position of corresponding thermocouples is given in *Figure 62*.

As for the model validation for shunt, a small statistical evaluation is performed to compare the data (see **Table 15**). The maximal relative error and maximal temperature difference were calculated for the last 15 min thus, the thermal equilibrium and the maximal temperature of the components have been achieved.

Thermocouple		I = 60A		I = 90A		I = 120A		I = 150A		I = 168A		I = 210A		I = 240A	
		η	ΔT_{Max}	η	ΔT_{Max}	η	ΔT_{Max}	η	ΔT_{Max}	η	ΔT_{Max}	η	ΔT_{Max}	η	ΔT_{Max}
Position		%	°C	%	°C	%	°C	%	°C	%	°C	%	°C	%	°C
Contact 1	$T(t)_{T01}$	1.44	0.98	0.24	0.21	1.00	0.98	0.78	0.99	0.14	0.21	1.11	0.47	0.80	0.43
	$T(t)_{T06}$	0.19	0.12	0.95	0.73	0.05	0.04	0.53	0.61	0.46	0.62	1.14	0.45	0.84	0.42
Busbar 1	$T(t)_{T07}$	1.42	0.81	0.63	0.45	1.89	1.53	3.10	3.27	3.61	4.50	1.23	0.45	0.32	0.15
	$T(t)_{T08}$	0.24	0.13	0.65	0.43	0.55	0.41	1.98	1.92	2.90	3.33	2.76	0.97	1.69	0.73
Max. value		1.44	0.98	0.95	0.73	1.89	1.53	3.10	3.27	3.61	4.50	2.76	0.97	1.69	0.73

Table 15: Maximal relative error and maximal temperature difference between the measured and model data for the relay with connected 40 mm² cross-section busbar

Looking at **Table 15**, the maximal relative error is less than 3.7% and the maximal temperature difference is 4.5°C. Comparing this to **Table 12** (shunt$_A$ with connected 40mm² busbar), the η is smaller by 2.5%. This may lie in the fact, that the finite node element length dx was smaller and because of that the FDM was more accurate. Nevertheless, by optimizing the busbar geometry and the connection of the relay to the busbar, the heat could be dissipated much better from the relay and the components would not heat that much. Again, the thermal model could be optimized even more if the dx was smaller and more node equations would be solved. Considering other dimensions, the result would be even better. On the other hand, such complexity of the system and the number of equations would be a real challenge for the computational power of the CPU.

■ife

6 Thermal Model for the Battery Disconnect Unit

U sing the FDM for developing a thermal model for individual components placed inside the BDU, proved to be a valid and accurate method. However, the BDU with all its components forms a system, which only performs as it should if all the components are operating correctly. The next task was to create a thermal model that describes the behaviour of the part of the BDU used in Samsung SDI batteries. The combination of the components is shown in the following ***Figure 64***:
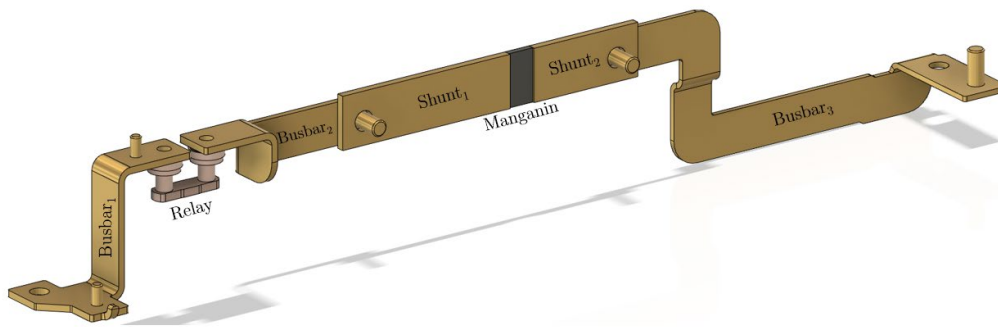
Figure 64: Combination of the components in Samsung SDI BDU used for the thermal building

As shown in ***Figure 64*** the components are already designed with the necessary simplifications, where for the relay only bolts and contact BR are shown. The governing idea was to combine the already developed node equations for shunt, busbar, and relay into one system. Even if more components are included in the system, their thermal behaviour could be easily described following the described steps. As for the shunt and relay, the geometry shown in ***Figure 64*** is divided into regions for easier FDM representation:

- Boundary Equation where $Busbar_1$ connects to the rest of BDU
- Node Equation for $Busbar_1$
- Node Equation for the contact between $Busbar_1$ and $Bolt_1$
- Node Equation for $Bolt_1$
- Node Equation for the contact between $Bolt_1$ and Bridge
- Node Equation for Bridge
- Node Equation for the contact between Bridge and $Bolt_2$
- Node Equation for $Bolt_2$

- Node Equation for the contact between $Bolt_2$ and $Busbar_2$
- Node Equation for $Busbar_2$
- Node Equation for $Shunt_1$
- Boundary Equations where $Shunt_1$ connects to Manganin
- Node Equation for Manganin
- Boundary Equations where Manganin connects to $Shunt_2$
- Node Equation for $Shunt_2$
- Node Equation for $Busbar_3$
- Boundary Equation where $Busbar_3$ connects to the rest of BDU

It is can be easily concluded that the same node equations from *Chapter 4.2* for shunt and *Chapter 4.3* for a relay are used here with no alternation. Once again, the full node equations are given in **Appendix A** and **Appendix B** for shunt and relay, respectively. The algebraic system of node equations is solved using the Forward Euler Method described in *Chapter 4.2* because of its simplicity to be coded into the MATLAB program.

The data for comparison was not obtained through measurements but was generated in 3D thermal simulation in COMSOL Multiphysics Simulation Software. In *Figure 65* the system is shown in thermal equilibrium after $t = 3600\ s$ when 100 A is passed through.
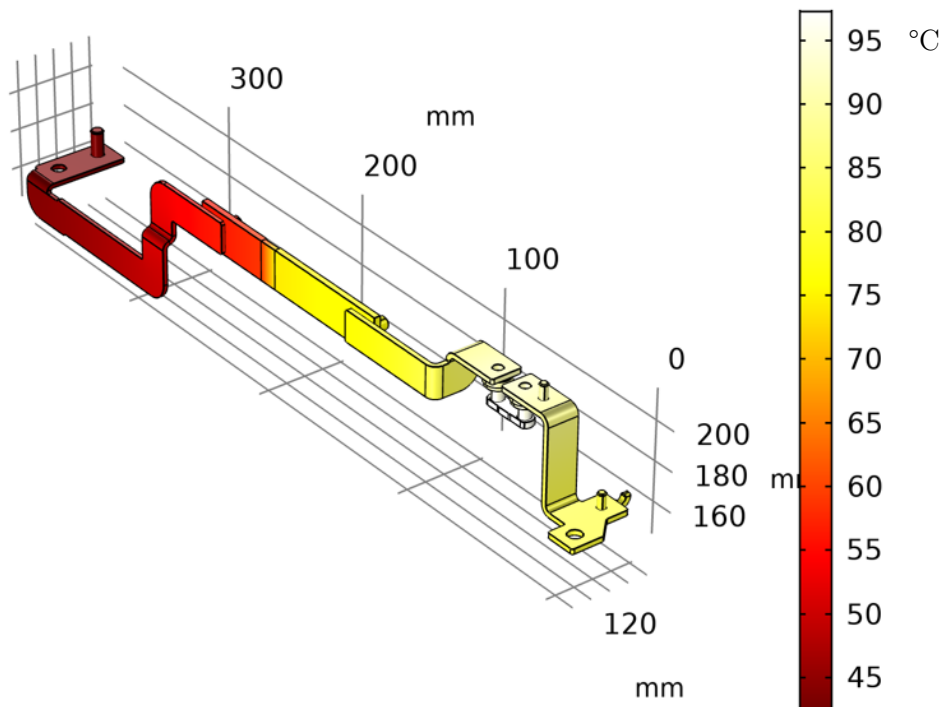
Figure 65: 3D thermal simulation of the Samsung SDI BDU

Because the relay is hermetically sealed there is no convection and minimal radiation. Furthermore, there is constant heat flux from the coil to the bottom side of the contact bridge, and the only way the heat is dissipated is through conduction to busbars and ceramic and plastic parts. Thus, the contact bridge is heated up the most. A total of 9 virtual thermocouples was placed on different positions during the 3D simulation. Their position is shown in **Figure 66**.
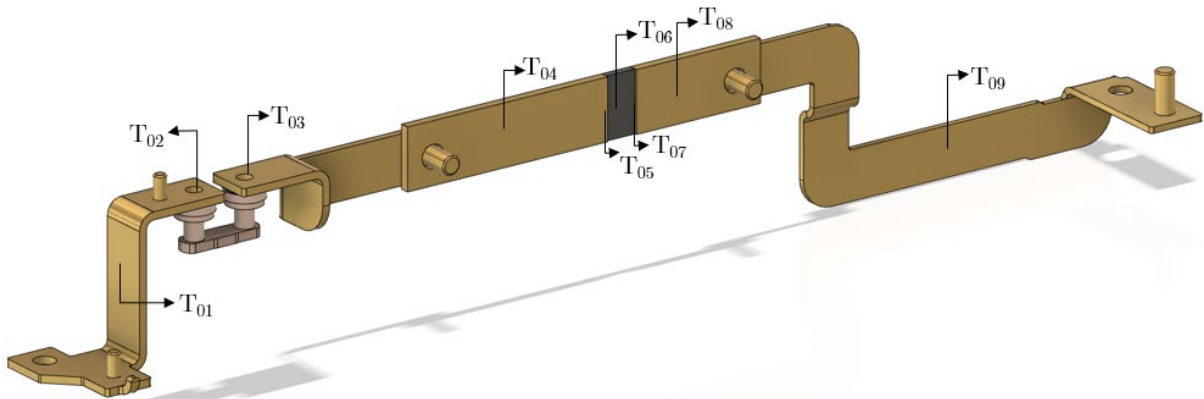
Figure 66: Position of virtual thermocouples in 3D thermal simulation

After the FDM thermal model was solved, the temperature data for every of the finite element nodes was obtained and it could be compared to simulation data for validation. In **Figure 67** the node temperature distribution is given for every node.
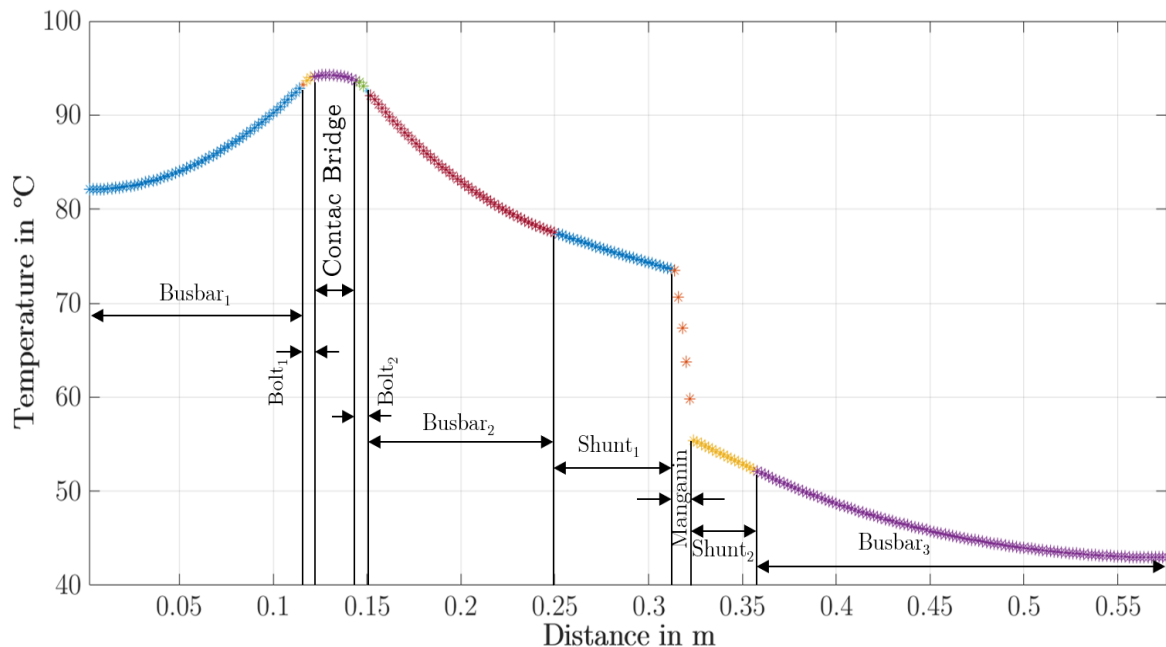
Figure 67: Nodes temperature distribution at $t = 3600\ s$

■ife

Different regions are annotated and as from the 3D thermal simulation, the *BR* is heated up the most. The reason why the nodes for the manganin part are so stretched is, that the conduction coefficient for manganin $k_M = 22\frac{W}{m \cdot K}$ is 18 times smaller than the conduction coefficient for copper $k_{Cu} = 389\frac{W}{m \cdot K}$. Therefore, the manganin conducts heat 18 times worse than copper, thus, parts of manganin dissipate heat at different speeds. In *Figure 68* the thermal model data is compared to the 3D simulation data of the virtually placed thermocouples shown in *Figure 66*.
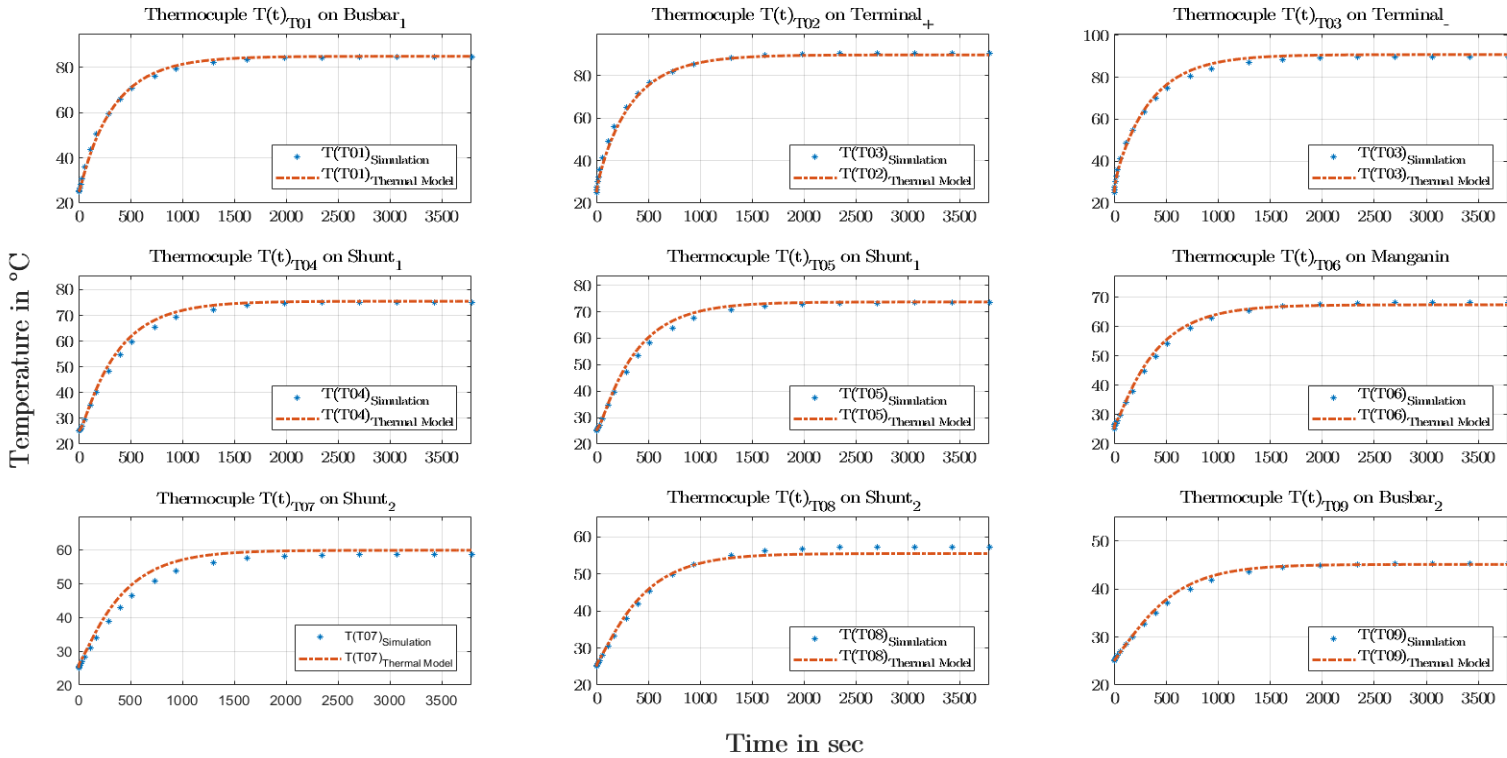
Figure 68: Comparison between the developed thermal model and simulation data for the BDU

Looking at the temperature curves, it can be stated that the FDM model resembles the simulated curves almost identically. The only noticeable difference is for the thermocouple T_{07} and T_{08} on shunt₂. The reason may lie in fact, that the exact nodes could not be extracted from the FDM simulation because the whole geometry is represented in 1D and the simulated geometry resembles the real-world component arrangement. The maximal relative error for all the thermocouples between the simulated and thermal model data is 3%, where the minimal relative error is just 0.3%. An interesting fact is that the simulation time in the 3D simulation software was 13 min and 21 sec, where the computation time for the developed thermal model was 40 sec, which is 20 times faster.

7 Conclusion and Outlook

Electro-thermal coupling under dynamic conditions in modern EVs BDUs using the current I as model input to generate thermal models was presented in this work. A trade-off between accuracy and speed of computation was embodied in 1D thermal models using the FDM. While the efficiency of calculation and minimal usage of BMS computer memory and CPU power is essential, the thermal model developed with FDM gives satisfactory accuracy using the Forward Euler Method for efficient computation. Thus, the average maximal relative error for the shunt$_A$ connected to different cross-sections of busbars was 5.1%, and on the other hand 2.2% for the tested relay with 40 mm^2 cross-section busbar. These results imply the usability of the developed FDM model. Using the developed FDM thermal model it is possible to predict the transient and maximal temperature of the different parts of BDU components, which are crucial for the safe operation of EV. Knowing the thermal efficiency of the BDU components can help to avoid switching problems and sink the probability of occurring accidents because of component failure.

FDM has proven to be a powerful method, where complex 3D geometry and related thermal processes could be simplified to a 1D representation. Using this method, the first forecasts for the temperature of the components can be estimated already at the design stage. At the same time, commercial 3D simulation software is not used, which often requires user experience. Furthermore, the commercial software often solves a large system of equations, and if the input geometry is complex, it often cannot be solved on the majority of CPUs. The computational time also depends on the complexity of geometry and it takes much longer than for the developed FDM thermal model, which is 20 times *faster* simulating the same input geometry as convectional software.

On the other hand, the commercial simulations software is completely independent of the input geometry into the program. In this way, the user has complete freedom to change the geometry if it does not exceed reasonable complexity. The generated thermal model does not provide this freedom to the user, because it is generated for the precisely defined geometry of the components used in the BDU. The FDM thermal model was intentionally developed this way to preserve the simplicity with the aim of efficient and sufficiently accurate calculation. It could certainly be extended to the other two dimensions, and a guided user interface could be programmed, but in this way, it would depict commercial software, which is developed by many engineers and programmers over many years.

Furthermore, the thermal equations used for the finite element volumes could be extended even further by analysing the selected components even more or by doing additional measurements and experiments where the exact thermal heat coefficients or heat dissipation mechanisms could be obtained. The length of the finite volumes dx used in the presented FDM models was selected in such a way, that the resulting algebraic system is not too demanding for the computational power of the CPU. Thus, it could be chosen much smaller $dx \rightarrow 0$, and the numerical solution would ultimately converge to the analytical solution. On the other hand, if the dx is chosen larger, the algebraic system would be solved much faster but to the detriment of the accuracy. One should ask, what simulation error can be accepted at the expense of a fast solution of the thermal equation system.

To sum up, the FDM thermal model was developed to calculate the transient and maximal temperatures during the heat up process in the BDU. It was developed for specific safety components (e.g. shunts and relay), which are not intended to change in geometry or physical properties. The developed model was verified by comparing it to measurements with satisfactory accuracy. Nevertheless, because of the limited time, the models could not be optimized even more. Thus, this thesis hopes to offer useful guidelines and sources of information for future thermal or related model development.

Appendices

Appendix A

Thermal Model for Shunt$_A$

Boundary Equations where Busbar$_1$ connects to PSU-Cable (subscript: B1-PSU)

Convection Part:

$$\dot{E}_{Conv,B1-PSU} = \underbrace{\frac{2}{\rho_{Cu}c_{p,Cu}a_B}\frac{7.66}{\sqrt[4]{b_B 10^3}}\sqrt[4]{\left(T_{Room} - T_{n^1_{B1}}\right)^5}}_{Vertical\ Surface} + \underbrace{\frac{2}{\rho_{Cu}c_{p,Cu}b_B}\frac{5.92}{\sqrt[4]{a_B 10^3}}\sqrt[4]{\left(T_{Room} - T_{n^1_{B1}}\right)^5}}_{Horizonal\ Surface} \tag{85}$$

Radiation Part:

$$\dot{E}_{Rad,B1-PSU} = \frac{2\ (a_B + b_B)\varepsilon\sigma}{\rho_{Cu}c_{p,Cu}\ a_B b_B}\left((T_{Room} + 273.15)^4 - (T_{n^1_{B1}} + 273.15)^4\right) \tag{86}$$

Conduction Part:

$$\dot{E}_{Cond,B1-PSU} = \frac{k_{Cu}}{\rho_{Cu}c_{p,Cu}}\frac{T_{n^2_{B1}} - T_{n^1_{B1}}}{dx^2} \tag{87}$$

Energy Generation Part:

$$\dot{E}_{Gen,B1-PSU} = F_{Gen_1}\frac{I^2\ \rho_{el,Cu}}{\rho_{Cu}c_{p,Cu}(a_B b_B)^2}(1 + \alpha_{Cu}(T_{n^1_{B1}} - T_{Ref})), \qquad where\ F_{Gen_1} = 0.85 \tag{88}$$

Energy Conservation Equation:

$$\frac{dT}{dt} = \frac{1}{2}\dot{E}_{Conv,B1-PSU} + \frac{1}{2}\dot{E}_{Rad,B1-PSU} + \dot{E}_{Cond,B1-PSU} + \frac{1}{2}\dot{E}_{Gen,B1-PSU} \tag{89}$$

Node Equation for Busbar$_1$ (subscript: B1)

Convection Part:

$$\dot{E}_{Conv,B1} = \underbrace{\frac{2}{\rho_{Cu}c_{p,Cu}a_B}\frac{7.66}{\sqrt[4]{b_B 10^3}}\sqrt[4]{[T_{Room} - T_m]^5}}_{Vertical\ Surface} + \underbrace{\frac{2}{\rho_{Cu}c_{p,Cu}b_B}\frac{5.92}{\sqrt[4]{a_B 10^3}}\sqrt[4]{[T_{Room} - T_m]^5}}_{Horizonal\ Surface} \tag{90}$$

Radiation Part:

$$\dot{E}_{Rad,B1} = \frac{2\ (a_B + b_B)\varepsilon\sigma}{\rho_{Cu}c_{p,Cu}a_B b_B}\left((T_{Room} + 273.15)^4 - (T_m + 273.15)^4\right) \tag{91}$$

Conduction Part:

$$\dot{E}_{Cond,B1} = \frac{k_{Cu}}{\rho_{Cu}c_{p,Cu}}\frac{T_{m-1} - 2T_m + T_{m+1}}{dx^2} \tag{92}$$

Energy Generation Part:

$$\dot{E}_{Gen,B1} = F_{Gen_1}\frac{I^2\ \rho_{el,Cu}}{\rho_{Cu}c_{p,Cu}(a_B b_B)^2}(1 + \alpha_{Cu}(T_m - T_{Ref})), \qquad where\ F_{Gen_1} = 0.85 \tag{93}$$

Energy Conservation Equation:

$$\frac{dT}{dt} = \dot{E}_{Conv,B1} + \dot{E}_{Rad,B1} + \dot{E}_{Cond,B1} + \dot{E}_{Gen,B1}, \qquad where\ m = n^2_{B1}, \ldots, n^{End}_{B1} \tag{94}$$

■ife

Node Equation for Shunt$_1$ (subscript: S1)

Convection Part:

No convection

Radiation Part:

$$\dot{E}_{Rad,S1} = \frac{2 \ (a_S + b_S)\varepsilon\sigma}{\rho_{Cu}c_{p,Cu} \ a_S b_S}((T_{Room} + 273.15)^4 - (T_m + 273.15)^4) \tag{95}$$

Conduction Part:

$$\dot{E}_{Cond,S1} = \frac{k_{Cu}}{\rho_{Cu}c_{p,Cu}}\frac{T_{m-1} - 2T_m + T_{m+1}}{dx^2} \tag{96}$$

Energy Generation Part:

$$\dot{E}_{Gen,S1} = F_{Gen_2}\frac{I^2\rho_{el,Cu}}{\rho_{Cu}c_{p,Cu}(a_S b_S)^2}(1 + \alpha_{Cu}(T_m - T_{Ref})), \qquad \text{where } F_{Gen_2} = 0.62 \tag{97}$$

Energy Conservation Equation:

$$\frac{dT}{dt} = \dot{E}_{Rad,S1} + \dot{E}_{Cond,S1} + \dot{E}_{Gen,S1}, \qquad \text{where } m = n_{S1}^2, \ldots, n_{S1}^{End} \tag{98}$$

Boundary Equations where Shunt$_1$ connects to Manganin: (subscript: S1-M)

Convection Part:

No convection

Radiation Part:

$$\dot{E}_{Rad,S1-M} = \frac{2 \ (a_S + b_S + a_M + b_M)\varepsilon\sigma}{(\rho_{Cu}c_{p,Cu}a_S b_S + \rho_M c_{p,M}a_M b_M)}((T_{Room} + 273.15)^4 - (T_{n_M^1} + 273.15)^4) \tag{99}$$

Conduction Part:

$$\dot{E}_{Cond,S1-M} = \frac{2 \ a_S b_S k_{Cu}}{(\rho_{Cu}c_{p,Cu}a_S b_S + \rho_M c_{p,M}a_M b_M)}\frac{T_{n_{S1}^{End}} - T_{n_M^1}}{dx^2} + \frac{2 \ a_M b_M k_M}{(\rho_{Cu}c_{p,Cu}a_S b_S + \rho_M c_{p,M}a_M b_M)}\frac{T_{n_M^2} - T_{n_M^1}}{dx^2} \tag{100}$$

Energy Generation Part:

$$\dot{E}_{Gen,S1-M} = F_{Gen_2}\frac{I^2\left(\frac{\rho_{el,Cu}}{a_S b_S}(1 + \alpha_{Cu}(T_{n_M^1} - T_{Ref})) + \frac{\rho_{el,M}}{a_M b_M}\right)}{(\rho_{Cu}c_{p,Cu}a_S b_S + \rho_M c_{p,M}a_M b_M)}, \qquad \text{where } F_{Gen_2} = 0.62 \tag{101}$$

Energy Conservation Equation:

$$\frac{dT}{dt} = \dot{E}_{Rad,S1-M} + \dot{E}_{Cond,S1-M} + \dot{E}_{Gen,S1-M} \tag{102}$$

Node Equation for Manganin (subscript: M)

Convection Part:

No convection

Radiation Part:

$$\dot{E}_{Rad,M} = \frac{2\ (a_M + b_M)\varepsilon\sigma}{\rho_M c_{p,M}\ a_M b_M}((T_{Room} + 273.15)^4 - (T_{n_M^2} + 273.15)^4) \tag{103}$$

Conduction Part:

$$\dot{E}_{Cond,M} = \frac{k_M}{\rho_M c_{p,M}}\frac{T_{n_M^1} - 2T_{n_M^2} + T_{n_{S2}^1}}{dx^2} \tag{104}$$

Energy Generation Part:

$$\dot{E}_{Cond,M} = F_{Gen_2}\frac{I^2\ \rho_{el,M}}{\rho_M c_{p,M}(a_M b_M)^2}, \qquad \text{where } F_{Gen_2} = 0.62 \tag{105}$$

Energy Conservation Equation:

$$\frac{dT}{dt} = \dot{E}_{Rad,M} + \dot{E}_{Cond,M} + \dot{E}_{Cond,M} \tag{106}$$

Boundary Equation where Manganin connects Shunt₂ (with subscript: S2-M)

Convection Part:

No convection

Radiation Part

$$\dot{E}_{Rad,S2-M} = \frac{2\ (a_S + b_S + a_M + b_M)\varepsilon\sigma}{(\rho_{Cu}c_{p,Cu}a_S b_S + \rho_M c_{p,M}a_M b_M)}((T_{Room} + 273.15)^4 - (T_{n_M^2} + 273.15)^4) \tag{107}$$

Conduction Part

$$\dot{E}_{Cond,S2-M} = \frac{2\ a_S b_S k_{Cu}}{(\rho_{Cu}c_{p,Cu}a_S b_S + \rho_M c_{p,M}a_M b_M)}\frac{T_{n_{S2}^2} - T_{n_{S2}^1}}{dx^2} + \frac{2\ a_M b_M k_M}{(\rho_{Cu}c_{p,Cu}a_S b_S + \rho_M c_{p,M}a_M b_M)}\frac{T_{n_M^2} - T_{n_{S2}^1}}{dx^2} \tag{108}$$

Energy Generation Part

$$\dot{E}_{Gen,S2-M} = F_{Gen_2}\frac{I^2\left(\frac{\rho_{el,Cu}}{a_S b_S}(1 + \alpha_{Cu}(T_{n_{S2}^1} - T_{Ref})) + \frac{\rho_{el,M}}{a_M b_M}\right)}{(\rho_{Cu}c_{p,Cu}a_S b_S + \rho_M c_{p,M}a_M b_M)}, \qquad \text{where } F_{Gen_2} = 0.62 \tag{109}$$

Energy Conservation Equation:

$$\frac{dT}{dt} = \dot{E}_{Rad,S2-M} + \dot{E}_{Cond,S2-M} + \dot{E}_{Gen,S2-M} \tag{110}$$

■ife

Node Equation for Shunt₂ (subscript: S2)

Convection Part:

No convection

Radiation Part:

$$\dot{E}_{Rad,S2} = \frac{2\ (a_S + b_S)\varepsilon\sigma}{\rho_{Cu}c_{p,Cu}\ a_S b_S}((T_{Room} + 273.15)^4 - (T_m + 273.15)^4) \tag{111}$$

Conduction Part:

$$\dot{E}_{Cond,S2} = \frac{k_{Cu}}{\rho_{Cu}c_{p,Cu}}\frac{T_{m-1} - 2T_m + T_{m+1}}{dx^2} \tag{112}$$

Energy Generation Part:

$$\dot{E}_{Gen,S2} = F_{Gen_2}\frac{I^2\ \rho_{el,Cu}}{\rho_{Cu}c_{p,Cu}(a_S b_S)^2}(1 + \alpha_{Cu}(T_m - T_{Ref})), \qquad \text{where } F_{Gen_2} = 0.62 \tag{113}$$

Energy Conservation Equation:

$$\frac{dT}{dt} = \dot{E}_{Rad,S2} + \dot{E}_{Cond,S2} + \dot{E}_{Gen,S2}, \qquad \text{where } m = n_{S2}^2, \ldots, n_{S2}^{End-1} \tag{114}$$

Node Equation for Busbar₂ (subscript: B2)

Convection Part:

$$\dot{E}_{Conv,B2} = \underbrace{\frac{2}{\rho_{Cu}c_{p,Cu}\ a_B}\frac{7.66}{\sqrt[4]{b_B}10^3}\sqrt[4]{[T_{Room} - T_m]^5}}_{Vertical\ Surface} + \underbrace{\frac{2}{\rho_{Cu}c_{p,Cu}\ b_B}\frac{5.92}{\sqrt[4]{a_B}10^3}\sqrt[4]{[T_{Room} - T_m]^5}}_{Horizonal\ Surface} \tag{115}$$

Radiation Part:

$$\dot{E}_{Rad,B2} = \frac{2\ (a_B + b_B)\varepsilon\sigma}{\rho_{Cu}c_{p,Cu}\ a_B b_B}((T_{Room} + 273.15)^4 - (T_m + 273.15)^4) \tag{116}$$

Conduction Part:

$$\dot{E}_{Cond,B2} = \frac{k_{Cu}}{\rho_{Cu}c_{p,Cu}}\frac{T_{m-1} - 2T_m + T_{m+1}}{dx^2} \tag{117}$$

Energy Generation Part:

$$\dot{E}_{Gen,B2} = F_{Gen_1}\frac{I^2\ \rho_{el,Cu}}{\rho_{Cu}c_{p,Cu}(a_B b_B)^2}(1 + \alpha_{Cu}(T_m - T_{Ref})), \qquad \text{where } F_{Gen_1} = 0.82 \tag{118}$$

Energy Conservation Equation:

$$\frac{dT}{dt} = \dot{E}_{Conv,B2} + \dot{E}_{Rad,B2} + \dot{E}_{Cond,B2} + \dot{E}_{Gen,B2}, \qquad \text{where } m = n_{B1}^2, \ldots, n_{B1}^{End} \tag{119}$$

■ife

Boundary Equations where Busbar₂ connects to PSU (subscript: B2-PSU)

Convection Part:

$$\dot{E}_{Conv,B2-PSU} = \underbrace{\frac{2}{\rho_{Cu}c_{p,Cu}\,a_B}\frac{7.66}{\sqrt[4]{b_B 10^3}}\sqrt[4]{\left(T_{Room} - T_{n_{B2}^{End+1}}\right)^5}}_{Vertical\ Surface} + \underbrace{\frac{2}{\rho_{Cu}c_{p,Cu}\,b_B}\frac{5.92}{\sqrt[4]{a_B 10^3}}\sqrt[4]{\left(T_{Room} - T_{n_{B2}^{End+1}}\right)^5}}_{Horizonal\ Surface} \qquad (120)$$

Radiation Part:

$$\dot{E}_{Rad,B2-PSU} = \frac{2\,(a_B + b_B)\varepsilon\sigma}{\rho_{Cu}c_{p,Cu}\,a_B b_B}((T_{Room} + 273.15)^4 - (T_{n_{B2}^{End+1}} + 273.15)^4) \qquad (121)$$

Conduction Part:

$$\dot{E}_{Cond,B2-PSU} = \frac{k_{Cu}}{\rho_{Cu}c_{p,Cu}}\frac{T_{n_{B2}^{End}} - T_{n_{B2}^{End+1}}}{dx^2} \qquad (122)$$

Energy Generation Part:

$$\dot{E}_{Gen,B2-PSU} = F_{Gen_1}\frac{I^2\,\rho_{el,Cu}}{\rho_{Cu}c_{p,Cu}(a_B b_B)^2}(1 + \alpha_{Cu}(T_{n_{B2}^{End+1}} - T_{Ref})), \qquad where\ F_{Gen_1} = 0.82 \qquad (123)$$

Energy Conservation Equation:

$$\frac{dT}{dt} = \frac{1}{2}\dot{E}_{Conv,B2-PSU} + \frac{1}{2}\dot{E}_{Rad,B2-PSU} + \dot{E}_{Cond,B2-PSU} + \frac{1}{2}\dot{E}_{Gen,B2-PSU} \qquad (124)$$

Appendix B

Thermal Model for Relay

Boundary Equations where Busbar₁ connects to PSU (subscript: B1-PSU)

Convection Part:

$$\dot{E}_{Conv,B1-PSU} = \underbrace{\frac{2}{\rho_{Cu}c_{p,Cu}a_B}\frac{7.66}{\sqrt[4]{b_B 10^3}}\sqrt[4]{\left(T_{Room}-T_{n_{B_1}^1}\right)^5}}_{Vertical\ Surface} + \underbrace{\frac{2}{\rho_{Cu}c_{p,Cu}b_B}\frac{5.92}{\sqrt[4]{a_B 10^3}}\sqrt[4]{\left(T_{Room}-T_{n_{B_1}^1}\right)^5}}_{Horizonal\ Surface} \tag{125}$$

Radiation Part:

$$\dot{E}_{Rad,B1-PSU} = \frac{2\,(a_B+b_B)\varepsilon\sigma}{\rho_{Cu}c_{p,Cu}\,a_B b_B}\left((T_{Room}+273.15)^4-(T_{n_{B_1}^1}+273.15)^4\right) \tag{126}$$

Conduction Part:

$$\dot{E}_{Cond,B1-PSU} = \frac{k_{Cu}}{\rho_{Cu}c_{p,Cu}}\frac{T_{n_{B_1}^2}-T_{n_{B_1}^1}}{dx^2} \tag{127}$$

Energy Generation Part:

$$\dot{E}_{Gen,B1-PSU} = F_{Gen_1}\frac{I^2\,\rho_{el,Cu}}{\rho_{Cu}c_{p,Cu}(a_B b_B)^2}(1+\alpha_{Cu}(T_{n_{B_1}^1}-T_{Ref})), \qquad where\ F_{Gen_1}=0.82 \tag{128}$$

Energy Conservation Equation:

$$\frac{dT}{dt} = \frac{1}{2}\dot{E}_{Conv,B1-PSU}+\frac{1}{2}\dot{E}_{Rad,B1-PSU}+\dot{E}_{Cond,B1-PSU}+\frac{1}{2}\dot{E}_{Gen,B1-PSU} \tag{129}$$

Node Equation for Busbar₁ (subscript: B1)

Convection Part:

$$\dot{E}_{Conv,B1} = \underbrace{\frac{2}{\rho_{Cu}c_{p,Cu}a_B}\frac{7.66}{\sqrt[4]{b_B 10^3}}\sqrt[4]{[T_{Room}-T_m]^5}}_{Vertical\ Surface} + \underbrace{\frac{2}{\rho_{Cu}c_{p,Cu}b_B}\frac{5.92}{\sqrt[4]{a_B 10^3}}\sqrt[4]{[T_{Room}-T_m]^5}}_{Horizonal\ Surface} \tag{130}$$

Radiation Part:

$$\dot{E}_{Rad,B1} = \frac{2\,(a_B+b_B)\varepsilon\sigma}{\rho_{Cu}c_{p,Cu}a_B b_B}\left((T_{Room}+273.15)^4-(T_m+273.15)^4\right) \tag{131}$$

Conduction Part:

$$\dot{E}_{Cond,B1} = \frac{k_{Cu}}{\rho_{Cu}c_{p,Cu}}\frac{T_{m-1}-2T_m+T_{m+1}}{dx^2} \tag{132}$$

Energy Generation Part:

$$\dot{E}_{Gen,B1} = F_{Gen_1}\frac{I^2\,\rho_{el,Cu}}{\rho_{Cu}c_{p,Cu}(a_B b_B)^2}(1+\alpha_{Cu}(T_m-T_{Ref})), \qquad where\ F_{Gen_1}=0.82 \tag{133}$$

Energy Conservation Equation:

$$\frac{dT}{dt} = \dot{E}_{Conv,B1}+\dot{E}_{Rad,B1}+\dot{E}_{Cond,B1}+\dot{E}_{Gen,B1}, \qquad where\ m=n_{B1}^2,\ldots,n_{B1}^{End} \tag{134}$$

■ife

Boundary Equations where Busbar₁ connects to Bolt₁ (subscript: B1-BT1)

Convection Part:

$$\text{No convection}$$

Radiation Part:

$$\text{No radiation}$$

Conduction Part:

$$\dot{E}_{Cond,B1-BT1} = \frac{k_{Cu}}{\rho_{Cu} c_{p,Cu}} \frac{T_{n_{B1}^{End}} - 2T_{n_{BT1}^1} + T_{n_{BT1}^2}}{dx^2} \tag{135}$$

Energy Generation Part:

$$\dot{E}_{Gen,B1-BT1} = F_{Gen_2} \frac{I^2 \; \rho_{el,Cu}}{\rho_{Cu} c_{p,Cu} \left(\frac{D_{BTop}^2}{4}\pi\right)^2} (1 + \alpha_{Cu}(T_{n_{BT2}^{End}} - T_{Ref})), \qquad F_{Gen_2} = -\frac{3}{50}I^{0.43} + 0.837 \tag{136}$$

Energy Conservation Equation:

$$\frac{dT}{dt} = \dot{E}_{Cond,B1-BT1} + \dot{E}_{Gen,B1-BT1} \tag{137}$$

Node Equation for Bolt₁ (subscript: BT1)

Convection Part:

$$\text{No convection}$$

Radiation Part:

$$\text{No radiation}$$

Conduction Part 1:

$$\dot{E}_{Cond,BT1} = \frac{k_{Cu}}{\rho_{Cu} c_{p,Cu}} \frac{T_{m-1} - 2T_m + T_{m+1}}{dx^2} \tag{138}$$

Energy Generation Part:

$$\dot{E}_{Gen,BT1} = F_{Gen_2} \frac{I^2 \; \rho_{el,Cu}}{\rho_{Cu} c_{p,Cu} \left(\frac{D_{BT}^2}{4}\pi\right)^2} (1 + \alpha_{Cu}(T_m - T_{Ref})), \qquad F_{Gen_2} = -\frac{3}{50}I^{0.43} + 0.837 \tag{139}$$

Energy Conservation Equation:

$$\frac{dT}{dt} = \dot{E}_{Cond,BT1} + \dot{E}_{Gen,BT1}, \qquad \text{where } m = n_{BT1}^2, \dots, n_{BT1}^{End} \tag{140}$$

■ife

Boundary Equation for the contact between Bolt₁ and Bridge (subscript: BT1-BR)

Convection Part:

No convection

Radiation Part:

No radiation

Conduction Part:

$$\dot{E}_{Cond,BT1-BR} = \frac{k_{Cu}}{\rho_{Cu}c_{p,Cu}} \frac{T_{n_{BT1}^{End-1}} - T_{n_{BT1}^{End}}}{dx^2} \tag{141}$$

Energy Generation Part:

$$\dot{E}_{Gen,BT1-BR} = F_{Gen_2} \frac{I^2\,\rho_{el,Cu}}{\rho_{Cu}c_{p,Cu}\,\left(\frac{D_{BT}}{4}^2\pi\right)^2} \left(1 + \alpha_{Cu}(T_{n_{BT1}^{End}} - T_{Ref})\right), \qquad F_{Gen_2} = -\frac{3}{50}I^{0.43} + 0.837 \tag{142}$$

Energy Conservation Equation:

$$\frac{dT}{dt} = \dot{E}_{Cond,BT1-BR} + \dot{E}_{Gen,BT1-BR} \tag{143}$$

Node Equation for Bridge (subscript: BR)

Convection Part:

No convection

Radiation Part:

No radiation

Conduction Part:

$$\dot{E}_{Cond,BR} = \frac{k_{Cu}}{\rho_{Cu}c_{p,Cu}} \frac{T_{m-1} - 2T_m + T_{m+1}}{dx^2} \tag{144}$$

Energy Generation Part:

$$\dot{E}_{Gen,BR} = \frac{I^2\,\rho_{el,Cu}}{\rho_{Cu}c_{p,Cu}(a_{BR}b_{BR})^2} (1 + \alpha_{Cu}(T_m - T_{Ref})) \tag{145}$$

Heat Flux from Coil:

$$\dot{H}F_{Coil} = \frac{\dot{q_{Coil}}}{\rho_{Cu}c_{p,Cu}\,a_{BR}b_{BR}dx} a_{BR}dx, \qquad \text{where } \dot{q_{Coil}} = \frac{25\% \cdot P_{StandBy}}{a_{BR}L_{BR}} \left[\frac{\text{W}}{\text{m}^2}\right] \tag{146}$$

Energy Conservation Equation:

$$\frac{dT}{dt} = \dot{E}_{Cond,BR} + \dot{E}_{Gen,BR} + \dot{H}F_{Coil}, \qquad \text{where } m = n_{BR}^1, \ldots, n_{BR}^{End} \tag{147}$$

■ife

Boundary Equation for the contact between Bridge and Bolt₂ (subscript: BT2-BR)

Convection Part:

No convection

Radiation Part:

No radiation

Conduction Part:

$$\dot{E}_{Cond,BT2-BR} = \frac{k_{Cu}}{\rho_{Cu}c_{p,Cu}}\frac{T_{n_{BT2}^2} - T_{n_{BT2}^1}}{dx^2} \tag{148}$$

Energy Generation Part:

$$\dot{E}_{Gen,BT2-BR} = F_{Gen_2}\frac{I^2\ \rho_{el,Cu}}{\rho_{Cu}c_{p,Cu}\ \left(\frac{D_{BT}^2}{4}\pi\right)^2}\left(1 + \alpha_{Cu}(T_{n_{BT2}^1} - T_{Ref})\right), \qquad F_{Gen_2} = -\frac{3}{50}I^{0.43} + 0.837 \tag{149}$$

Energy Conservation Equation:

$$\frac{dT}{dt} = \dot{E}_{Cond,BT2-BR} + \dot{E}_{Gen,BT2-BR} \tag{150}$$

Node Equation for Bolt₂ (subscript: BT2)

Convection Part:

No convection

Radiation Part:

No radiation

Conduction Part:

$$\dot{E}_{Cond,BT2} = \frac{k_{Cu}}{\rho_{Cu}c_{p,Cu}}\frac{T_{m-1} - 2T_m + T_{m+1}}{dx^2} \tag{151}$$

Energy Generation Part:

$$\dot{E}_{Gen,BT2} = F_{Gen_2}\frac{I^2\ \rho_{el,Cu}}{\rho_{Cu}c_{p,Cu}\ \left(\frac{D_{BT}^2}{4}\pi\right)^2}\left(1 + \alpha_{Cu}(T_m - T_{Ref})\right), \qquad F_{Gen_2} = -\frac{3}{50}I^{0.43} + 0.837 \tag{152}$$

Energy Conservation Equation:

$$\frac{dT}{dt} = \dot{E}_{Cond,BT2} + \dot{E}_{Gen,BT2}, \qquad where\ m = n_{BT2}^1, \ldots, n_{BT2}^{End-1} \tag{153}$$

Boundary Equations where Bolt₂ connects to Busbar₂ (subscript: B2-BT2)

Convection Part:

<div align="center">No convection</div>

Radiation Part:

<div align="center">No radiation</div>

Conduction Part:

$$\dot{E}_{Cond,B2-BT2} = \frac{k_{Cu}}{\rho_{Cu}c_{p,Cu}} \frac{T_{n_{BT2}^{End-1}} - 2T_{n_{BT2}^{End}} + T_{n_{B2}^{1}}}{dx^2} \tag{154}$$

Energy Generation Part:

$$\dot{E}_{Gen,B2-BT2} = F_{Gen_2} \frac{I^2\,\rho_{el,Cu}}{\rho_{Cu}c_{p,Cu}\left(\frac{D_{BTop}^2}{4}\pi\right)^2}(1 + \alpha_{Cu}(T_{n_{BT2}^{End}} - T_{Ref})), \qquad F_{Gen_2} = -\frac{3}{50}I^{0.43} + 0.837 \tag{155}$$

Energy Conservation Equation:

$$\frac{dT}{dt} = \dot{E}_{Cond,B2-BT2} + \dot{E}_{Gen,B2-BT2} \tag{156}$$

Node Equation for Busbar₂ (subscript: B2)

Convection Part:

$$\dot{E}_{Conv,B2} = \underbrace{\frac{2}{\rho_{Cu}c_{p,Cu}a_B}\frac{7.66}{\sqrt[4]{b_B 10^3}}\sqrt[4]{[T_{Room} - T_m]^5}}_{Vertical\ Surface} + \underbrace{\frac{2}{\rho_{Cu}c_{p,Cu}b_B}\frac{5.92}{\sqrt[4]{a_B 10^3}}\sqrt[4]{[T_{Room} - T_m]^5}}_{Horizonal\ Surface} \tag{157}$$

Radiation Part:

$$\dot{E}_{Rad,B2} = \frac{2\,(a_B + b_B)\varepsilon\sigma}{\rho_{Cu}c_{p,Cu}\,a_B b_B}((T_{Room} + 273.15)^4 - (T_m + 273.15)^4) \tag{158}$$

Conduction Part:

$$\dot{E}_{Cond,B2} = \frac{k_{Cu}}{\rho_{Cu}c_{p,Cu}} \frac{T_{m-1} - 2T_m + T_{m+1}}{dx^2} \tag{159}$$

Energy Generation Part:

$$\dot{E}_{Gen,B2} = F_{Gen_1} \frac{I^2\,\rho_{el,Cu}}{\rho_{Cu}c_{p,Cu}(a_B b_B)^2}(1 + \alpha_{Cu}(T_m - T_{Ref})), \qquad \text{where } F_{Gen_1} = 0.82 \tag{160}$$

Energy Conservation Equation:

$$\frac{dT}{dt} = \dot{E}_{Conv,B2} + \dot{E}_{Rad,B2} + \dot{E}_{Cond,B2} + \dot{E}_{Gen,B2}, \qquad \text{where } m = n_{B2}^1, \ldots, n_{B2}^{End-1} \tag{161}$$

Boundary Equations where Busbar₂ connects to PSU (subscript: B2-PSU)

Convection Part:

$$\dot{E}_{Conv,B2-PSU} = \underbrace{\frac{2}{\rho_{Cu}c_{p,Cu}a_B}\frac{7.66}{\sqrt[4]{b_B 10^3}}\sqrt[4]{\left(T_{Room} - T_{n_{B2}^{End}}\right)^5}}_{Vertical\ Surface} + \underbrace{\frac{2}{\rho_{Cu}c_{p,Cu}b_B}\frac{5.92}{\sqrt[4]{a_B 10^3}}\sqrt[4]{\left(T_{Room} - T_{n_{B2}^{End}}\right)^5}}_{Horizonal\ Surface} \tag{162}$$

Radiation Part:

$$\dot{E}_{Rad,B2-PSU} = \frac{2\,(a_B + b_B)\varepsilon\sigma}{\rho_{Cu}c_{p,Cu}\,a_B b_B}\left((T_{Room} + 273.15)^4 - (T_{n_{B1}^1} + 273.15)^4\right) \tag{163}$$

Conduction Part:

$$\dot{E}_{Cond,B2-PSU} = \frac{k_{Cu}}{\rho_{Cu}c_{p,Cu}}\frac{T_{n_{B2}^{End-1}} - T_{n_{B2}^{End}}}{dx^2} \tag{164}$$

Energy Generation Part:

$$\dot{E}_{Gen,B2-PSU} = F_{Gen_1}\frac{I^2\,\rho_{el,Cu}}{\rho_{Cu}c_{p,Cu}(a_B b_B)^2}(1 + \alpha_{Cu}(T_{n_{B2}^{End}} - T_{Ref})), \qquad \text{where } F_{Gen_1} = 0.82 \tag{165}$$

Energy Conservation Equation:

$$\frac{dT}{dt} = \frac{1}{2}\dot{E}_{Conv,B2-PSU} + \frac{1}{2}\dot{E}_{Rad,B2-PSU} + \dot{E}_{Cond,B2-PSU} + \frac{1}{2}\dot{E}_{Gen,B2-PSU} \tag{166}$$

List of Figures

ife

![ife logo]

List of Tables

ife

Biography

[1] M. Rosina, "I-Micronews," July 2018. [Online]. Available: https://bit.ly/2YbkLfX. [Accessed 3 December 2019].

[2] M. B. Svensson and A. Engelbrektsson, An Optimised Packaging Solution of a Battery Disconnect Unit, Gothenburg: Department of Product and Production Development at Chalmers University of Technology, 2017.

[3] S. Kang, "Battery disconnect unit". US Patent US 10.250.047 B2 , 2 April 2019.

[4] K. Fukahori and P. Gray, "Computer simulation of integrated circuits in the presence of electrothermal interaction," *IEEE Journal of Solid-State Circuits ,* vol. 11, no. 6, pp. 843-846, 1976.

[5] E. J. Diebold and W. Luft, "Transient thermal impedance of semiconductor devices," *Trans. Amer. Inst. Electr. Eng., I, Commun. Electron,* vol. 79, no. 6, pp. 719-726, 1961.

[6] K. H. Kwok and V. d'Alessandro, "Fast Analytical Modelling of Dynamic Thermal Behaviour of Semiconductor Devices and Circuits," *IEEE Transactions on Electron Devices,* vol. 61, no. 4, pp. 1031-1038, 2014.

[7] A. R. Hefner and D. L. Blackburn, "Thermal Component Models for Electro-Thermal Network Simulation," in *Ninth Annual IEEE Semiconductor Thermal Measurement and Management Symposium*, Austin, TX, USA, 1993.

[8] K. Mashimo, Y. Saita, K. Koizumi and H. Nakazato, "Heat Transfer Analysis for Vehicle Electronic Parts," *Furukawa Review ,* no. 22, pp. 1-6, 2002.

[9] M. Capobianchi, V. Labay, F. Shi and G. Mizushima, " Simulating the Electrical Behaviour of Integrated Circuit Devices in the Presence of Thermal Interactions," *IEEE Transactions on Computer-Aided Design of Integrated Circuits and Systems,* vol. 25, no. 10, pp. 2231-2241, 2006.

[10] T. Azoui, P. Tounsi, P. Dupuy and J.-M. Dorkel, "Dynamic compact thermal model for smart electro-thermal simulation: Application to automotive power device," in *IEEE Bipolar/BiCMOS Circuits and Technology Meeting (BCTM)*, Austin, TX, USA, 2010.

[11] S. Y. Hwang, J. H. Lee, K. K. Visuwanthan and I. Ban, "Experiments and thermal-electrical analysis of buss bar and relay assemblies in junction blocks," *International Journal of Automotive Technology,* vol. 1, no. 14, pp. 79-90, 2013.

[12] A. Chvála, J. Marek, P. Príbytný and D. Donoval, "Advanced 3-D device and circuit electrothermal simulations of power integrated circuit," in *46th European Solid-State Device Research Conference (ESSDERC)*, Lausanne, Switzerland, 2016.

[13] J. Meng, X. Wen, Y. Zhong, Z. Qiu and L. Kong, "A thermal model for electrothermal simulation of power modules," in *International Conference on Electrical Machines and Systems (ICEMS)*, Busan, South Korea , 2013.

[14] F. Freschi, M. Mitolo and R. Tommasini, "Shielding the Public from Shock," *IEEE Industry Applications Magazine,* vol. 24, no. 3, pp. 58-63, 27 Frebruary 2018.

ife

[15] S. Jud and G. Hehn, "Battery management systems for electric vehicles: The crucial role of the current sensor interface," 12 August 2014. [Online]. Available: https://www.electronicproducts.com. [Accessed 17 March 2020].

[16] V. Yuvraj, "BATTERY MANAGEMENT SYSTEM," 26 March 2019. [Online]. Available: http://www.engineeringfact.com/battery-management-system/. [Accessed 18 March 2020].

[17] G. J. Girard and P. Whalen, "Modular battery disconnect unit". US Patent US 9.266.434 B2 , 23 February 2016.

[18] P. Lell, "Innovative Safety Concept to Shutdown Short Circuit Currents in Bat-tery Systems up to 1000V Based on Ultrafast Pyrofuse Technology," Albuquerque, 2018.

[19] S. Leibson, "Digi Key Electronics," 9 October 2018. [Online]. Available: https://www.digikey.at/. [Accessed 15 March 2020].

[20] F. Stadler, "DAS OHMSCHE GESETZ IN DER PRAKTISCHEN ANWENDUNG," *Genauigkeit bei der Strommessung,* pp. 26-28, November 2013.

[21] U. Hetzler and T. Kuther, "Widerstände für Strommessungen in Automobilanwendungen," 31 August 2011. [Online]. Available: https://www.elektronikpraxis.vogel.de. [Accessed 20 March 2020].

[22] "Four-terminal sensing," 13 December 2019. [Online]. Available: https://en.wikipedia.org/. [Accessed 16 March 2020].

[23] J. R. Davis, "Metallurgy, Alloys and Applications," in *ASM Specialty Handbook: Copper and Copper Alloys*, ASM International, 2001, pp. 158-159.

[24] "Seebeck coefficient," 18 July 2019. [Online]. Available: https://en.wikipedia.org/wiki/Seebeck_coefficient. [Accessed 19 March 2020].

[25] "EV Relays (DC Contactors)," 26 July 2018. [Online]. Available: https://www3.panasonic.biz. [Accessed 8 April 2020].

[26] "LSIS HV DC Relay(Contactor)," 24 June 2019. [Online]. Available: https://www.youtube.com/watch?v=VnFLZCArVeQ. [Accessed 8 April 2020].

[27] R. C. Life, n.d.. [Online]. Available: https://www.te.com/. [Accessed 24 March 2020].

[28] "High Voltage DC Relay for New Energy Vehicle," 25 February 2019. [Online]. Available: https://www.evs-cn.com. [Accessed 22 March 2020].

[29] M. Büchsenmeister, "Test Report High Power BDU Test," SAMSUNG SDI Battery Systems, Graz, 2020.

[30] Incropera, DeWitt, Bergman and Lavine, Heat and Mass Transfer, Hoboken: John Wiley & Sons, 2007.

[31] O. Fabris, Osnovi inženjerske termodinamike, Sarajevo: Svjetlost, 1988.

[32] Y. A. Çengel and A. J. Ghajar, "Numerical Methods in Heat Conduction," in *Heat and Mass Transfer: Fundamentals & Applications 5th Edition*, McGraw-Hill, The McGraw-Hill Companies, 2015.

ife

[33] E. Parliament, "European Parliament," 3 October 2019. [Online]. Available: https://bit.ly/34NaKYD. [Accessed 3 December 2019].

[34] P. Lell, "Innovative Safety Concept to Shutdown Short Circuit Currents in Bat-tery Systems up to 1000V Based on Ultrafast Pyrofuse Technology," Albuquerque, 2018.

ife